SPATIAL PROFILING OF QUANTUM DOT LASERS

Vinod Rangaswamy Vukkalam

Thesis submitted in partial fulfillment of the
requirements for the degree
Master of Science (Research)

from the
WATERFORD INSTITUTE OF TECHNOLOGY, WATERFORD, IRELAND

Research Supervisor :

Dr. John Houlihan,

Mentoring Supervisor:

Dr. Claire Keary

Submitted to Waterford Institute of Technology on January, 2012

ABSTRACT OF THE DISSERTATION

The unique electronic structure of quantum dot based semiconductor lasers leads to significant differences in lasing properties when compared to their quantum well counterparts. In particular, the total injected carrier population can be separated into two types: one that take part in lasing process, called resonant charge carriers and the other one that do not take part in lasing process, called non-resonant charge carriers. In this thesis, two methods are used to model injection profiled quantum dot lasers and examine the roles of resonant and non-resonant carrier populations.

The first model is a rate equation approach, which is used to analyze the dynamical properties along the transverse section of the laser. The second model is a steady state beam propagation approach, which calculates both transverse and longitudinal carrier and field distributions in the laser. Numerical simulations on both models reveal the role of non-resonant carries in the appearance of a characteristic dip at the center of the near field intensity profile. Furthermore, these models reveal the occurrence of symmetry breaking in the near and far field intensity distributions at high injection currents. In addition, the steady state beam propagation approach uncovers non-uniformities in the non-resonant carrier profile along the longitudinal dimension.

In addition to single emitters, this work also examines the possibility of phase-locking between two transversely coupled injection profiled QD lasers, where various types of phase relationships are identified. We compare the performance of single and double emitters by examining the beam focusing properties and evaluating M^2 factor for various configurations.

DECLARATION

This thesis is a presentation of my original research work. Wherever contributions of others are involved, every effort is made to indicate this clearly, with due reference to the literature, and acknowledgment of collaborative research and discussions. The work was done under the guidance of Dr. John Houlihan at the Waterford Institute of Technology, Waterford, Ireland.

DEDICATION

To my family.

TABLE OF CONTENTS

LIST OF FIGURES

LIST OF TABLES

ACKNOWLEDGEMENTS

I would like to thank my research supervisor, Dr. John Houlihan, for his support, generosity and guidance over the last two years of this program. I could not envision this work without him. I would also like to thank my mentoring supervisor, Dr. Claire Keary for her endorsement of my studentship.

I would also like to acknowledge the financial support from the Institute of Technology Irelands Strand I program, and access to QD structures under the Tyndall National Access Program (NAP).

PUBLICATIONS AND CONFERENCE PRESENTATIONS

Vinod Vukkalam and John Houlihan, Optics Communications, Volume 283, Issue 12, Pages 2596-2602, 15 June (2010).

Vinod Vukkalam and John Houlihan, "Beam properties of injection profiled quantum dot lasers", Waterford Institute of Technology (WIT) Research day, May 17, 2010.

Chapter 1

Introduction

1.1 Overview and Objectives

Diode lasers have a wide range of applications and have become the most common laser in the world today. These devices are used in telecommunications, optical storage, material processing, medical therapeutic, sensing and metrology. Even though these compact light emitters are used in a wide range of applications, a profound impact is yet to be met in health care and materials processing fields, due to limitations in the achievable brightness[1]. As a result, systems design and modifications to improved beam quality and achieve high brightness feature continues to generate a lot of research interest.

One approach that has received a lot of attention lately, involves the use of quantum dot [QD] nanostructures as an active laser medium in high power laser diodes. These devices offer improved operating characteristics such as high modulation bandwidths [7] [6], low linewidth enhancement factor, temperature-insensitive threshold current, high insensitivity to optical feedback, low threshold current density, high tunability of gain spectrum width and emission wavelength, low chirp (shift of lasing wavelength with injection current), improved beam quality (M^2 characteristics) and reduced filamentation than conventional semiconductor lasers like bulk and Quantum Well (QW) lasers.

[1]Generally, the term "high brightness" can be understood as the ability of a high power laser diode to focus to a small area and achieve high power densities

The objective of this thesis was, to numerically simulate QD laser output patterns using a variety of methods and compare to experimental measurements. In doing that, the role of non-resonant charge carriers, width of Lorentzian injection profile and other important laser parameters could be addressed. Furthermore, a detailed study of symmetry breaking at the near and far field intensity distributions due to high injection currents was carried out. In addition, the phase relationship between two coupled injection profiled QD laser emitters was investigated and compared to a previously investigation on quantum well devices. Thus the research study aims to improve the performance of these devices close to that of gas lasers, and demonstrates the capability of QD structures to ameliorate drawbacks typically associated with the traditional semiconductor lasers based on bulk or quantum well active media.

1.2 A Historical Perspective

In 1960, Theodore H. Maiman successfully demonstrated a functioning laser for the first time, using a solid-state flash lamp to pump a synthetic ruby crystal, resulting in a red light emission at a wavelength of 694 nm [47]. In 1962, Robert N. Hall constructed the first diode laser in the near-infrared region at 850 nm wavelength using gallium arsenide [47]. During the late 1990's, there evolved a need for semiconductor lasers, that were highly insensitive to temperature and optical feedback, so that they could be employed as optical sources for next-generation high-speed data communications. Currently, the desire to achieve high speed data transmission of 100 Gbps is driving much communications related research on diode lasers.

The evolution of semiconductor lasers can be separated into various semiconductor wafer designs. The first generation laser diodes were homojuction type with threshold current densities of 1000 $\frac{A}{cm^2}$ at 77 K temperature [47]. These devices had even higher threshold current densities (in the 100,000 $\frac{A}{cm^2}$ range), when operated at room temperature. Clearly, these devices did not find widespread application as they required high powers to operate and delivered low outputs due

to thermal rollover.

The next step in the evolution was the heterojunction device. The first heterojunction diode lasers had a single-heterojunction with threshold current densities in the 10,000 $\frac{A}{cm^2}$ range at 300 K. Compared to the homojuction type the threshold current densities were lowered by 10 times. Unfortunately, these devices were still not achieving adequate performance for practical applications. Moreover these devices did not function in continuous wave (CW) operation at room temperature.

The need to improve the output performance led to the discovery of double heterostructure (DH) lasers, where a thin layer of low bandgap material is sandwiched between two high bandgap layers. In these devices, the laser optical field is generated by electron-hole recombination in the thin sandwiched layer also known as active layer. During the late 1970s, the active layer thickness in DH lasers was about 100-200nm [95]. As the years progressed, technological improvements in the fabrication field allowed the thinning down of the active layer thickness to $\leq$ 10 nm. This changed the available distribution of energy states (Density of states) for electrons and holes confined in the active layer. The density of states changed from quasi-continuous to discrete due to quantum confinement effects. Since lasing action is obtained by stimulating carrier recombination between the discrete (quantum well) states, the devices were called quantum well (QW) lasers. The exceedingly low threshold currents and the very high quantum efficiencies from these devices made them good optical sources for data communications. Currently, the transmission speed from these devices is 10 Gbps [56] [2]. The main drawback with QW lasers is their operating sensitivity to temperature changes, which in turn corresponds to a dramatic rise in power consumption and the need for expensive temperature control schemes.

Further improvements in the laser efficiency have also been achieved by reducing the quantum well layer to distributions of quantum wire or quantum dot nanostructures. The first quantum dot laser capable of 25 Gbps data transmission speed was developed by the Fujitsu Laboratories [56]. This latest innovation had

[2]Note: 40 Gbps can be obtained from these devices using external optics [66]

a high temperature insensitivity feature, which made these devices extremely attractive as optical sources for high-speed communications. Thus the study of QD laser beam properties acquired a high research prominence. In this thesis, using QD laser rate equations [15] we examine the effect of various device parameters on the output beam profile.

1.3 Scope of the Thesis

The outline of the thesis is as follows: Chapter 2 discusses the basic physics behind the operation of the semiconductor laser and types of diode lasers. This chapter also includes the fundamentals of nanostructures like quantum well, quantum wire and quantum dot. Chapter 3 introduces injection current profiling and outlines simulation results from rate equation approach of injection profiled quantum dot laser. Chapter 4 describes beam propagation approaches and reports on simulation results from steady state carrier beam propagation of injection profiled quantum dot laser. Chapter 5 discusses types of semiconductor laser array devices, and outlines simulation results from both rate equation and steady state carrier beam propagation approach of two transversely coupled injection profiled quantum dot lasers. Chapter 6 describes methods of laser beam evaluation and presents simulation results from focusing beam properties of injection profiled lasers and arrays. This involves taking the steady state electric field from the QD laser device simulated through rate equation approach and propagating through free space using beam propagation approach. This allows the performance of the QD laser beam to be evaluated using M^2 values.

Chapter 2

Background

2.1 Laser

The laser's[1] theoretical groundwork was framed, when Einstein postulated the theory of stimulated emission. The stimulated emission process can be simply understood as: an electron in the higher energy level drops to a lower energy level in the presence of an incident photon leading to the emission of another photon and the perturbing photon remains unchanged. The newly emitted photon has the same phase, frequency, polarization, and the direction of propagation with respect to the incident photon (see fig[2.1]). Generally, lasers are composed of three main elements: a gain medium (either solid, liquid or gas), a pump source and a resonator cavity.

In order to have the stimulated emission process, two conditions must be fulfilled. Firstly, the number of atoms (N_2) in the higher excited levels must be greater than the number of atoms (N_1) in the lower energy levels. In other words, a population inversion ($N_2 > N_1$) must be achieved, as more atoms occupy the lower energy levels than the higher levels due to Boltzmann thermal distribution law. Therefore, an external pump source (usually either electrical or optical) is used to attain population inversion. This condition is essential otherwise the stimulated emission of light can be re-absorbed directly by the atoms in the lower energy

[1]LASER is an acronym, which stands for "Light Amplification by Stimulated Emission of Radiation".

states. Secondly, the stimulated emission of radiation in the gain medium must be dominant over the spontaneous emission. In order to achieve this requirement, an optical resonator must be used to traverse the resultant photons (from the stimulated emission process) back and forth inside the laser cavity to have a cascading effect. This type of optical feedback generates a highly unidirectional, coherent, monochromatic light emission from the low reflecting cavity facet.

A full mathematical analysis of absorption, stimulated emission, and spontaneous emission was given by A. Einstein through the requirement that the system should be in thermal equilibrium, i.e. the rate of upward transition (from E_1 to E_2) must be equal to the rate of downward transition (from E_2 to E_1). Let us suppose that the two-level atomic energy level system (as shown in figure [2.16]) is in equilibrium inside a blackbody cavity. Now the rate of absorption (R_{12}) of radiation at a frequency ω_{12} is given as:

$$R_{12} = B_{12} N_1 \rho(\omega_{12}) \tag{2.1}$$

Where "B_{12}" is a absorption coefficient and "$\rho(\omega_{12})$" is the energy density at the frequency ω_{12}. The rate of emission has both spontaneous and stimulated components, i.e.

$$R_{21} = A_{21} N_2 + B_{21} N_2 \rho(\omega_{21}) \tag{2.2}$$

Where B_{21} is the coefficient for stimulated emission and A_{21} is the coefficient for spontaneous emission.

In thermal equilibrium then,

$$\rho(\omega_{21}) = \rho(\omega_{12}) \; and \; R_{21} = R_{12} \tag{2.3}$$

hence

$$\rho(\omega_{12}) = \frac{N_2 A_{21}}{N_1 B_{12} - N_2 B_{21}} \tag{2.4}$$

or

$$\rho\left(\omega_{12}\right) = \frac{\frac{A_{21}}{B_{21}}}{\frac{B_{12}}{B_{21}}\left(\frac{N_1}{N_2}\right) - 1} \tag{2.5}$$

The relative populations of two energy levels E_2 and E_1 in thermal equilibrium are governed by Fermi-Dirac statistics. However, under certain conditions it is possible to use the Boltzmann approximation. Therefore the two population densities are then related by:

$$\frac{N_2}{N_1} = \frac{g_2}{g_1}\left[exp\left(\frac{E_1 - E_2}{kT}\right)\right] \tag{2.6}$$

Where "k" is Boltzmann constant,"T" is temperature and "g_i" is the degeneracy of the ith level.

Since the two atom system we are considering is in thermal equilibrium, it must give rise to radiation that must be identical to the black body spectrum, derived by Planck.

$$\rho\left(\omega\right) = \frac{\omega^3}{\pi^2 c^3}\left[exp\left(\frac{\hbar\omega}{kT} - 1\right)\right]^{-1} \tag{2.7}$$

Where "c" is speed of light in vacuum , $\omega = \frac{2\pi}{\lambda}$, "$\lambda$" is wavelength and "$\hbar = \frac{h}{2\pi}$" is the Planck constant.

Comparison between equations [2.5] and [2.7] results in,

$$g_1 B_{12} = g_2 B_{21} \tag{2.8}$$

and

$$\frac{A_{21}}{B_{21}} = \frac{\hbar\omega^3}{\pi^2 c^3} \tag{2.9}$$

Equations [2.8] and [2.9] are referred to as the Einstein relations. The relation [2.9] enables us to measure the ratio of the rate of spontaneous emission to the rate of stimulated emission for a given pair of energy levels and the ratio is given by

$$R = \frac{A_{21}}{\rho\left(\omega_{21}\right) B_{21}} \tag{2.10}$$

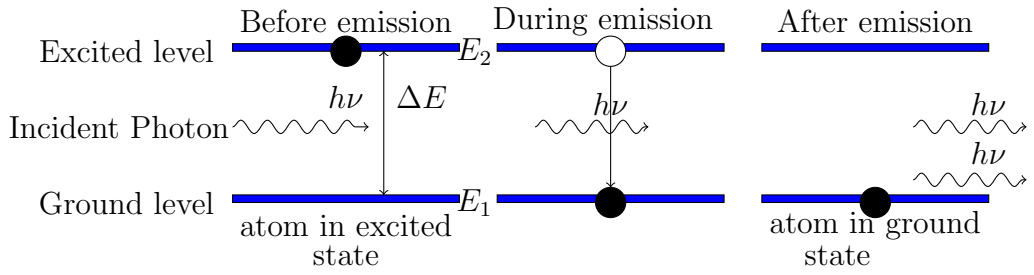

Figure 2.1: Stimulated Emission process, where the incident (perturbed) photon having energy ($h\nu$) causes excited atom to emit photon with same energy ($h\nu$) and $\Delta E = E_2 - E_1 = h\nu$.

On the whole, laser devices can be broadly divided into two groups based on the output power:

- Continuous Wave (CW) Laser, where output power is constant;
- Pulsed Laser, where output power fluctuates repetitively in time.

In the following section, a simple outline of the semiconductor lasers is illustrated.

2.2 Semiconductor lasers

Lasing action in the semiconductor diode lasers is quite different from other laser types. These devices don't have sharp distinct energy levels, instead, the presence of bands makes the quantitative description of the population inversion difficult. The available states and the charge carriers are spread non-uniformly over a range of energies in both the conduction and the valence bands. In addition, the statistical nature (Fermi-Dirac statistics) of the carrier density results in different stimulated emission rates for different incident photon energies. Nonetheless, the possibility of high carrier densities in these structures enables the realization of much smaller laser device plus the electrical injection of carriers makes them highly desirable.

2.2.1 Functioning principles

The radiative emission in the diode lasers is due to recombination of the electrons and the holes at the p-n junction region or in a heterostructure region. Forward electrical bias causes the electrons and the holes to be "injected" into the depletion region (formed between p-n junction and is almost free of charge carriers) or in a heterostructure region from their respective n-doped and p-doped layers. Recombination of these charge carriers can result in either spontaneous or stimulated emission of light. In a laser, if gain is less than the photon losses due to absorption and mirror losses, then the laser is said be working in the below threshold region and the light emanating from the diode is predominantly spontaneous emission. However, in the above threshold region (*i.e.* $gain > Loss$) both spontaneous and stimulated emission of light occurs. Nevertheless, only light from the stimulated emission gets amplified in the resonator cavity.

2.2.2 Optical Amplification in Semiconductor Lasers

The role of the Fabry-Perot cavity is threefold. First, it directs the radiation from stimulated emission in one particular direction depending on the geometry of the cavity facets. Second, it brings in a frequency-selective mechanism, which only sets a limited number of longitudinal cavity modes to resonate in the cavity. Third, it allows a fraction of radiation to pass through one of the low partially reflecting facets (see fig [2.2]). Also, a fraction of the electric field is re-absorbed by the different material layers constituting the laser.

The quantitative description of the above roles played by Fabry-Perot cavity can be illustrated mathematically. As shown in the figure [2.2], the nature of the optical feedback from the laser mirrors creates standing waves between the mirrors. Therefore the possible wavelengths that can propagate inside the cavity are:

$$m \frac{\lambda_0}{2} = L n_g,\ m = 1, 2, 3.... \tag{2.11}$$

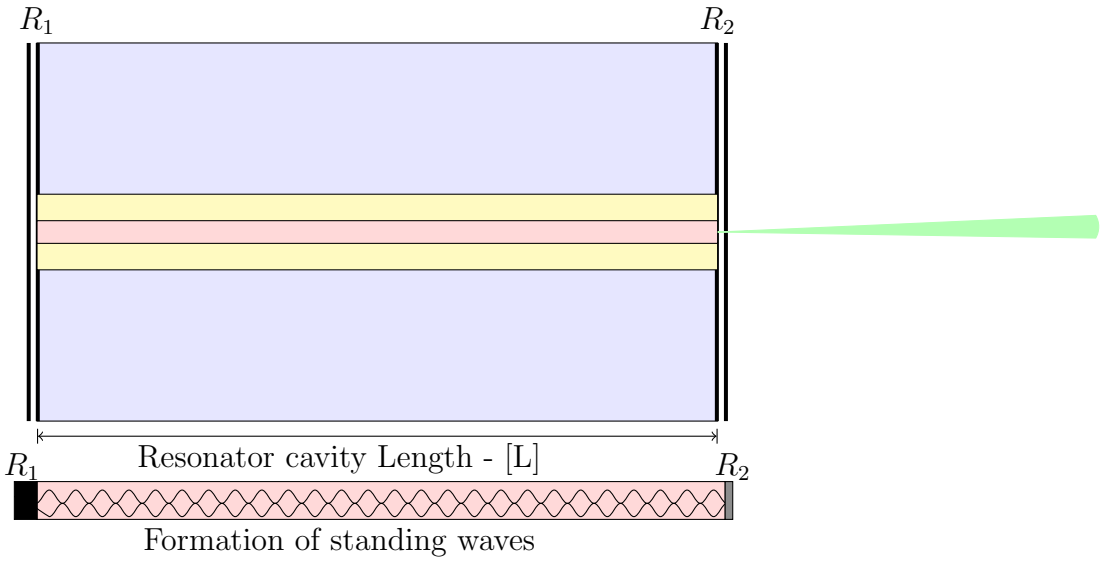

Figure 2.2: Schematic representation of a diode laser optical resonator. R_1 - High reflective mirror (black), R_2 - Low reflective mirror (black), Cladding layer (light blue), Waveguide layer (light yellow & light red), Active region (light red), Emitted radiation (light green).

Where "m" is the number of the nodes of the standing wave, the order number of the longitudinal mode, "n_g" denotes to group refractive index, "L" represents the cavity length and "λ_0" is the vacuum wavelength.

Mathematically, the frequency and the wavelength spacing of the longitudinal modes are given as:

$$\Delta\nu = \frac{c}{2n_g L} \tag{2.12}$$

$$\Delta\lambda = \frac{\lambda_0^2}{2n_g L} \tag{2.13}$$

Where both "$\Delta\lambda$ *and* $\Delta\nu$" represents the free spectral range of an optical resonator.

If the effective spectral width ($\Delta\nu_g$) of the semiconductor gain medium is known, then the number of longitudinal modes that can resonate in the Fabry-Perot cavity can be calculated using the ratio $\frac{\Delta\nu_g}{\Delta\nu}$.

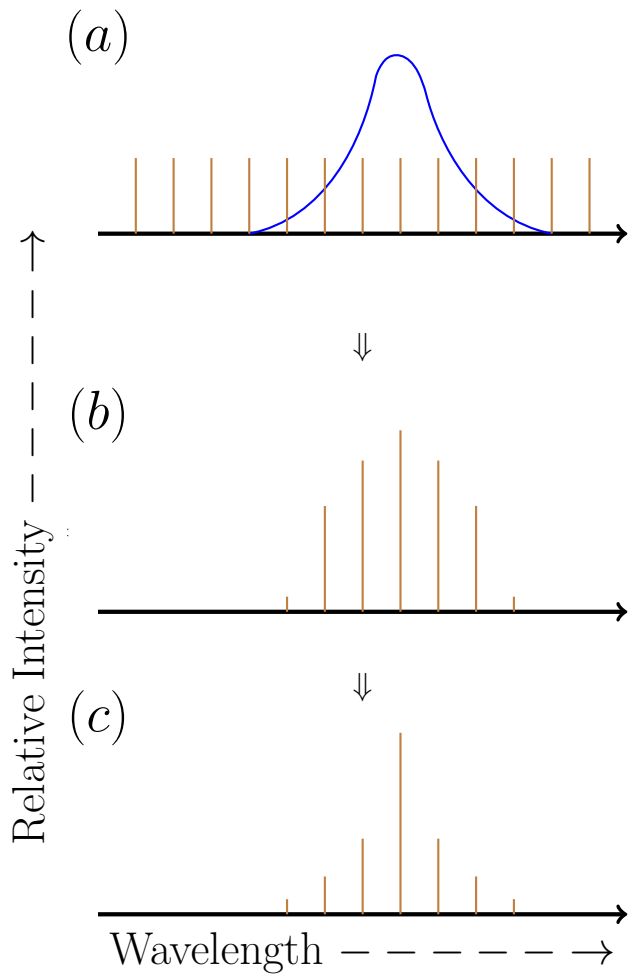

Figure 2.3: Schematic representation of Fabry-Perot modes that produce a self-selected narrow output spectrum. The above Fabry-Perot modes (brown) are evenly spaced in wavelength and will therefore constitute a spectrum of optical signals that can be fed back into the active medium. Those nearest in wavelength to the center of the gain curve (blue) will be self selected after a number of rotations inside Fabry-Perot cavity, and the output of the laser will consist of a single line, or at most a few modes, of very narrow spectral width. The amplitude of the final stage (c) will distinctly be much greater than the beginning (a) and intermediate stages (b).

2.2.3 Laser Threshold

For any semiconductor diode laser to lase, the gain experienced by photons inside the Fabry-Perot cavity must be greater than the internal losses plus the fraction of the intensity that is emitted through the low reflecting mirror. The lasing threshold is defined as the point where the gain is equal to the loss. Let us include all optical losses except those due to transmission at the mirrors in a single effective loss coefficient (γ). We presume that the laser medium fills the space between the mirrors (see figure [2.2]). Then the beam irradiance in travelling from one cavity facet to another cavity facet undergoes an intensity change from I_0 to I. Mathematically, this can be written as:

$$I = I_0 \, exp\left[(g - \gamma)\, L\right] \tag{2.14}$$

Where "L" is the cavity length and g is the gain coefficient. After reflection at the facet, the beam irradiance will be $R_2 I_0 \, exp\left[(g - \gamma)\, L\right]$ and after a complete round trip the final irradiance will be $R_1 R_2 I_0 \, exp\left[2\,(g - \gamma)\, L\right]$, where the round trip gain G is:

$$G = \frac{final\ irradiance}{initial\ irradiance} = R_1 R_2 \, exp\left[2\,(g - \gamma)\, L\right] \tag{2.15}$$

For the laser to lase G must be greater than unity. The laser threshold is reached when the net gain G is unity.

$$G = R_1 R_2 \, exp\left[2\,(g_{th} - \gamma)\, L\right] = 1 \tag{2.16}$$

$\Rightarrow$

$$g_{th} = \gamma + \frac{1}{2L} \ln\left(\frac{1}{R_1 R_2}\right) = \gamma + \alpha_m \tag{2.17}$$

Where "g_{th}" refers to threshold gain coefficient and "α_m" represents mirror losses. Therefore, equation [2.17] represents laser threshold condition.

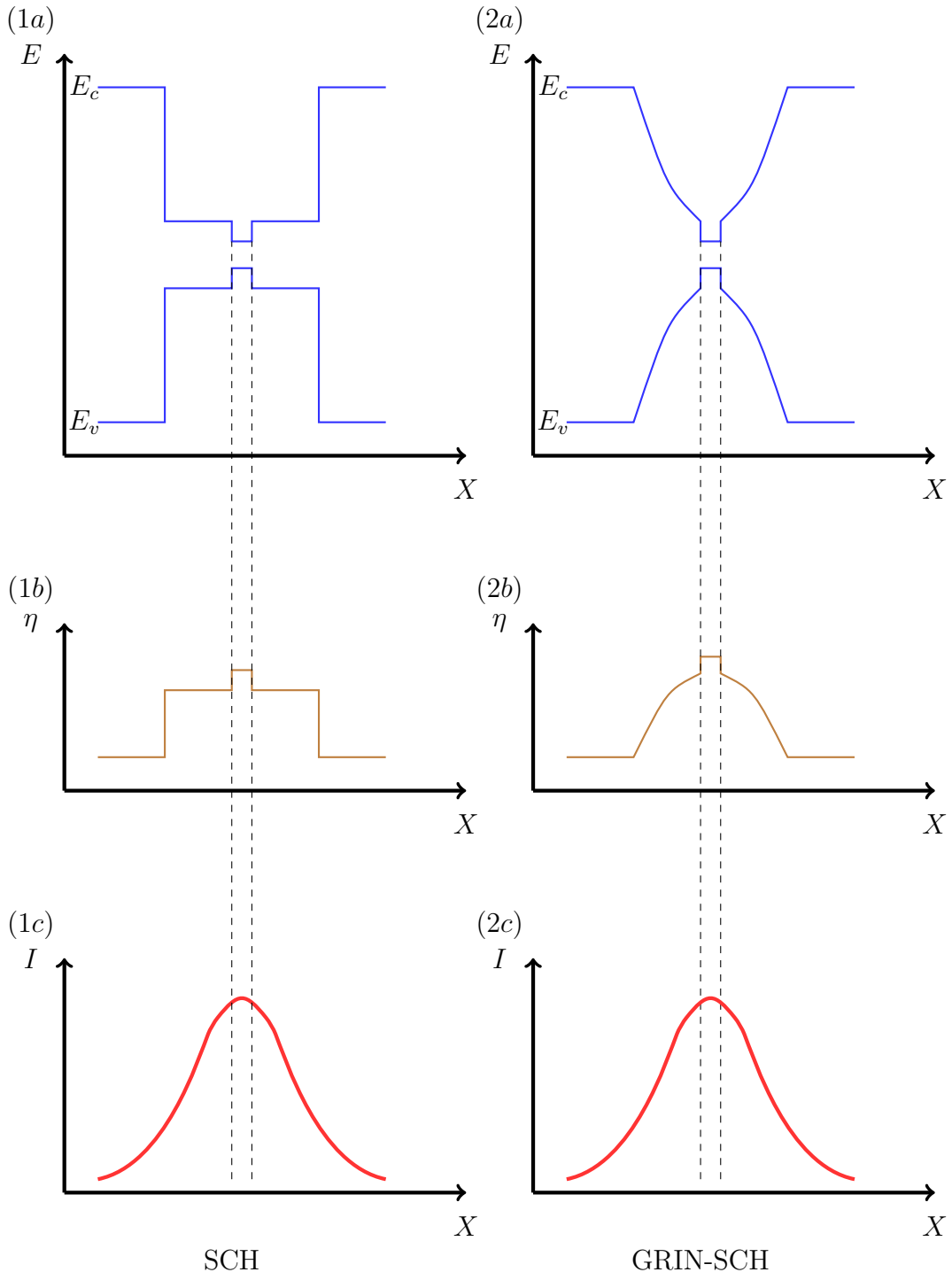

Figure 2.4: Schematic representation of Energy band structure (1a), Index of refraction profile (1b), and Optical field profile (1c) for separate confinement heterostructures (SCH) and (2a), (2b), and (2c) represents the corresponding Energy band structure, Index of refraction profile, and Optical field profile for graded index separate confinement heterostructures (GRIN-SCH).

2.3 Transverse Structure

A laser beam propagating in a homogeneous medium will expand due to diffraction. Therefore, confining light in the active region is an issue for semiconductor lasers. A common procedure to prevent this beam expansion is to use a guiding structure with a spatially varying refractive index profile, known as a waveguide.

Although simple quantum well or quantum dot lasers have good charge carrier confinement, these emitters cannot confine light properly, because the active layer thickness is too thin $\leq 10\,nm$. To compensate, additional layers are added in such a way that the active layer is sandwiched between the new layers. The refractive index of the active layer is high and guides the optical wave between these new outer layers of lower refractive index. As shown in the figure [2.4], the index of refraction profile of the SCH structure determines the optical field profile. A GRIN-SCH structure is different from a SCH structure because the inner barrier layers are engineered in such a way that the refractive index profile grades in a parabolical way (see figure [2.4]).

In general, a semiconductors laser consists of a number of epitaxial layers, engineered by varying the composition, thickness, and doping to provide an electrically and optically efficient device. As shown in the figure [2.5], a typical $Al_xGa_{1-x}As - GaAs$ semiconductor laser diode [2] has a heavily doped cap and substrate layers in order to facilitate low resistance ohmic contacts. The confining layers are chosen in such a way that the bandgap energy is greater than the active layer and the inner barrier layers. The active layer has the smallest bandgap energy and provides an efficient confinement of injected electrons and holes in the active layer.

[2] In this thesis, for simplicity, only important layers are outlined for the upcoming figures on diode lasers.

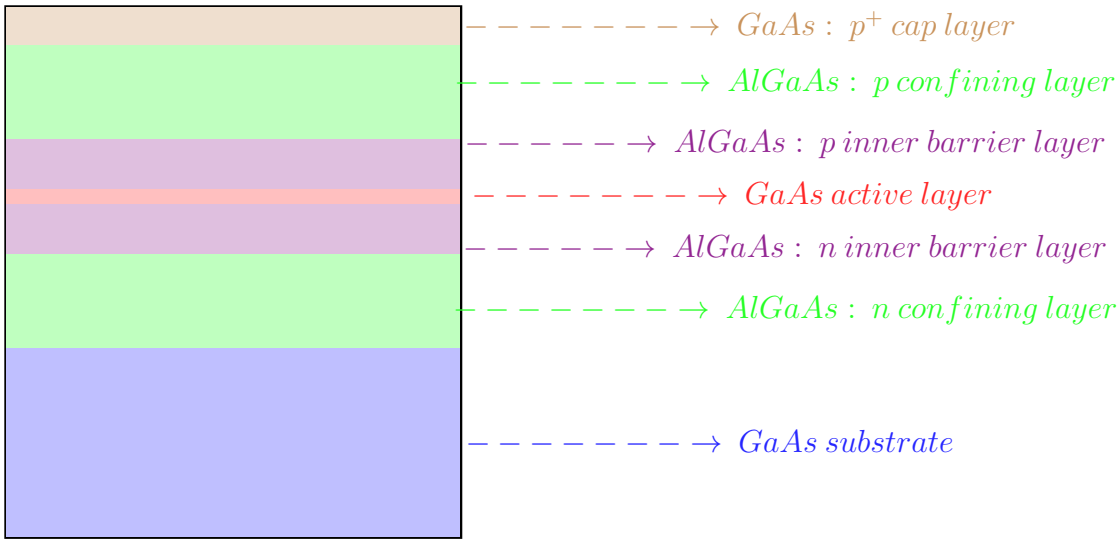

Figure 2.5: Schematic cross-section of a typical $Al_xGa_{1-x}As - GaAs$ semiconductor laser diode.

2.4 Transverse confinement

Transverse confinement of current, charge carriers and optical mode is an important requirement for semiconductor lasers. A diode laser lacking in transverse confinement leads to high thresholds and nonlinearities in its light vs current characteristics. Several laser designs were developed over the years to address these problems. Among them are gain guided lasers, ridge waveguide lasers and buried heterostructure lasers.

2.4.1 Gain guided laser

If the optical mode distribution along the transverse x dimension is determined by the optical gain profile then the devices are said to be gain guided structures. Gain guiding is the most simple form of transverse confinement.

As shown in the figure [2.6], the gain guided laser has a stripe geometry, where the metal contact is the stripe with a width "w" defined by processing procedure. Here, the basic idea is to pump the central part of the active region. The injected current J spreads along the transverse (*i.e.*, x) direction. For the most part, only regions lying under the contact stripe are pumped and the rest

of the active layer acts as absorbing regions. The carrier density (n) distribution along the x direction is determined by the current spreading and the transverse diffusion. Therefore, the effective width of the carrier density distribution and the gain profile along the transverse direction are wider than the stripe width w. An associated effect is the refractive index in the pumped region decreases with respect to unpumped regions, resulting in an antiguiding effect. Thus the gain inhomogeneity along the x direction provides a guiding mechanism for the optical mode confinement in the transverse direction.

A single mode stripe gain-guided laser is very easy to fabricate and much cheaper to produce. The principle of the gain-guided lasers is schematically illustrated in the top of figure [2.10]. The injected current spreads along the transverse direction and the optical mode profile follows the injection current profile. The type of transverse mode operation, i.e. whether single mode or multimode, depends on the stripe width "w" and injection. Fundamental transverse mode operation can be obtained by using small stripe widths and operating the gain-guided device just above the threshold.

2.4.2 Index guided lasers

In gain guided semiconductor lasers, the carrier spreading along the transverse dimension degrades the laser performance, and resulting in a high threshold current density and a low differential quantum efficiency. Moreover, due to lack of built in refractive index step the gain guided laser have poor optical confinement. Precisely, due to antiguiding the optical mode expands instead of confining in these structures. To improve the laser performance, index-guided structures have been developed for a better optical confinement.

The principle of index-guided lasers is schematically illustrated in the center of figure [2.10]. The optical mode propagates through the waveguide structure due to the transverse effective refractive index step Δn_{eff}. The type of transverse mode operation, i.e. whether single mode or multimode, depends on the index step and the width "W" of the waveguide. However, the output power from these devices is considerably less compared to the gain-guided lasers.

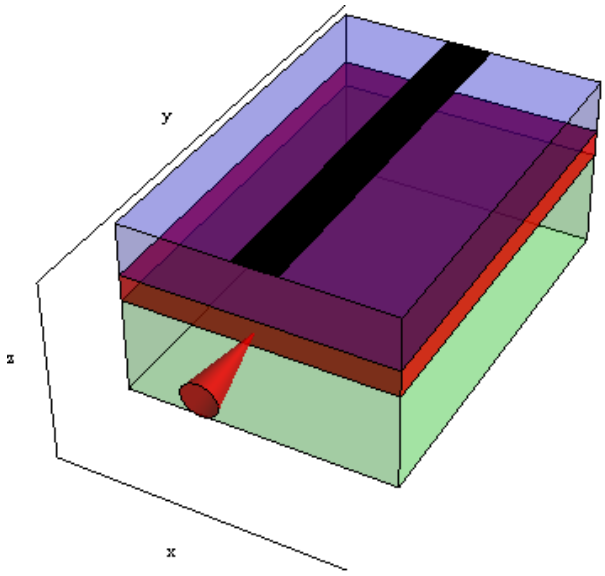

Figure 2.6: Schematic representation of Gain guided $InGaAsP - InP$ heterostructure laser. Metal contact or stripe (black), active region $InGaAsP$ (light red), substrate $n - InP$ (light green), top layer $p - InP$ (light blue) and light output [cone shaped] (red). The laser cavity is in the axial (or longitudinal) direction [y], [z] represents lateral or vertical direction, and [x] denotes transverse direction.

Index guided lasers can broadly divided in two types: weakly index guided lasers and strongly index guided lasers.

2.4.2.1 Weakly index guided lasers

The structures which have a small index step in the transverse direction are called weakly index guided structures, such as ridge waveguide lasers (see figure [2.7]). The index step is achieved by etching a part of the top (cladding) layer. This decreases the effective refractive index in the regions outside of the strip in comparison to the region below the ridge, creating a waveguide along the transverse dimension.

2.4.2.2 Strongly index guided lasers

Strongly index guided lasers usually employ a buried heterostructure (see figure [2.8]). In these structures, the active region is bounded by epitaxially grown layers of lower index both along and normal to the plane of active region. Thus

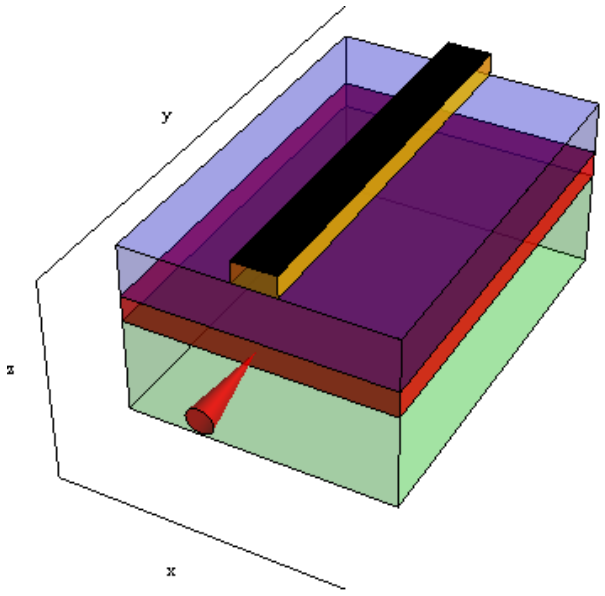

Figure 2.7: Schematic representation of Weakly index guided [Ridge waveguide] $InGaAsP-InP$ heterostructure laser. Metal contact or stripe (black), Waveguide $p-InP$ (yellow), active region $InGaAsP$ (light red), substrate $n-InP$ (light green), top layer $p-InP$ (light blue) and light output [cone shaped] (red). The laser cavity is in the axial (or longitudinal) direction [y], [z] represents lateral or vertical direction, and [x] denotes transverse direction

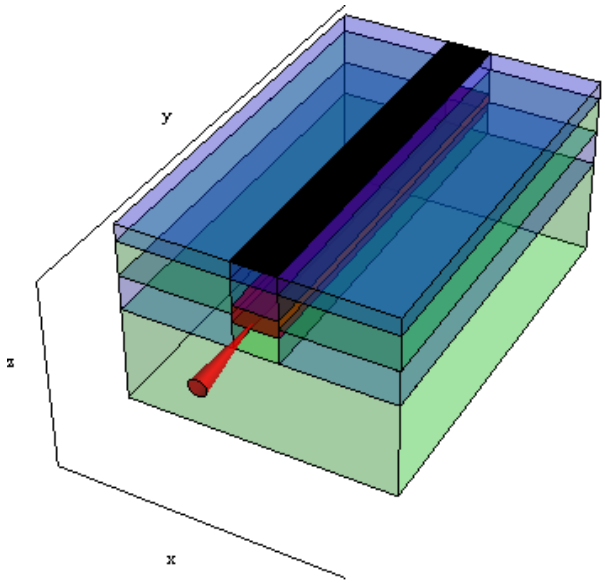

Figure 2.8: Strongly index guided buried $InGaAsP - InP$ heterostructure laser. $n - InP$ (light green), $p - InP$ (light blue), $InGaAsP$ [active region] (red), and light output [cone shaped] (red) and Metal contact (black). The laser cavity is in the axial (or longitudinal) direction [y], [z] represents lateral or vertical direction, and [x] denotes transverse direction.

having a high refractive index and gain waveguide area at the center of the active layer results in an structure similar to optical fiber. These strongly index-guided lasers have a robust beam profiles than that of weakly-index guided and gain-guided lasers.

To summarize the differences between gain-guided and index-guided structures, index-guided devices have small astigmatism, lower threshold current, and usually have a robust output beam profile, often a single transverse mode. However, these structures are more complex to fabricate and therefore more costly. Gain-guided devices have larger astigmatism, higher threshold current, and generally have multiple transverse modes. Nevertheless, these devices are easy to fabricate and are much cheaper to produce. A comparison of gain guided, ridge waveguide and buried heterostructure laser in terms of carrier distribution, refractive index profile, and optical field distribution is shown in figure [2.9].

In conclusion, transverse confinement in semiconductor diode lasers is a very important requirement for realizing single mode operations. Three types of

transverse confinement can be envisioned in diode laser devices, namely: transverse current confinement, transverse optical mode confinement and transverse carrier confinement. For example: gain-guided structures have good transverse current confinement, index guided lasers have a built in refractive index waveguide which offers a good transverse hold on injection current, and optical mode, whereas buried heterostructure offers all three: transverse current, charge carrier, and optical mode confinement [58] (see figure [2.10]).

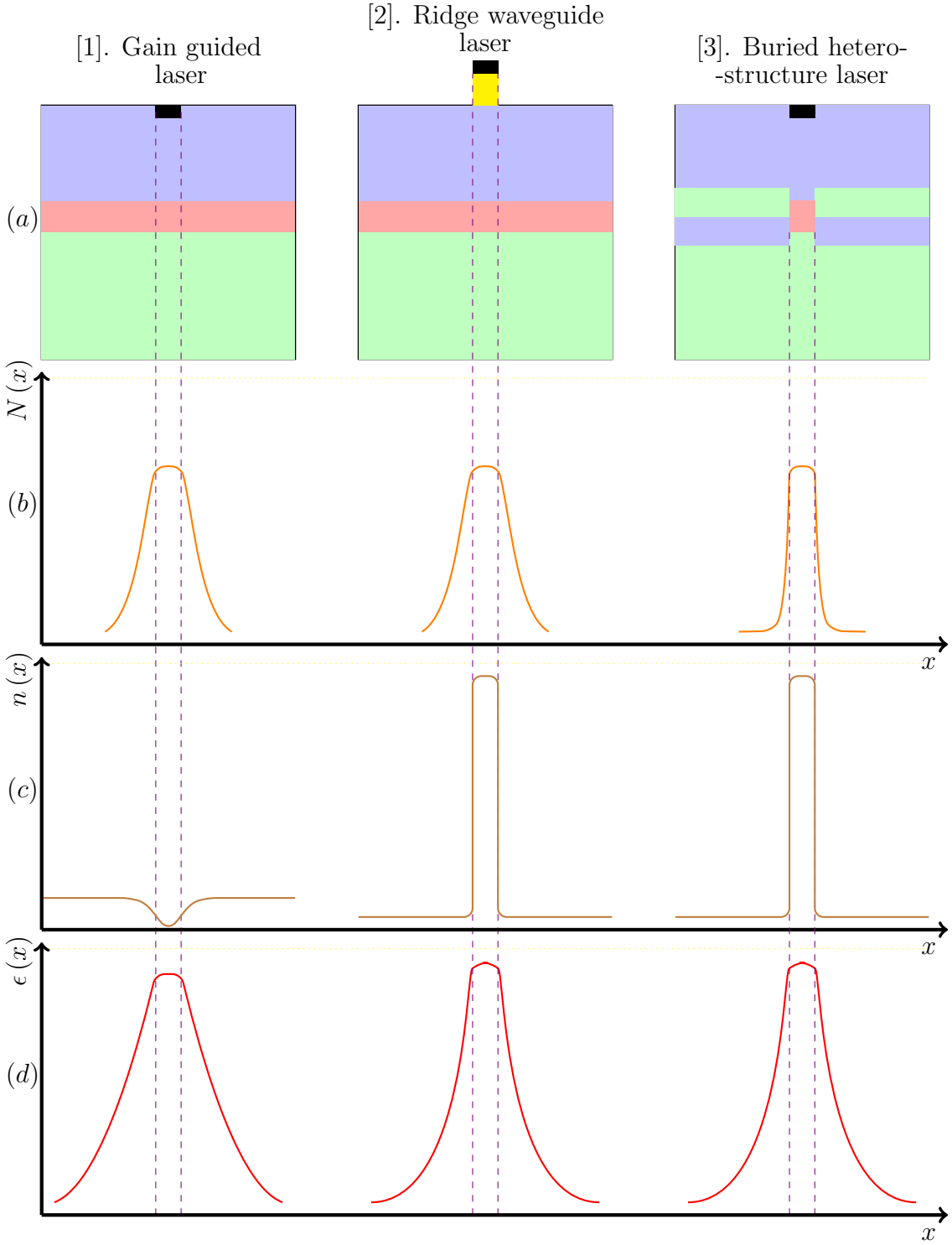

Figure 2.9: Transverse representation of (a) basic structure of (gain guided [1], ridge waveguide [2] and buried heterostructure [3] $InGaAsP-InP$ laser) (b) excess carrier distribution, (c) refractive index profile, and (d) optical field distribution. Metal contact or stripe (black), active region $InGaAsP$ (light red), substrate $n-InP$ (light green), top layer $p-InP$ (light blue), and Waveguide $p-InP$ (yellow).

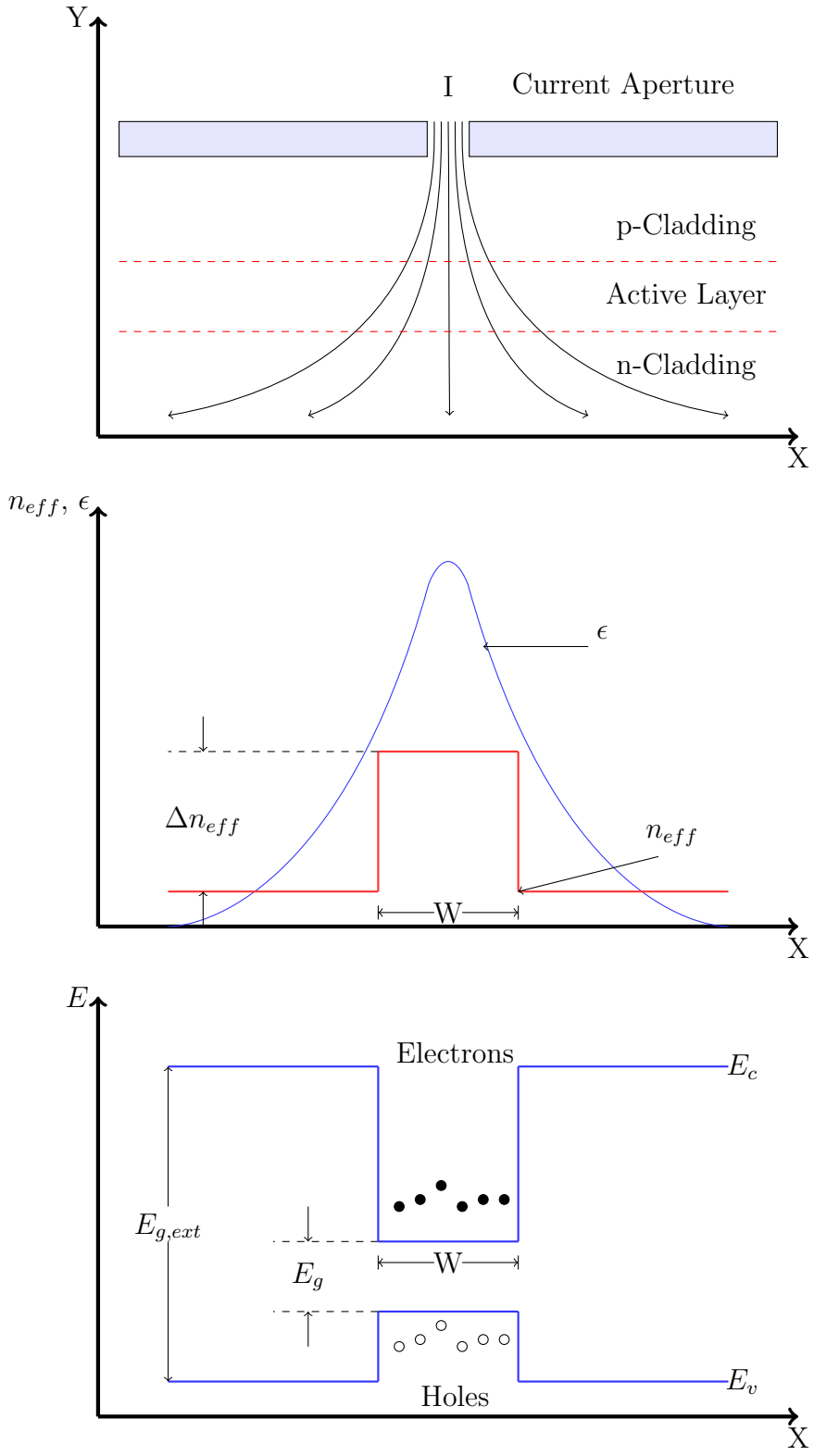

Figure 2.10: Schematic representation of three basic types of transverse confinement. Current confinement (top) : the current (I) is injected through an aperture. Optical confinement (center) : a step in the effective refractive index n_{eff} builds up a dielectric transverse waveguide for the optical mode with intensity "ϵ". Carrier confinement (bottom) : a double heterostructure barrier prevents the transverse diffusion of electrons and holes [58].

Overall, the necessary basic elements to realize a semiconductor diode laser are:

- a medium offering optical gain by stimulated emission,
- a resonator for optical feedback,
- an optical waveguide for the confinement of the photons in the active region,
- a mechanism for the transverse[3] confinement of injected current, carriers and photons.

[3]Note: Some authors use the "transverse" term for the direction of heterostructure grown, instead of the "lateral" term. In this thesis, lateral term is used for the direction of heterostructure grown.

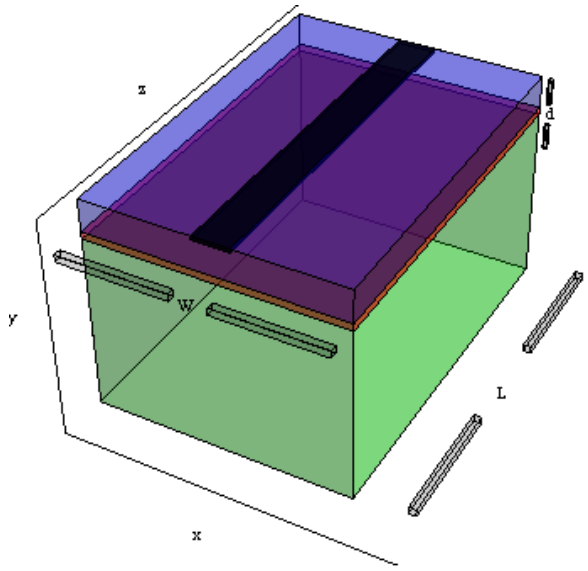

Figure 2.11: Schematic representation of an edge-emitting laser with the coordinate system (x,y,z). The laser cavity is in the axial (or longitudinal) direction [z]. [y] represents lateral or vertical direction, [x] denotes transverse direction, Contact area (black), active region (red), substrate (light green) and top layer (light blue). The active region below the contact area has a axial length (L), transverse width (W) and a vertical height (d).

2.5 Edge-emitting laser with horizontal resonator

Edge-emitting lasers have light output at the edge of the epitaxial structure. Most edge-emitting lasers are stripe-geometry or index guided lasers. The resonator of an edge-emitting laser is usually a horizontal one and the optical waveguide can be either due to a gain-guiding or index-guiding stripe. There are three different kinds of edge-emitting lasers, namely: the FabryPerot laser, the distributed Bragg reflector laser (DBR laser), and the distributed feedback laser (DFB laser). The mirror facets of the edge-emitting laser are formed by cleaving the semiconductor wafer along the crystal planes. If the facets are uncoated then the mirror reflectivities can be around roughly $\sim 30\%$. Normally, a single-stripe edge-emitting structures are used in high power laser diodes [see fig 2.11].

A typical cavity length (L) and stripe width (W) of an edge-emitting laser will range between $300-2000\mu m$ long and $10\mu m$ wide. Due to long cavity length, a large number of longitudinal modes can take part in the lasing process. A typical

free spectral range or the longitudinal mode spacing would be $\sim 100GHz$. In these devices, light propagates through a rectangular waveguide, i.e. along the active layer.

2.6 Carrier induced refractive index change

The charge carriers injected into the active layer of semiconductor laser causes a significant decrease in the refractive index along with a positive increase in the gain. These two changes are correlated and can be quantitatively described.

The complex wave vector (K) can be written as:

$$K = K^{'} + jK^{''} \; with \; K^{'} = \frac{n^{'}\omega}{c} \; and \; K^{''} = \frac{n^{''}\omega}{c} \tag{2.18}$$

Where "ω" represents frequency, "n" denotes refractive index and "c" refers to velocity of light.

The optical electric field (E) propagating in the semiconductor laser can be written as:

$$E = E_0 \, exp\left(jKz + \omega t\right) \; = \; E_0 \, exp\left(j\left(K^{'} + jK^{''}\right)z + \omega t\right) \tag{2.19}$$

or

$$E = \; E_0 \, exp\left(-\frac{n^{''}\omega}{c}z\right) exp\left(j\frac{n^{'}\omega}{c}z + \omega t\right) \tag{2.20}$$

During the propagation the term $exp\left(j\frac{n^{'}\omega}{c}z + \omega t\right)$ has a constant modulus, whereas the real term $exp\left(-\frac{n^{''}\omega}{c}z\right)$ decreases if $n^{''}$ is positive.

The intensity of the radiation propagating through the semiconductor gain medium can be written as:

$$I \simeq |E|^2 \; = \; I_0 \, exp\left(-\frac{2n^{''}\omega}{c}z\right) \; = \; I_0 \, exp\left(-\beta z\right) \tag{2.21}$$

Where $\beta = \frac{2n^{''}\omega}{c}$ is the absorption coefficient, the equation [2.21] is called Beer's law of variation of the intensity.

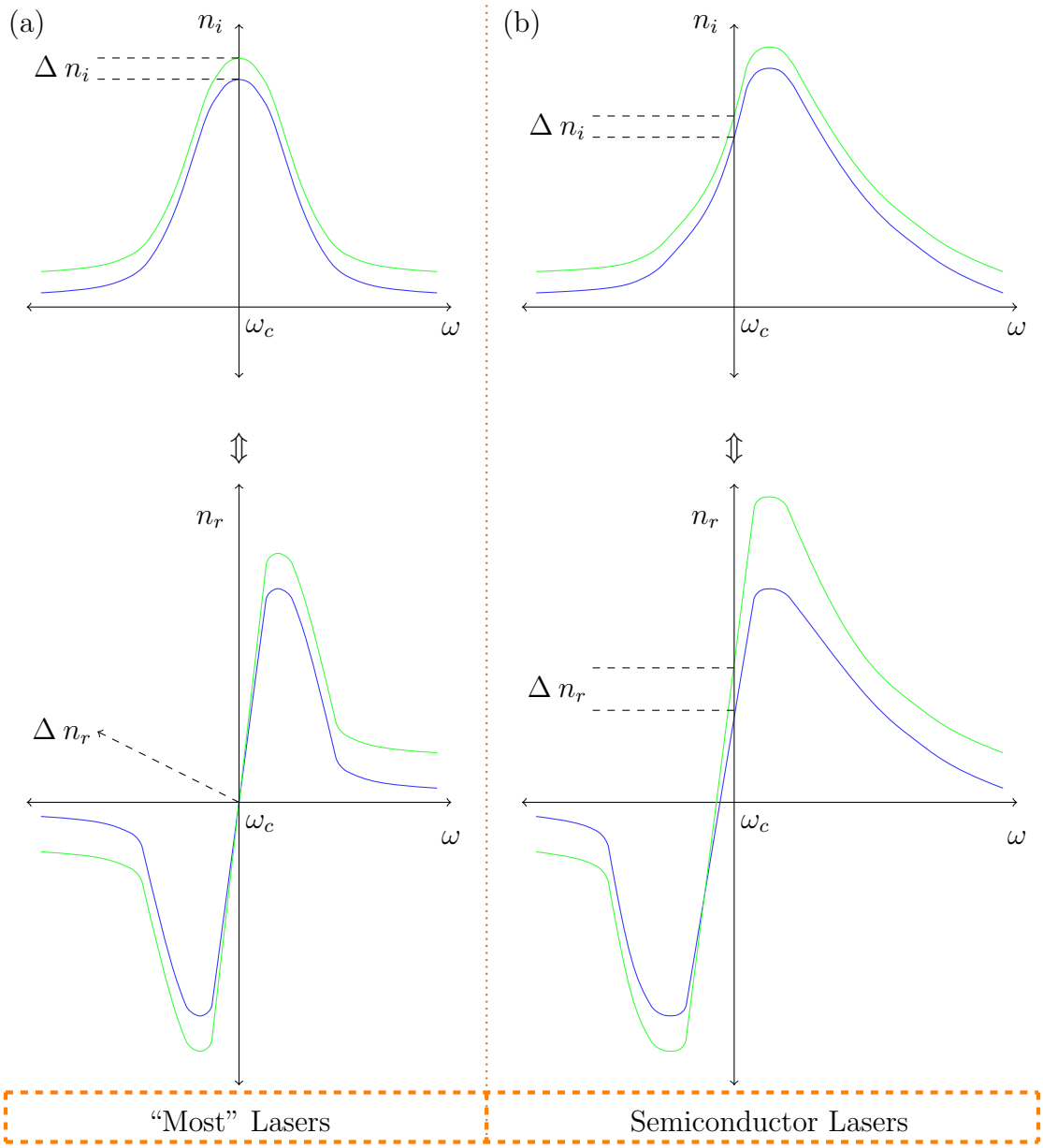

Figure 2.12: Schematic representation of real and imaginary parts of refractive index function for most (gas/solid state) lasers (a) and for a generic semiconductor laser (b). The real and imaginary parts are related by the "Kramers-Kronig" relations.

So the change in the gain due to absorption of light intensity is proportional to the change in the imaginary part of the refractive index $\left(n^{''}\right)$. Whereas, the real part of the refractive index depends on the carrier density.

$$\Delta g = -\frac{2\Delta n^{''}\omega}{c} \; since \; g = -\beta \tag{2.22}$$

The real and imaginary parts of the refractive index are interconnected. Precisely, a small change in the imaginary part of the refractive index may result in a change in the real part of the refractive, and this effect is explained through "Kramers-Kronig" dispersion relations (see figure [2.12]).

For small changes in the refractive index, it can be shown that $\Delta n^{'}$ and the $\Delta n^{''}$ are similarly related [13] [61].

$$\Delta n^{''}\left(E\right) = \frac{2}{\pi} P \int_0^{\infty} \frac{E^{'}\Delta n^{''}\left(E^{'}\right) dE^{'}}{E^{'2} - E^2} \tag{2.23}$$

Where P is the principle value of the integral and E is the energy.

A gain change induced by a change in the carrier density is symmetric in the frequency domain about the peak value for most gas/solid state laser. This implies that there is no change in the imaginary part of the refractive index at the peak gain (where the laser operates). In contrast, the electronic structure of semiconductor materials results in a highly asymmetric gain change due to a change in the carrier density. This entails a lowering of imaginary part of refractive index (through the Kramers-Kronig relations) at the peak gain frequency (see figure [2.12]). Whereas, an increase in the carrier density whether local or non-local decreases the real part of the refractive index for both gas/solid state and semiconductor laser.

2.6.1 Linewidth enhancement (α) factor

The decrease in the carrier density due to stimulated emission triggers an opposite effect on the refractive index. This is called intensity dependent refractive index change, as the increase in the refractive index is caused by stimulated emission. One can see a slight broadening of the spectral bandwidth of the laser. This non-linear effect affects the dynamical properties of semiconductor lasers. To quantify this particular effect Henry introduced linewidth enhancement factor [13].

$$\alpha = -\frac{\frac{\partial \chi^{'}}{\partial N}}{\frac{\partial \chi^{''}}{\partial N}} = -\frac{\frac{\partial n^{'}}{\partial N}}{\frac{\partial n^{''}}{\partial N}} = -\frac{2\omega}{c}\frac{\frac{dn^{'}}{dN}}{\frac{dg}{dN}} = -\frac{4\pi}{\lambda}\frac{\frac{dn^{'}}{dN}}{\frac{dg}{dN}} \tag{2.24}$$

Where $\partial\chi^{'}$ and $\partial\chi^{''}$ represents the carrier dependence of the real and imaginary parts of electric susceptibility. Similarly, $\partial n^{'}$ and $\partial n^{''}$ denotes the carrier dependence of the real and imaginary parts of refractive index, g denotes gain per unit length, λ refers to wavelength , N corresponds to carrier density and ω refers to angular frequency. The minus sign in the equation [2.24] is to ensure that the α factor remain positive, since the refractive index decreases with an increase in the carrier density.

From the above equation [2.24], we can say that α is a proportionality factor relating phase changes with respect to changes in the amplitude gain.

The introduction of α - factor in the BA laser rate equations explains the following phenomenon: broad linewidth, large chirp, onset of coherence collapse induced by optical feedback and filamentation.

There are different ways to measure the α - factor in semiconductor lasers. Some such important techniques are: Amplified Spontaneous Emission (ASE), FM/AM response ratio under small signal current modulation, Pump Probe Measurements and Linewidth Measurements (for further information see paper [15]).

In the QW lasers, the end results from these various α measurement techniques leads to same value in contrast to the QD lasers, where different techniques accounts different output values. It has been reported that such behavior is due to free carrier plasma effects and intrinsic capture/escape dynamics of the QD materials [15]. Measurements in both bulk and quantum well lasers have shown that the α factor can depend strongly on device operating conditions such as carrier density, temperature and frequency as well as epitaxial structure [77].

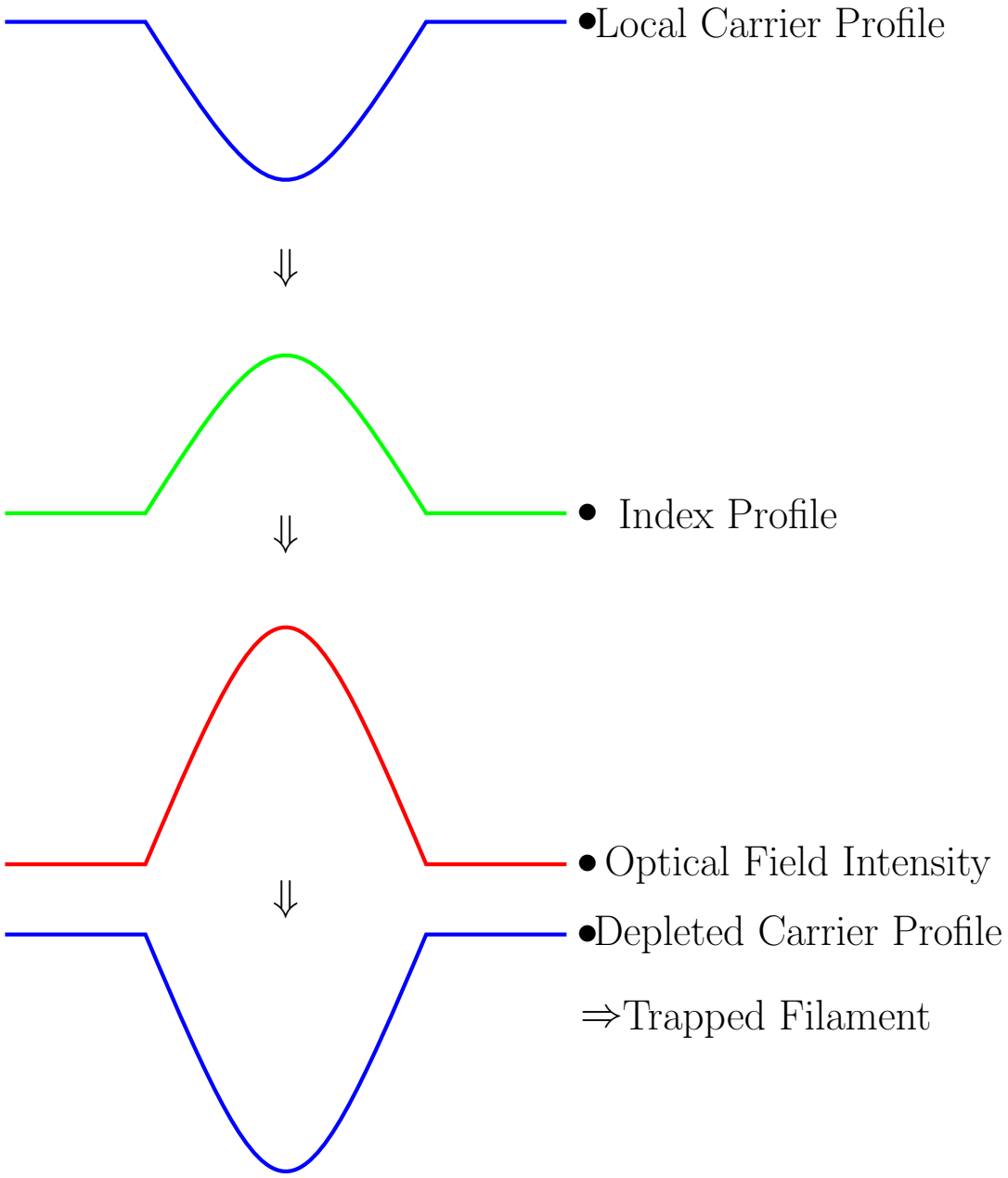

Figure 2.13: Schematic representation of filament formation in broad area semiconductor lasers. Locally, if any carrier (top blue) reduction occurs then it initiates an increase of the refractive index (green) due to the presence of phase-amplitude coupling in the medium. This increase in the refractive index triggers an increase in the local laser light intensity (red). The formation of optical filament occurs when a further rise in the local carrier density (bottom blue) takes place as a result of an increase in the local laser light intensity. However, the absence of light near the adjacent region of the filament causes a localized build-up of carriers, far beyond the equilibrium level. This inherently unstable effect causes the filament to collapse and reform at a different spatial position. Thus, a fast irregular phenomenon in time called filamentation takes place in BA lasers.

2.7 Filamentation

Due to large stripe width, BA lasers suffer from a fast irregular phenomenon in time, where bright spot particles move to and fro in a zigzag manner along the stripe width. This irregular pattern is called filamentation. The width of the moving filament is typically around 10 μm, and it takes several picoseconds to move from one end of the active region to the other. Filamentation is a common problem for wide stripe lasers and for laser arrays. The origins of the dynamic filamentation can be traced back to the effects of self-focusing, diffraction, and spatial hole burning.

2.7.1 Thermal Lensing

Mostly, bulk and high power lasers suffer from thermal lensing effect because of temperature dependent refractive index. This so-called thermal lensing effect causes self-focusing of the radiation in regions of higher temperature leading to uneven optical gain. This nonlinear effect coupled with diffraction move the high intensity spots from one place to another inside the cavity.

There are several methods in use to control unstable filamentary dynamics in a BA laser. These control techniques can be classified generally into two types:

- First, improvements based on the device structure. Example: Quantum Dot active region over Quantum Well active region. Quantum-dot lasers have a strong carrier localization and discrete energy levels, which reduces carrier diffusion. Thus strong transverse confinement of carriers in the QDs leads to much higher spectral purity when compared to quantum wells [59].

- Second, using a control mechanism. Example: (1) injection locking in a master-slave configuration, (2) frequency selective optical feedback, (3) spatial filtering using optical feedback [5].

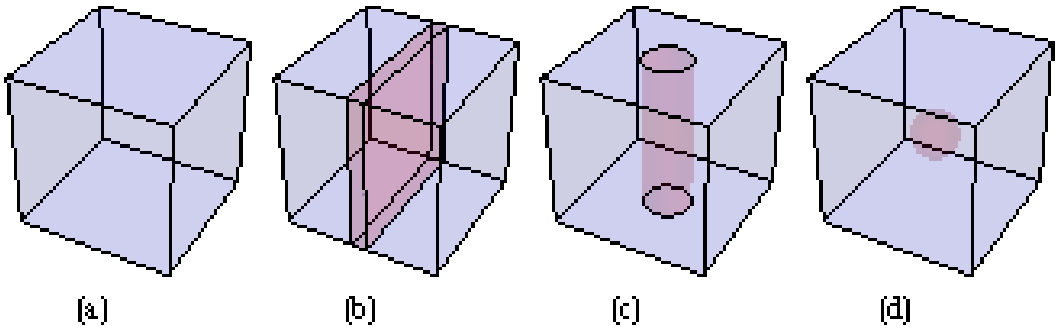

Figure 2.14: Graphical representation of: (a) Bulk semiconductor, (b) Quantum well (c) Quantum wire (d) Quantum dot.

2.8 Low dimensional heterostructures

The emergence of low dimensional heterostructures, such as Quantum Wells (QWs), Quantum wires (QWRs) and Quantum Dots (QDs) offers better carrier confinement. Carriers can be confined in one transverse direction (QWs), two transverse directions (QWRs) or all three dimensions (QDs). As shown in the figure [2.14], a sandwich of the lower bandgap material between two layers of another material having high bandgap results in the formation of QWs, QWRs and QDs.

2.8.1 Quantum confinement

Due to the Coulomb interaction, the electrons in the conduction band and the holes in the valence band interact with each other, forming excitons. Exciton Bohr Radius is the distance between the electron and the hole within an exciton, and it is of few nanometers. If the length of the semiconductor is reduced to the same order as that of exciton Bohr radius, then the properties of exciton changes. This effect is known as quantum confinement. In bulk semiconductors, the exciton can move freely in all directions (i.e. along lateral, longitudinal and vertical dimensions).

Quantum confinement in a semiconductor can be broadly divided into three types based on the confining dimension:

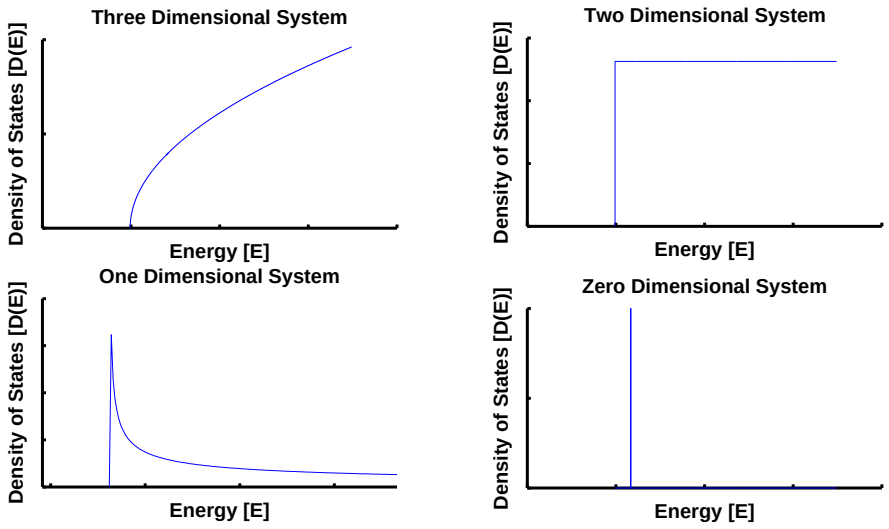

Figure 2.15: Density of states (number of states per unit energy and per unit volume) of one, two, three and zero dimensional systems. The density of states for bulk semiconductor is of parabola and for the quantum well, it is a step function. These two profiles are of continuous in nature. However, in the QDs the density of states is discrete due to δ like density of states.

2.8.1.1 Two dimensional systems

In these systems, energy levels are quantized in the perpendicular direction to the heterostructure layers. Charge carriers (both electrons and holes) move freely in the plane parallel to the heterostructure layers. In other words, semiconductor size is reduced in just one dimension (usually vertical dimension), and the exciton is immobile in that dimension.

Note: The size reduction is of the order of the Fermi wavelength $(L \sim \lambda_f)$. where "L" represents length of the semiconductor and "λ_f" denotes Fermi wavelength.

2.8.1.2 One dimensional systems

Semiconductor size is reduced in two dimensions, and the exciton is immobile in those dimensions.

2.8.1.3 Zero dimensional systems

Semiconductor size is reduced in all three dimensions, and the exciton is immobile in all those directions. These so-called Quantum Dots function like atoms and are very useful in analyzing the atomic properties of semiconductors. Moreover, the guiding idea behind the development of QDs is to have sharp, distinct quantized energy levels in semiconductors just like in atoms (see figure [2.15], [2.12]).

2.9 QDs Size and Distribution in a QD Laser

Theoretically, advantages of QD laser are due to δ like density of states (see fig [2.15]). If all the QDs are of same size and orderly distributed then the gain spectrum of the QD laser will also look like a δ function. However, in the real QD laser structure, the QDs vary in size, shape, composition and local strain [40]. Structural defects in the QDs directly degrade the optical emission by causing fluctuations in the quantized energy levels and there by opening alternative non-radiative carrier recombination channels. This is the main reason behind the inhomogeneous broadening of the gain spectrum in the QDs and the problem could be countered satisfactorily if the produced quantum dots have very narrow size distribution.

2.9.1 Phonon bottleneck

QD laser structures suffer from phonon bottleneck, where the δ like density of states significantly slows down carrier transitions between energy levels in the QD system. For the 1D and 2D cases there is a continuum of states in at least one dimension, whereas in the 0D system all states are fully quantized with a δ like density of states. This results in a very few phonon mediated processes to occur because the phonon energy must exactly match the energy spacing between the QD levels. Furthermore, for a typical QD system, the energy level spacing for

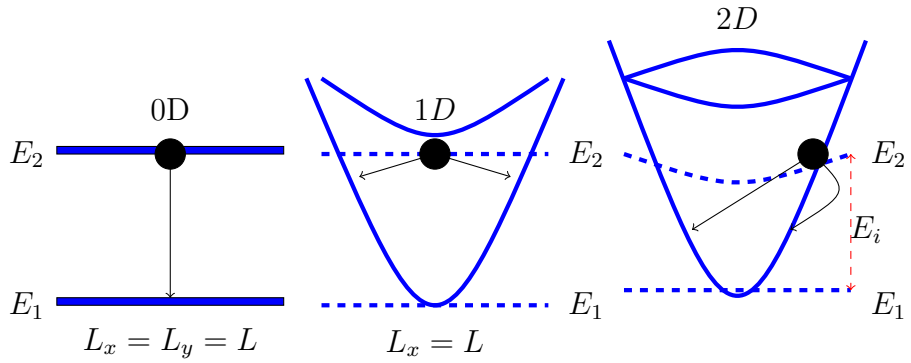

Figure 2.16: Schematic representation of the differences in phonon mediated electron relaxation in 0D, 1D, and 2D structures. In 1D and 2D there are various allowed phonon relaxation transitions of an electron at energy E_i. In 0D, if E_i is greater than the LO phonon energy then no single phonon transitions occurs [78].

QDs with only 1 or 2 levels ends up being larger than the typical LO[4] phonon energy so there is slight opportunity for phonon scattering. In these structures, as the phonon-mediated relaxation paths are almost blocked the excited state carrier lifetimes should lengthen from the $1 - 10\,ps$ measured in QW systems to the nanosecond range predicted for QD systems. Therefore the excited carriers stay longer in the lasing states, which results in the degradation of stimulated emission[79]. Nevertheless, other mechanisms such as Auger interaction[5] can be used to suppress this bottleneck effect [80].

2.9.2 Fabrication of QD Lasers

Modern electronic and optical devices are fabricated through heteroepitaxial technique. In this process, a crystalline film is made to grow on a crystalline substrate or film of another material.

Originally, QDs were made by patterning the QWs, using etching process. This fabrication process further involves regrowing of epitaxial layers on the etched

[4]Optical phonons are often abbreviated as LO and TO phonons, for the longitudinal and transverse varieties respectively.

[5]In this process, the released energy due to recombination of electron and hole is transferred to another electron in the conduction band, which raises to a higher energy level in that band. This second electron eventually comes down to the bottom of the band by releasing excess energy through phonon.

QDs. This led to high defect densities in the device structure, and eventually poor performance triggering a device failure. Nevertheless, fabrication of the defect free QDs came in to prominence with the development of self-organizing effect in heteroepitaxial systems.

The self assembly method of growing QDs is based on the "Stranski-Krastonov (SK) heteroepitaxial growth mode", which in turn is primarily based on the strain effect. This growth mode offers control on both surface densities and size of QDs.

2.9.2.1 Stranski-Krastonov heteroepitaxial growth mode

Epitaxial Growth Modes characterizes the nucleation and the growth process of thin film semiconductors. In SK heteroepitaxial growth mode case, highly strained semiconductors grow epitaxially due to the lattice mismatch between the substrates. The fabrication of QDs using SK heteroepitaxial growth mode first begins with the formation of smooth atomic monolayers, later, formation of islands takes place.

In this thesis work, spatial properties of gain guided (edge emitting) lasers with a injection stripe width of $\sim$ 5 μm, and QDs as active gain medium are studied in detail.

2.10 Classifications of Lasers

Dynamical instabilities occur in all laser types and can usually be reproduced using generic rate equations for the photon number, the population inversion and the material polarization (Maxwell-Bloch equations). As a result, different laser types can be classified according to the difference in relaxation time scales of these three quantities. Moreover, one or more of these rate equations may be adiabatically eliminated due to the difference in time constants (see equations [3.1], [3.2] & [3.3]). Therefore, based upon the scales of the time constants, any laser can be classified into three classes: class A, B, and C lasers [86] [87].

2.10.1 Class C Lasers

The Maxwell-Bloch rate equations involves three coupled rate equations describing the dynamics of the electric field [E], polarization [P], and charge carriers [N]. If the decay rates representing the photon or field [γ_c], population inversion [γ_i] and polarization [$\gamma_\perp$] are all comparable then the dynamics represents a Class C laser. In conclusion, for Class C lasers no adiabatic elimination of time constants is possible.

2.10.2 Class B Lasers

If there exists a large difference in the decay rates [$\gamma_\perp >> \gamma_c$ and $\gamma_\perp >> \gamma_i$], an adiabatic elimination of the polarization rate equation is possible and the dynamics of laser are described by only two coupled rate equations (electric field and charge carriers). Then the rate equations are said to represent Class B lasers. Our QD rate equation model (see chapter [3]) represents a Class B type laser, because the polarization rate equation can be adiabatically eliminated due to fast carrier-carrier and carrier-phonon scattering at room temperature.

2.10.3 Class A Lasers

In Class A lasers, only electric field rate equation represents the dynamics of the laser and the other two are adiabatically eliminated because of good cavity limit conditions [$\gamma_c << \gamma_\perp$ and $\gamma_c << \gamma_i$]. In our steady state beam propagation model (see chapter [4.2]), we assume a very fast relaxation of the carriers and thus this approach represents a Class A type approximation. Nonetheless, the model reproduces the main results of the Class B rate equation approach albeit with a reduced stability range.

2.11 Brightness of a laser

A good performance of a high power laser is assumed on the basis of "Brightness" feature. It is defined as the optical Power density (P) per emission area (A)

and unit solid angle (Ω) in the output beam.

The mathematical representation of the brightness (B) of a laser beam is:

$$B = \left(\frac{P}{A.\Omega}\right) \propto \left(\frac{P}{(W_o.\Theta)^2}\right) = \left(\frac{P}{Q^2}\right) \propto \left(\frac{P}{(M^2)^2}\right) \tag{2.25}$$

Where "Q" points to Beam Parameter product, "W_o" corresponds to beam's minimum diameter, "Θ" symbolizes divergence and "M^2" stands for represents beam parameter product normalized to a fundamental Gaussian mode [6].

M^2 is the prominent attribute of the beam and remains constant even after propagation through any non-aberrated optical system. The spot diameter and the beam divergence angle of a focused high order beam are always higher than that of the Gaussian beam by a factor of M^2. However, for asymmetric and dual lobed beams, the M^2 measurements requires special data processing. Whereas, for non-Gaussian and non-paraxial beams, the M^2 measurements can lead to large errors.

High brightness can be obtained by either increasing the available power or by decreasing the beam parameter product [M^2] (see expression [2.25]). In practice, the above means cannot be achieved by using passive components like lenses, mirrors, pinholes, etc. Nevertheless, it is possible to increase the available brightness of the laser diode by placing the optical source in an external cavity.

Sometimes we are concerned in the spectral brightness (SB) of a diode laser, which can be defined as the ratio of brightness to spectral width [$\Delta\lambda$] (measured at the $\frac{1}{e^2}$ points);

$$SB = \frac{B}{\Delta\lambda} \tag{2.26}$$

High brightness sources are very crucial in certain applications like photodynamic therapy (PDT), and fiber optics because the light beam from these devices can be focused to a small spot by use of simple external optics, whereas high spectral brightness sources are used in frequency doubling, and atom cooling.

In conclusion, high brightness can be obtained from a laser device by maximizing the output power and minimizing the beam divergence or emission area.

[6] **Note:** M^2 is defined in the International Standard ISO: 11146.

Chapter 3

Injection profiling

In self-assembled QD materials, resonant charge carriers reside in the QDs and take part in the lasing process, whereas non-resonant charge carriers populate wetting layer and do not take part in the lasing process. However, both charge carriers contribute to the linewidth enhancement (α) factor (also called anti-guiding factor) [15]. In this chapter, we examine the role of non-resonant carriers in the beam properties of injection profiled lasers and explain the appearance of a characteristic dip at the near field intensity distribution of the QD laser.

3.1 Introduction

3.1.1 Device approach

3.1.1.1 Broad area laser diodes

Gain guided lasers for high power applications typically have injection stripe widths of $\geq 100\,\mu m$ and are called as broad area (BA) laser diodes. Even though broad area laser diodes offer compactness at a reasonably low cost, efficiency, reliability and tunability over a wide range of available wavelength these devices have several shortcomings like divergent beams, elliptical beam profiles and multimode emission. Moreover, standard broad-area waveguide designs are more susceptible to modal instabilities (see figure [3.1] and table [6.1]), filamentation and catastrophic optical mirror damage (COD) than other diode lasers. Due to these effects

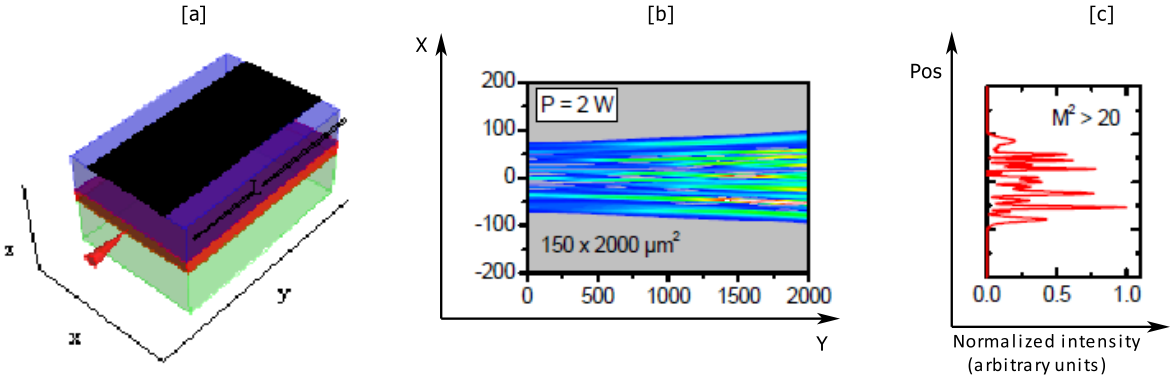

Figure 3.1: Schematic representation of BA ($InGaAsP - InP$) heterostructure laser [a]. Here, Metal contact or [injection] stripe (black), active region $InGaAsP$ (light red), substrate $n - InP$ (light green), top layer $p - InP$ (light blue) and light output [cone shaped] (red). The laser cavity is in the axial (or longitudinal) direction [y], [z] represents lateral or vertical direction, and [x] denotes transverse direction. 2-D representation of optical field inside the BA laser [b]. Here, [y] represents longitudinal direction, [x] denotes transverse direction, and (P) represents output power. Near-field profile [c], where [Pos] refers to position (μm), and (M^2) refers to beam quality [83]

.

BA lasers have a low beam quality. The occurrence of filamentation in broad-area semiconductor lasers can be attributed to to nonlinear mechanisms like carrier induced changes in the refractive index through linewidth enhancement factor, and self-focusing due to thermal induced changes in the refractive index. Whereas, the occurrence of modal instabilities in BA lasers is due to large stripe width (see figure [3.1]). This large stripe width leads to ineffective transverse current confinement. Lastly, the occurrence of COD is due to absorption of light energy near the facets, leading to melting and recrystallization of semiconductor material at the mirrors. Since the BA lasers have large stripe width and are thus designed to generate large powers, the probability of occurrence of catastrophic optical mirror damage is very high.

To obtain high output powers from these BA device, the following requirements are necessary: (1) low internal loss (low threshold and high quantum efficiency), (2) stable transverse mode (no kinks on current-light output power characteristics), (3) high temperature characteristics, (4) no catastrophic optical damage.

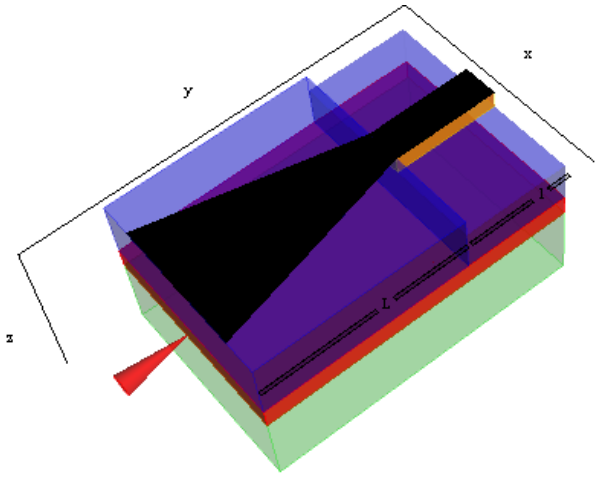

Figure 3.2: Schematic representation of Tapered ($InGaAsP - InP$) heterostructure laser . Metal contact or stripe (black), Waveguide $p - InP$ (yellow), active region $InGaAsP$ (light red), substrate $n - InP$ (light green), top layer $p - InP$ (light blue) and light output [cone shaped] (red). "L" refers to length of taper structure, and "l" represents length of ridge structure. The laser cavity is in the axial (or longitudinal) direction [y]. [z] represents lateral or vertical direction, [x] denotes transverse direction.

3.1.1.2 Tapered devices

In the last few years, a large number of different solutions have been proposed to overcome these problems, where the main effort has been directed to develop broad-area structures that support only one transverse mode, so that high beam quality together with high output power can be obtained. Tapered devices (see figure [3.2]), distributed feedback (DFB) lasers and monolithically integrated master-oscillator-power-amplifiers (MOPAs) are some solutions currently in use. These devices have demonstrated an output power well above $1W$ together with a high beam quality.

A ridge wave guide laser has a high beam quality, but low output power. Whereas, the BA laser has high output power, but low beam quality. The main idea behind the development of tapered lasers is to incorporate both the positive aspects of broad stripe and ridge-waveguide structures. Integrating both ridge waveguide and broad stripe structures in one single device can lead to high output powers

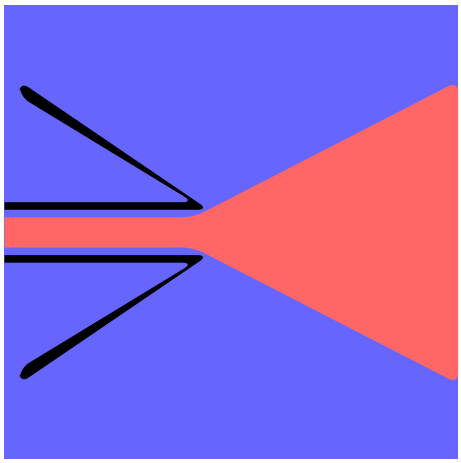

Figure 3.3: Schematic representation of tapered laser oscillator having Cavity-Spoiling grooves (black).

with high beam quality. The basic tapered laser structure has a transverse narrow waveguide structure at the input facet (similar to ridge waveguide structure) and a wider aperture consisting of tapered gain region at the output facet (similar to BA waveguide structure). Both mirror facets are coated with anti-reflection materials in order to suppress any optical resonances. Typically, the output facet reflectivity is less than 1% so that only a small part of the output light is back reflected towards the waveguide section (similar to a spatial mode filter). Further, to suppress Fabry-Perot type electric field oscillations cavity spoiling glooves are placed around the ridge waveguide structure.

One main consideration is to properly maintain the taper angle with respect to the diffraction angle of the propagating beam because the mode pattern of the output beam is very sensitive to the coupling accuracy of the input beam. In conclusion, the basic function of the ridge structure is to provide a good transverse optical mode and that of tapered structure is to provide optical amplification.

In comparison to broad-area laser, the cost of fabricating tapered stripe laser is high [83].

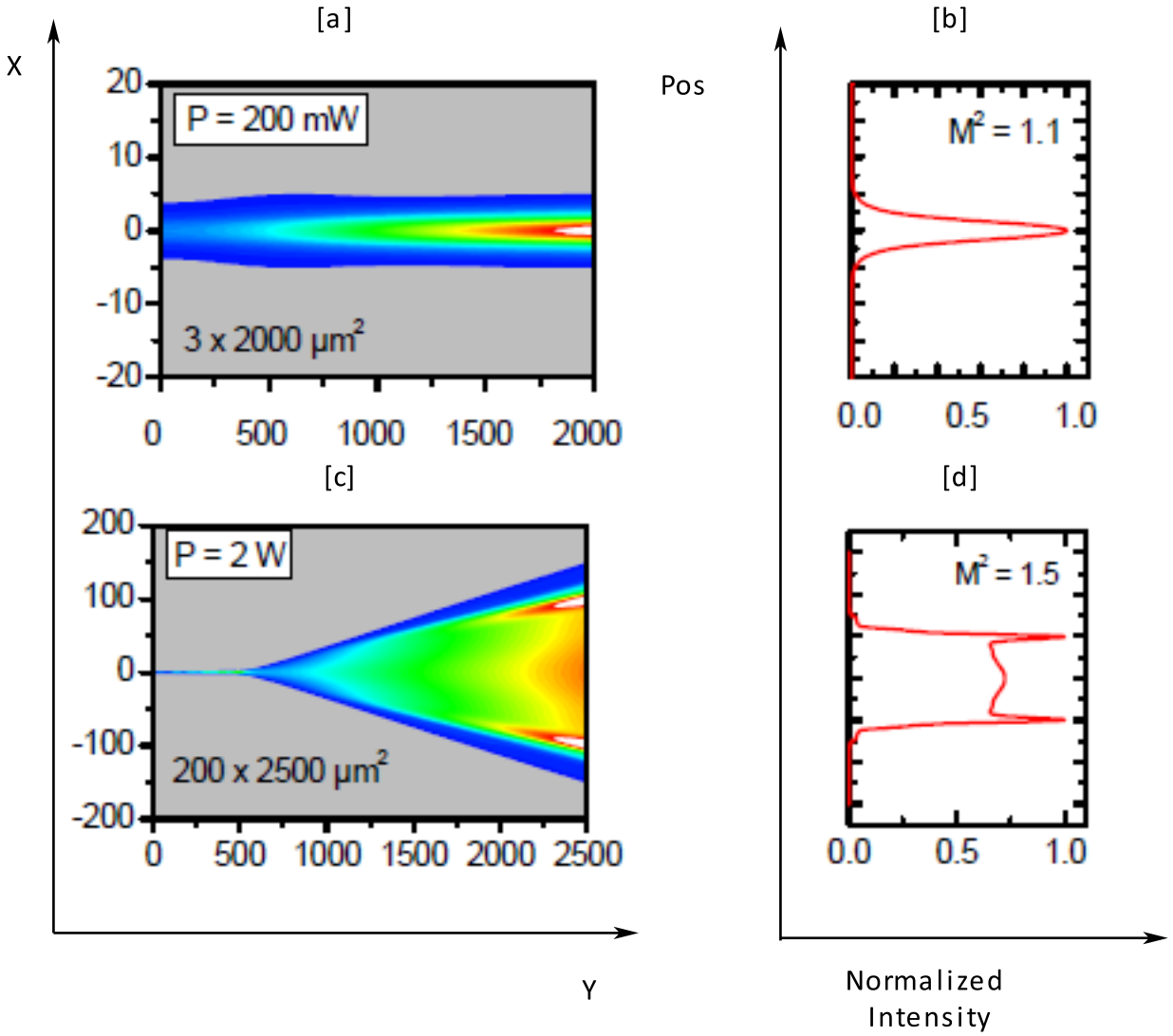

Figure 3.4: 2-D schematic representation of optical field inside the ridge waveguide (a) and tapered laser(c). [b] and [d] represents near-field profile of ridge waveguide and tapered laser respectively. Here, [y] represents longitudinal direction, [x] denotes transverse direction, (P) represents output power, (M^2) refers to beam quality, and Pos denotes position (μm) [83].

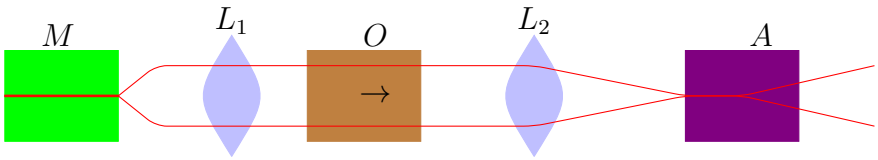

Figure 3.5: Schematic representation of master oscillator power amplifier (MOPAS), where an output power of 4 W can be obtained from master laser. M represents master laser oscillator [green], O refers to optical isolator [brown], A denotes optical amplifier [violet], and L_1 & L_2 refers to collimating lens.

3.1.1.3 Master oscillator power amplifier

In a master oscillator power amplifier (MOPA), an optical amplifier is used to boost the output power from the master laser (or seed laser) and the configuration is called MOPA (see figure [3.5]). Regarding the performance features like linewidth, wavelength tuning range, beam quality or pulse duration, the MOPA's have an edge over other semiconductor lasers. This is due to decoupling of various performance aspects, which adds extra flexibility. For example: it may be beneficial to modulate the low-power seed laser, or to use an optical modulator between seed laser and power amplifier, rather than to modulate a high-power device directly (refer figure [3.5]). Moreover, the optical intensities are comparatively much lower in an amplifier than in a laser because of absence of optical cavity.

On the other hand a MOPA type laser requires a complex optical setup and are prone to back-reflections. This presents a serious limitation for high-power pulsed devices. Moreover, MOPA's have high laser noise.

3.1.1.4 Distributed feedback laser

Most of the semiconductor lasers that have been described so far have Fabry-Perot cavities, whereas a distributive feedback (DFB) laser have Bragg-type diffraction grating, which provides optical feedback for the laser (see figure [3.6]). Here, the optical grating is just above the active region and is enforced over the entire active region which is going to be pumped. The guiding idea behind the keeping of corrugated grating outside the active region is to separate the perturbed

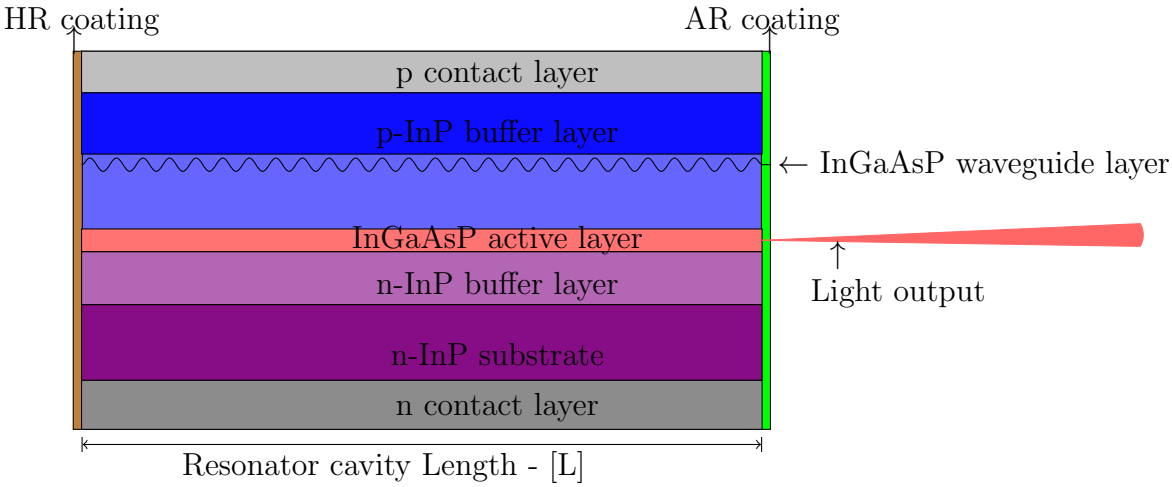

Figure 3.6: Schematic representation of distributed feedback (DFB) laser's cross-section.

regions from the laser medium. However, this has proved to be lossy because of optical absorption in the distributed grating regions.

The corrugated grating in the DFB laser is fabricated by etching the cladding layer adjacent to the active layer and the grating period can be through the Bragg condition. This corrugated grating at both ends of the laser acts as mirrors due to reflections at the selected wavelength.

The output power from the commercial DFB lasers ranges from 10 to 200 mW [92]. Whereas, the maximum output power from the MOPA consisting of DFB laser and fiber amplifier was $> 3W$ [91]

Fabricating a DFB laser is a complicated process because of uncontrollable grating phase at the laser facets. In comparison to DFB laser, a BA laser is easier to fabricate.

3.1.1.5 Our approach

To access broad width of the active region, the BA lasers have broad stripe width ($\sim$ 100 μm) which is about twenty times larger than the edge-emitting

semiconductor lasers) [5]. This design structure leads to poor transverse current confinement (refer figure [2.10]) and in turn leads to low beam quality due to multimode emission. To overcome this problem a technique called "Injection current profiling" has been proposed and successfully demonstrated on QW lasers [9]. Using this injection current profiling technique, broad width of the active region can be accessed from small stripe widths ($\sim$ 5 μm). In this technique, the injection current is spatially varied from a flat plane profile at the injection contact region to a smooth Lorentzian profile at the active region of the laser. Similar to gain guided lasers, the Lorentzian injection profile induces a transverse antiguide in the structure which holds the optical mode. This technique can be achieved by either patterning the contact electrode of the device [27] or through by including an additional current spreading layer [9] [16]. In the current study, the later technique has been carried out. However, both techniques provide coherent output in the pulsed regime, but operation in the CW regime results in the cancellation of the anti-guide due to an induced thermal guide, which in turn leads to unstable filamentary operation [9]. Finally, injection current profiling can be termed as internal control mechanism mainly used to suppress the filamentation in gain guided laser.

The other main problem with BA lasers is catastrophic optical damage. One of the solution currently in use is the utilization of quantum dot materials as the active region in semiconductor lasers. These heterostructures are known to reduce the surface charge carrier diffusion leading to a larger COD threshold. [39]

3.1.2 Epitaxial structure and device

The epitaxial structure for our device was provided by Innolume (formerly Nanosemiconductor GMBH) and contained 10 layers of MBE grown $InAs$ QDs on a $GaAs$ substrate. Each QD layer was formed by growing an 0.8 nm thick $InAs$ QD layer on a 33 nm thick $GaAs$ wetting layer and capped with a 5nm thick layer of $In_{0.15}Ga_{0.85}As$. Adjoining the active region was a 500 nm thick $Al_{0.35} - Ga_{0.65}As$ n-(p-)type $Si(C)$ doped layer ($5 \times 10^{17}\ cm^{-3}$), a 1000 nm thick $Al_{0.35}Ga_{0.65}As$ n-(p-)type $Si(C)$ doped layer ($1 \times 10^{18}\ cm^{-3}$) and a 15 nm thick $Al_xGa_{1-x}As$ (x graded from 0.35 to 0) layer, n-(p-)type $Si(C)$ doped to $3 \times 10^{18}\ cm^{-3}$. The n-

side contained an additional 300 nm thick $GaAs$ layer doped to $3 \times 10^{18} cm^{-3}$. To achieve current spreading p-side contained a 2000 nm thick $GaAs$ layer doped to $2 \times 10^{19}\ cm^{-3}$ and a 100 nm thick capping layer, doped to $1 \times 10^{20}\ cm^{-3}$. One noted distinction here is that the previously used spreading layer was an MOVPE grown 10 μm thick, 4×10^{18} doped $GaAs$ layer [9]; to achieve spreading in the MBE grown QD wafer, a thinner, more highly doped layer was used. Broad area lasers were fabricated by defining the width of the injection stripes (see figure [3.1]) and devices of two different lengths, 1.5 mm and 3 mm were tested.

3.2 Experimental results

For an injection stripe of 5 μm, the resulted carrier spreading in the active region is 120μm (see figure [3.7]). It was shown experimentally that the continuous-wave mode operation resulted in the development of a thermally-induced positive waveguide, which neutralized the carrier-induced anti-guide for increasing injection currents and thereby collapsed the stable non-linear mode of the cavity [9]. Therefore to avoid the unstable filamentary dynamics, the experimental device was operated in pulsed regime (1 kHz repetition rate, 100 ns pulse width).

The near-field intensity profiles for various injection currents are shown in figure [3.7] for the above QD laser. Below threshold regime, the near-field displays a smooth, bell shaped profile which is similar to the smoothened carrier profile in the active region due to the current spreading layer as mentioned previously. Slightly above threshold regime, the near-field intensity profile follows the injection current profile apart from a central dip where very little light is present. Such a near-field profile is not similar to that observed in the QW case but the far-field consists of dual lobes which is similar to QW case[16].

At high injection currents, the symmetric near-field profile slowly manifests in to a asymmetric one around the optical axis and the defect region begins to fill in. At 2.5 A, the beam waist of the near-field profile exhibit enough evidence to declare the output as unstable one. The formation of filament-like structures in the central region and the onset of coherence collapse starts from the 1.7 A

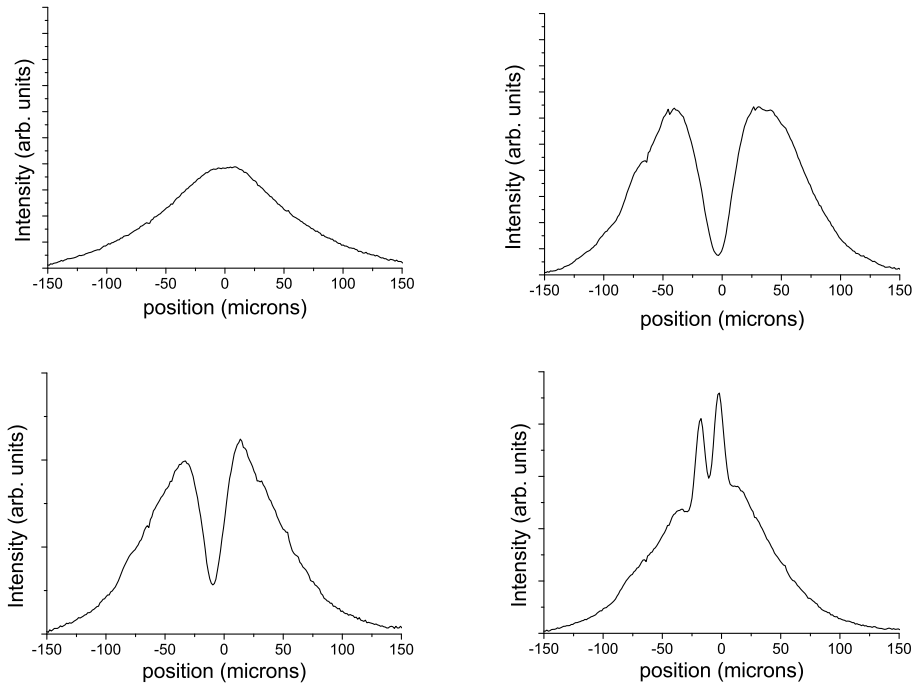

Figure 3.7: Experimentally obtained near field intensity distributions for various currents in an injection profiled quantum dot laser of length 1.5 mm. Note the appearance of a strong dip in the centre of the device which coincides with stable operation (top left - 120mA below threshold, top right - 1.2A, coherent output, bottom left - 2A coherent output, bottom right - 2.5A unstable output

injection current (see figure [3.8]). This particular onset of excited state lasing has been reported previously in QD structures [30], where enough reasons have been provided to explain the excited state lasing effect in QD structures. The onset of two state lasing is generally accompanied by an increase in the phase-amplitude coupling [34].

To understand the beam properties of the QD injection profiled device and, in particular, the appearance of the dip or defect in the near field we constructed a rate equation model.

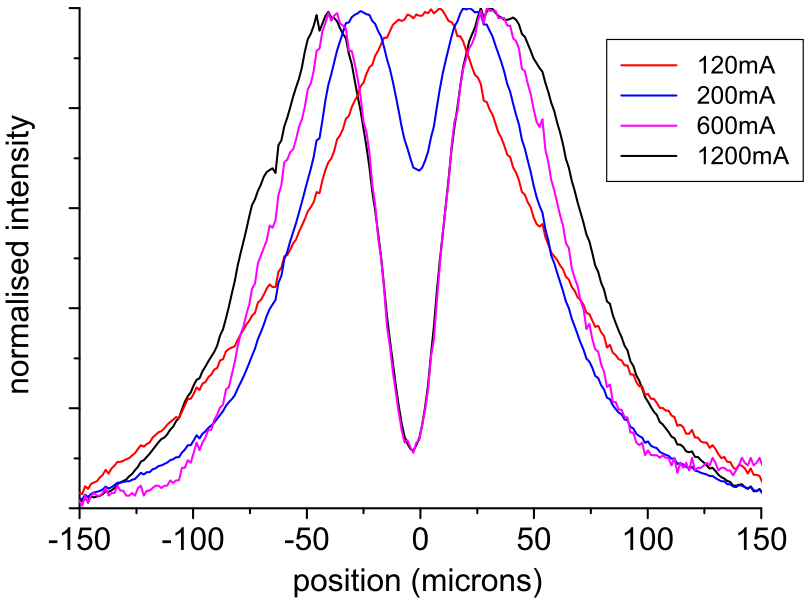

Figure 3.8: Experimental normalized time averaged near field intensities at different injection levels. Note the gradual emergence of the central dip as the injection level increases to 600 mA. Similar behaviour is seen in the simulation.

3.3 Semiconductor laser modelling

There are several ways of modelling the optical, electronic, thermal and gain features of the laser diode. However, one main consideration is choosing a right model. In the below section, an illustration of few ways of modelling the laser diode are presented.

In 0D modelling, Photon carrier rate equations are used to investigate the turn on transient features of the laser diode. In 1D modelling, rate equations representing either vertical (lateral) or transverse or longitudinal dimension of the semiconductor laser are numerically simulated to obtain dynamic characteristics. In 2D modelling, rate equation representing a combination of two dimensions are used to examine the dynamic characteristics. In 3D, rate equation representing all three dimensions are used to probe dynamic features of the SLs. The foregoing models vary in complexity in both theoretically and simulation wise.

The purpose of analyzing the transverse section of QD diode laser is to study the phase-amplitude coupling of emitted radiation with the active gain material. So in our present numerical analysis, [1D] rate equations representing the transverse dimension have been used. The propagation along the longitudinal dimension is neglected for the time being because earlier studies of injection profiling in QW devices showed that longitudinal mode dynamics are largely insignificant [52].

Spatially extended QD semiconductor laser models vary in complexity, ranging from a less complicated rate equation models [81], [82] to full spatio-temporal multi-mode MaxwellBloch approach where the material parameters are derived from microscopic calculations. For example, the study did on the InAs QDs verifies the sensitive dependence of ground state optical matrix element on QDs size and shape [49]. Therefore, introducing additional parameters to represent non-resonant levels and carrier transport among different sized dots will lead to a complex model to simulate. So in our rate equation model, we restricted the rate equations to a single dot state ρ, and a single non-resonant population N. The current QD laser model is a spatial extension of rate equation model (including parameter values) investigated by Melnik et al. [15]. In that paper, it was reported that due to free carrier plasma effects and intrinsic capture/escape dynamics of

quantum dot materials, the α measurement techniques report different values for QD lasers, particularly in the case where the dots population becomes saturated.

Due to Pauli blocking, the number of available states in the dot are limited. In addition, the occupancy of the dot plays a major part on the capture rate of charge carrier. Therefore, the model is based on the assumption that the carriers are directly injected into the wetting layer (WL) of the device, so that they can be captured into the QDs. Furthermore, the model neglects the charge carrier transport within the active region. A similar approximation was used in the examination of injection profiled QW devices [28].

Mathematically, the rate equations for the occupancy of the QD (ρ), WL carrier density (N), and electric field (E) can be written as:

$$\frac{\partial \rho}{\partial t} = -\gamma_d \rho + CN\left(1-\rho\right) - v_g \sigma \left(2\rho - 1\right)\left|E\right|^2 \tag{3.1}$$

$$\frac{\partial N}{\partial t} = \frac{J\left(x\right)}{q} - \gamma_n N - 2CN\left(1-\rho\right) \tag{3.2}$$

$$\frac{\partial E}{\partial t} = -\frac{1}{2}\gamma_s E + \frac{1}{2}(1+i\alpha_d) v_g g_0 \left(2\rho - 1\right) E + i\alpha_{nr} v_g g_0 N E + iD_e \frac{\partial^2 E}{\partial x^2} \tag{3.3}$$

Where γ_n , γ_d are the non-radiative decay rates for carriers in the WL and dot respectively, C is the capture rate from wetting layer into an empty dot, $J\left(x\right)$ is the spatially varying injection current per dot (a Lorentzian shape is used throughout), v_g is the group velocity, σ is the cross section of interaction of the carriers in a dot with the electric field, q is elementary charge, E is the complex amplitude of the electric field in the cavity normalized to the photon density $S = \left|E\right|^2$, γ_s is the photon decay rate in the cavity, g_0 the differential gain, α_d and α_{nr} describe the change of refractive index with change of dot carrier population and with non-resonant population respectively and $D_e = \frac{c}{2k_0\eta^2}$ refers to the diffraction coefficient of light (where k_0 represents the wavenumber in the vacuum, c is the velocity of light and η is the effective refractive index).

To accommodate the reported behaviour of long and short injection profiled QD laser devices [16], we numerically simulated the rate equations for saturated

Table 3.1: Parameters used in the model corresponding to a 60% contribution from non-resonant carriers to α_{th}

$\gamma_n = \gamma_d = 10^{-3}\ (ps)^{-1}$		
$\gamma_s = 0.3\ (ps)^{-1}$		
$v_g = 167 * 10^6\ \frac{m}{s}$		
$C = 10^{-1}\ (ps)^{-1}$		
$\lambda = 1310nm$		
$\eta = 3.5$		
For $\rho_{th} = 0.9$	$g_0 = 22.5\ (cm)^{-1}$	$\sigma = 1.88 * 10^{-7}\ (\mu m)^2$
$\alpha_{th} = 3$	$\alpha_d = 1.2$	$\alpha_{nr} = 0.45$
For $\rho_{th} = 0.6$	$g_0 = 90\ (cm)^{-1}$	$\sigma = 7.5 * 10^{-7}\ (\mu m)^2$
$\alpha_{th} = 1.5$	$\alpha_d = 0.6$	$\alpha_{nr} = 14.4$

Table 3.2: J_{th} value for different α values.

For $\alpha = 0$	$= 3$	$= 6$	$= 9$
$J_{th} = 2.85 * 10^{-10}\left(\frac{coulombs}{sec}\right)$	$= 2.6 * 10^{-10}\left(\frac{coulombs}{sec}\right)$	$= 2.3 * 10^{-10}\left(\frac{coulombs}{sec}\right)$	$= 2.15 * 10^{-10}\left(\frac{coulombs}{sec}\right)$

case ($\rho = 0.9$) and unsaturated case ($\rho = 0.6$). These saturated and unsaturated cases correspond to short and long devices respectively.

The saturated case is operated at $\alpha = 3$ value and the unsaturated case at $\alpha = 1.5$ which are in correspondence to the published experimental results, where α at the threshold (α_{th}) varies from 1.5 to 3 when going from long to short devices [51]. Moreover, in our sensitive analysis of rate equation parameters the contribution of non-resonant charge carriers has been varied from 40% to 60%, which agree to the experimental results published in the paper [44].

The threshold α factor of the QD laser may be described as:

$$\alpha_{th} = \alpha_d + \alpha_{nr}\left(\frac{\delta N}{\delta \rho}\right)\ and\ \frac{\delta N}{\delta \rho} = \frac{\gamma_d}{(C(1-\rho_{th})^2)}, \tag{3.4}$$

In above equation "α_{th}" is the dot population at the laser threshold.

3.4 Results

3.4.1 Simulation results: Rate equation approach

3.4.1.1 Narrow injection profiles

A snapshot of the simulation output features are shown in Fig [3.9] for $\rho_{th} = 0.6$, $J_{th} = 6J_{th}$. Here, the near field intensity follows the pump profile and consists of two spatially separated counter-propagating traveling waves resulting in distinct, off-axis emission in the far field, stabilized by a carrier induced anti-guide, which is very similar to the previous studies on QW case [28]. This behaviour stays on up to $\sim 8J_{th}$, thereafter the onset of filamentary dynamics occurs. A similar pattern was observed for the saturated case where the instability level increases to $\sim 24J_{th}$.

However, there is one significant observations that differentiate the saturated case output features from the unsaturated one. The steady state non-resonant carrier profiles are substantially narrower than the injection profile. This implicates that the carrier capture rate is lowered due to Pauli blocking in the saturated case leading to a buildup of non-resonant carriers in the centre of the device, thereby narrowing the non-resonant carrier profile (see figure [3.11]). This cascades into a stable asymmetric output behaviour at high injection currents (see figure [3.10]). A similar symmetry breaking was noticed for QW injection profiled lasers with a broad flat central pump region [25], where the source of the traveling waves in the near field moves from the centre to one of the edges of the injection profile.

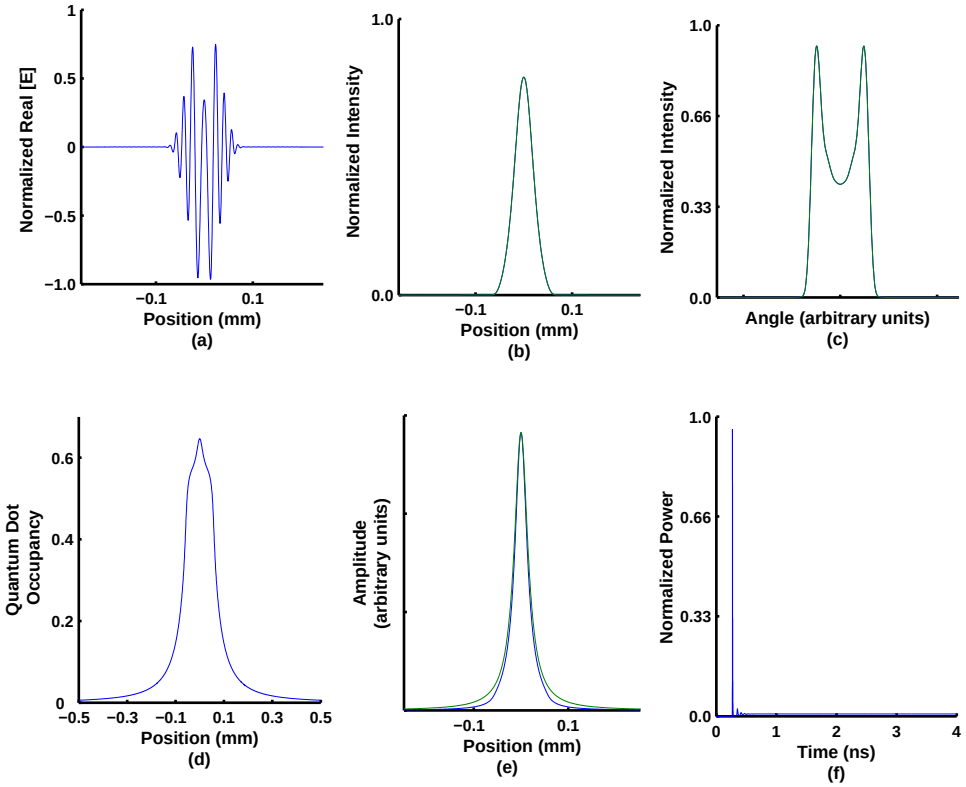

Figure 3.9: Simulated beam properties of QD laser using rate equation approach for a 35 μm wide Lorentzian injection profile in the unsaturated regime ($\rho_{ss} = 0.6$) at $6J_{th}$ and $\alpha = 1.5$. (a) Instantaneous near field electric field (b) instantaneous (blue) and time averaged (green) near field intensities (c) instantaneous (blue) and time averaged (green) far field intensities (d) QD occupancy (e) normalized injection profile (green) and non-resonant carrier profile (blue) (f) normalized output power as a function of time.

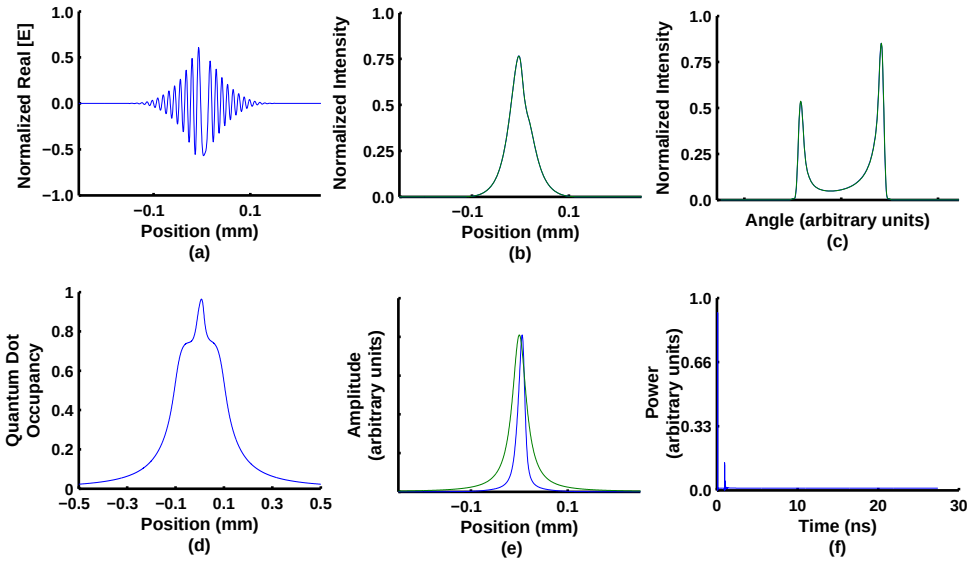

Figure 3.10: Simulated beam properties of QD laser using rate equation approach for a 35 μm wide Lorentzian injection profile in the saturated regime ($\rho_{ss} = 0.9$) at $18J_{th}$ and $\alpha = 3$. (a) Instantaneous near field electric field (b) instantaneous (blue) and time averaged (green) near field intensities (c) instantaneous (blue) and time averaged (green) far field intensities (d) QD occupancy (e) normalized injection profile (green) and non-resonant carrier profile (blue) (f) normalized output power as a function of time, Note asymmetric behaviour in near and far fields, and carrier densities.

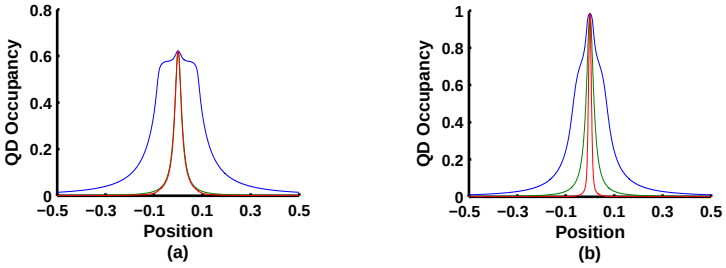

Figure 3.11: Injection profile (green) and non-resonant carrier profile (red), both normalized to QD occupancy (blue), compared for (a) unsaturated and (b) saturated regimes. Note the significant narrowing of the non-resonant carrier profile in the saturated case. Injection levels were $5J_{th}$ for unsaturated case and $8J_{th}$ for saturated case of QD laser using rate equation approach .

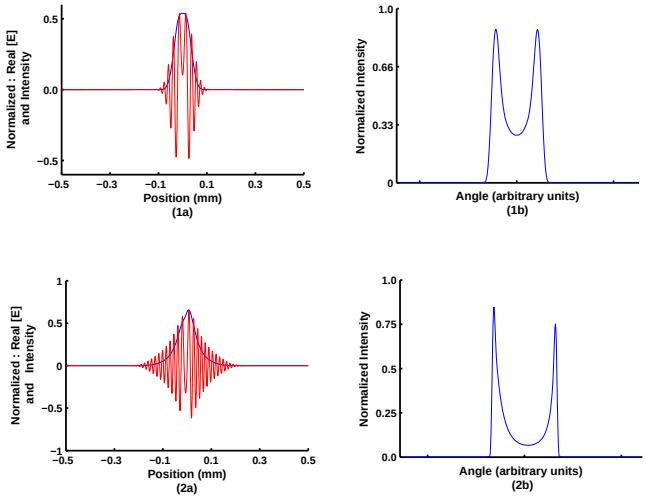

Figure 3.12: Simulated beam properties of QD laser using rate equation approach for a 70 μm wide Lorentzian injection profile in the saturated regime ($\rho_{ss} = 0.9$) at low ($3J_{th}$) and high ($16J_{th}$) injection levels. 1(a) and 2(a) contain near field electric field (red) and near field intensity (blue) for low (1(a)) and high (2(a)) injection levels. 1(b) and 2(b) contain the far field intensities for low and high injection respectively. Note the asymmetric behaviour at high injection.

3.4.1.2 Wide injection profiles

The following step was to simulate the wider $70\,\mu m$ injection profiles which occurred in the experiment. For the parameters outlined in table [3.1] and [3.2], the output features in the case of wider injection profile for both saturated and unsaturated dot cases were very similar to the narrower injection profile. An illustration of this for the saturated case is shown in Fig [3.12] for low and high injection currents. The output pattern consists of a single lobed near field and dual lobed far field. Once more, the steady state non-resonant carrier profiles are considerably narrower than the injection profile in the saturated case, as compared to the unsaturated one. Moreover, the symmetry breaking occurred in the near, and the far fields in a similar fashion to the narrow pump case.

High values for the phase amplitude coupling have been reported in the saturated regime, where two state lasing occurs [34]. Therefore, when the anti-guiding factor is increased from 3 to 9, an interesting features develops in the saturated case. A further narrowing of the non-resonant carrier profile accompanied by a large dip in the near field intensity were observed. The manifestation of such a dip in the near field intensity profile (see fig [3.13]) strongly correlates with the experimental one (see fig [3.7]). The gradual emergence of such a characteristic dip in the near field is due to both high injection currents and an increase in the anti-guiding due to α_{nr} term. In an interesting manner, a very similar pattern occurs in the experiment as shown in Fig [3.8], where the level of the dip increases with the injection current. In addition, some asymmetry comes into sight at increased injection (see figure [3.8]), such asymmetry also observed in the simulation at high injection levels. It is important to highlight that, in the simulation, such a characteristic dip in the near field does not happens for the unsaturated case, when the α is at 9. This may be due to lack of narrowness in the non-resonant carrier profile in the unsaturated case even at high α factor.

Even for wider injection profiles, up to $130\,\mu m$, the behaviour observed for the $70\,\mu m$ injection case persists. A symmetric traveling wave solution happens in the unsaturated case, whereas in the saturated case, the stable solution is typically asymmetric as before and includes a strong dip in intensity due to non-resonant

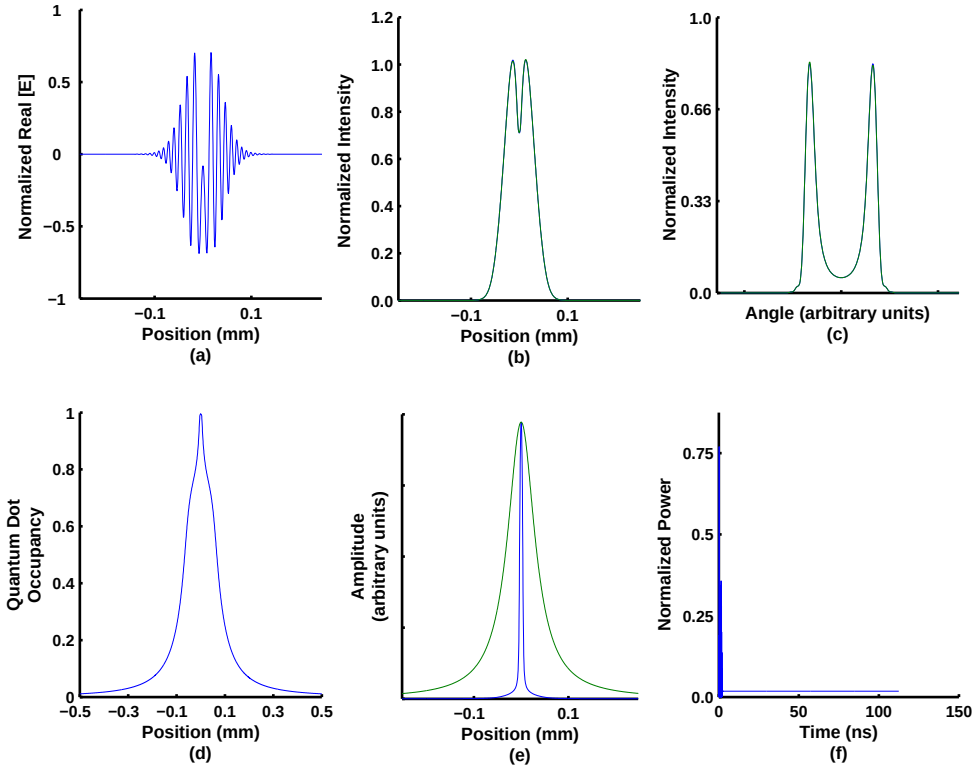

Figure 3.13: Simulated beam properties of QD laser using rate equation approach for a 70 μm wide Lorentzian injection profile in the saturated regime at increased phase amplitude coupling ($\alpha_{th} = 9$, injection level 9.5 J_{th}). (a) Instantaneous near field electric field (b) instantaneous (blue) and time averaged (green) near field intensities (c) instantaneous (blue) and time averaged (green) far field intensities (d) QD occupancy (e) normalized injection profile (green) and non-resonant carrier profile (blue) (f) normalized output power as a function of time, Note presence of a strong dip on the centre of the near field, similar to the experimental dip seen on figure 1.

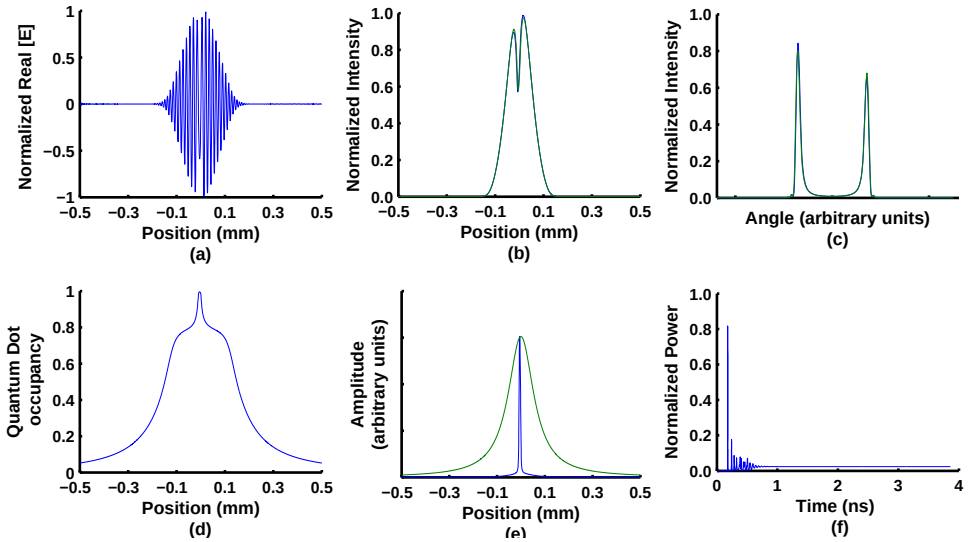

Figure 3.14: Simulated beam properties of QD laser using rate equation approach for a 130 μm wide Lorentzian injection profile in the saturated regime at increased phase amplitude coupling ($\alpha_{th} = 9$, injection level $3J_{th}$). (a) Instantaneous near field electric field (b) instantaneous (blue) and time averaged (green) near field intensities (c) instantaneous (blue) and time averaged (green) far field intensities (d) QD occupancy (e) normalized injection profile (green) and non-resonant carrier profile (blue) (f) normalized output power as a function of time, Note presence of a strong dip on the centre of the near field, together with asymmetric field and carrier profiles.

carrier induced anti-guiding. One such injection profile is exemplified using the 130 μm case (see figure [3.14]).

3.5 Discussions

In the foregoing sections, the beam properties of injection profiled QD lasers were analyzed using rate equation approach. This model overlooked the possibility of lasing from excited dot states [31], and different relaxation timescale's for electrons and holes [53]. Nevertheless, the model qualitatively explain the unique carrier dynamics of the QD laser devices. Again, as explained above, the objective of this particular modelling is to examine the role of non-resonant charge carriers in the appearance of the characteristic dip at the near field intensity distribution of the QD laser. The above "result" section exemplifies more than once about the occurrence of the characteristic dip at the near field intensity.

The experimental results points out that for wide injection profiled devices a strong dip appears in the near field. In the numerical simulations, a similar dip also occurs when the injection profile width increases beyond 70 μm for high phase amplitude coupling when the resonant states are close to saturation. This dip gradually emerges as the injection is raised, similar to the one observed in experiment. From the simulation results, this dip can be ascribed to increased anti-guiding in the region of the dip, due to both narrowing and subsequent build-up of the non-resonant carrier profile. Moreover, spontaneous symmetry breaking was discovered in the simulation, whereby the position of the source of the transverse traveling waves in the near field shifts from the centre of the injection region.

To examine the sensitivity of the output features to variation in the parameter values, the relative contribution of non-resonant charge carriers to the overall anti-guiding factor was varied. When the contribution was brought down from 60% to 50%, no noted difference in the output beam properties were observed. However, on being reduced to 40% the characteristic dip in the near field decreased significantly and the occurrence of filamentary output increased. In addition, the threshold current is not constant (see Table [3.2]) and it depends on the linewidth enhancement factor similar to QW lasers [9].

In the future, more elaborate experiments and simulations are planned to

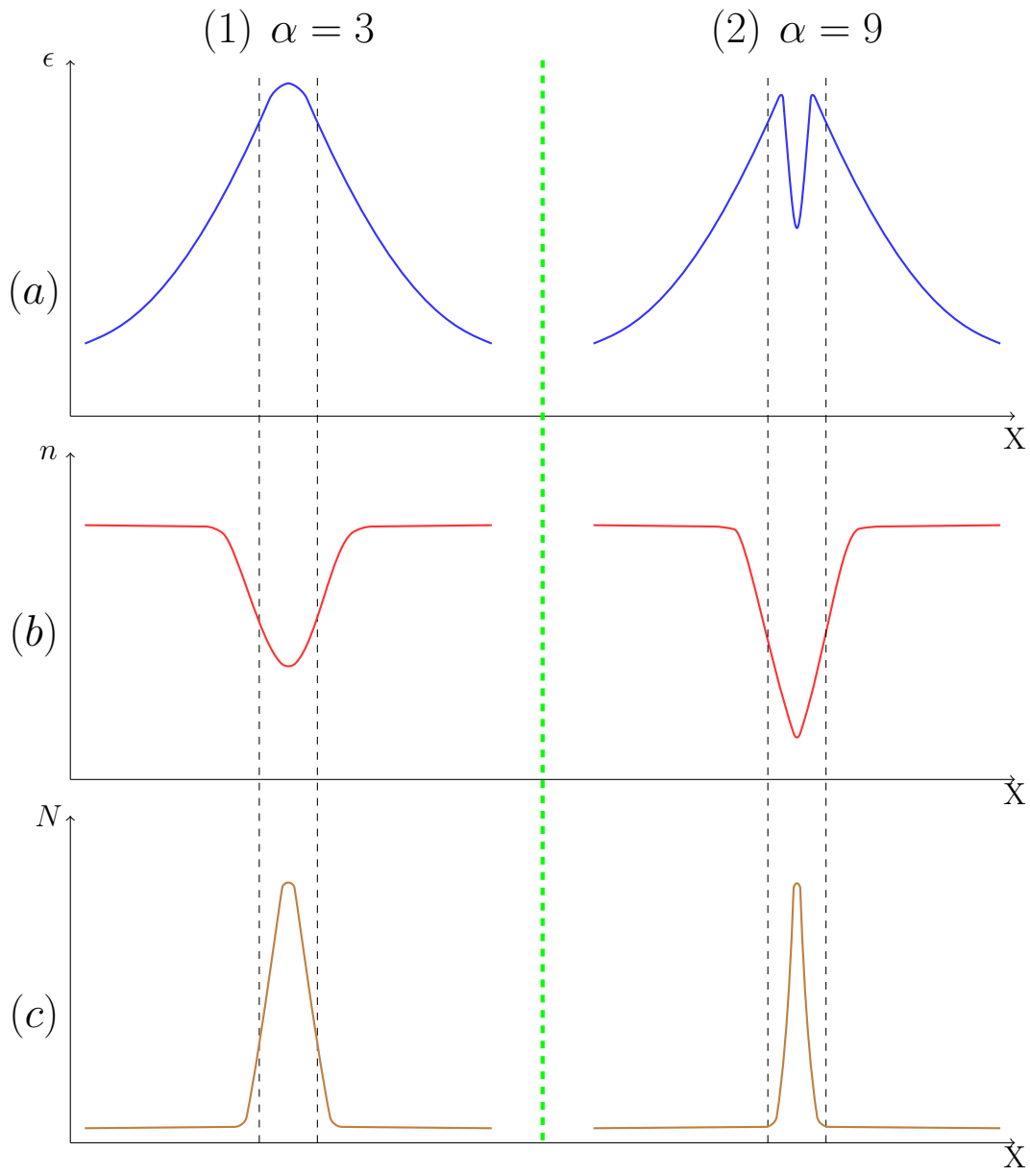

Figure 3.15: Schematic representation of characteristic dip formation in the near field intensity of the QD laser. "n" represents refractive index profile (red), "N" denotes to non-resonant carrier profile (brown), and "ϵ" refers to near field intensity (blue). The lowering of refractive index due to injected carriers creates an anti-guiding structure, which is common to gain guided lasers. In saturated QD laser case, the non-resonant charge carrier profile narrows substantially in comparison to the injected charge carrier profile. At high α factor, further narrowing of non-resonant charge carrier profile takes place. This effect triggers a further lowering of refractive index, and thus leading to a dip formation in the near field intensity.

further investigate unique effects to QDs such as the separate roles of excited dot and quantum well wetting layer states, and the different recombination times of electrons and holes due to the difference in effective mass [31][53].

3.5.1 Conclusions

The unique carrier dynamics of QD devices results in distinctive features when compared to QW devices. In QD SLs, a strong dip in the near field intensity can be attributed to increased localized anti-guiding due to the non-resonant carrier buildup when the resonant population is close to saturation. Moreover, the occurrence of symmetry breaking in the saturated dot case is due to shifting of transverse traveling wave source from the center to one of its side.

Chapter 4

Beam propagation approach

In this chapter, we employ an alternative modelling approach to further understand the structure of photon and carrier profiles inside a laser cavity, i.e. along the longitudinal and transverse dimensions and how they relates to the near field intensity distribution at high injection currents. Also, using this alternative method allows a comparison with the results obtained from the [1-D] rate equation approach in the previous chapter and a better fundamental understanding of the device properties.

4.1 Introduction

One of the main purpose of semiconductor laser modelling is to understand the device behaviour as well as to provide a feedback for device improvement. There are several rate equation models describing the dynamic properties of gain guided lasers and these models with a varying degree of approximation deal with transverse variations of the active region gain arising from the current spreading layer.

In the previous 1D modelling of QD laser (see chapter [3]), the transverse fluctuation of the active-region gain, arising due to injection current profile was discussed. However, the axial (i.e. along the longitudinal dimension) variation of both the transverse mode and the carrier density profiles inside the laser cavity were ignored (see figure [2.11]). While in axially uniform lasers the above assumption is

nearly sufficient for the realm of threshold. However, encase of the above-threshold regime, the stimulated recombination usually causes both the transverse mode and the carrier density profiles to vary along the longitudinal dimension [54]. In some special cases, the axial variation of a device parameter is intentionally introduced to increase the device performance [55]. In the current chapter, a beam-propagation (2-D) model that is capable of including both the axial and the transverse effects in the QD laser is examined.

4.2 Model

A forward-bias voltage across the double heterojunction injects the carriers (electrons and holes) into the active layer and changes the dielectric constant (both the real and imaginary parts). This affects the propagation of the optical mode along the axial direction which in turn affects the carrier distribution through stimulated recombination.

4.2.1 Paraxial wave equation

The optical field $E(r,t)$ inside the laser cavity satisfies Maxwell's wave equation.

$$\nabla^2 E - \frac{\epsilon(r)}{c^2}\frac{\partial^2 E}{\partial t^2} = 0 \tag{4.1}$$

Where c is the vacuum velocity of light and the complex dielectric constant $\epsilon(r)$ depends on the carrier density $N(r)$ inside the active layer. Generally, $E(r,t)$ is a superposition of many longitudinal, transverse, and lateral modes oscillating at different frequencies. For simplicity, a single mode at the optical frequency ω is taken into consideration as the lowest order even TE mode reaches threshold first. The contribution of spontaneous emission to the lasing mode has been overlooked because its affect on the static device characteristics is insignificant. The electric field propagating in the cavity can be written as:

$$E(r,t) \simeq \frac{1}{2}\widehat{x}\phi(y;x,z)\{E_f(x,z)\,exp[i(kz-\omega t)] + E_b(x,z)\,exp[-i(kz-\omega t)]\} \tag{4.2}$$

Where E_f and E_b corresponds to forward and backward travelling waves respectively, and k is the propagation constant. The field distribution $\phi(y;x,z)$, corresponding to the fundamental transverse mode guided by the double-heterostructure step depends weakly on x and z.

By substituting Eq. [4.2] in Eq. [4.1], multiply by $\phi^*(y)$ [complex conjugate of $\phi(y)$] and integrate along the lateral dimension y, we get a paraxial wave equation:

$$\pm 2ik\frac{\partial E_\mu}{\partial z} + \frac{\partial^2 E_\mu}{\partial x^2} + k_0^2\Delta\epsilon(x,z)E_\mu = 0 \tag{4.3}$$

Where + or − sign is chosen for μ equals f or b respectively,

Therefore, the equation for the propagating electric field in the forward direction is written as:

$$\frac{\partial E}{\partial Z} = \frac{i}{2K_z}\frac{\partial^2 E}{\partial x^2} + \frac{i}{2K_z}k_0^2\Delta\epsilon(x,z)E \tag{4.4}$$

Where $K_z = \eta K_0$ is the propagation constant, η is the effective refractive index, $k_0 = \frac{\omega}{c}$ and $\Delta\epsilon$ represents the active layer dielectric constant defined by the following equation:

$$\Delta\epsilon = \frac{\alpha_d\, g_0(2\rho-1)}{2v_g} + \frac{\alpha_{nr}\, g_0 N}{v_g} - i\frac{g_0(2\rho-1)}{2v_g} \tag{4.5}$$

where σ is the cross section of interaction of the carriers in a dot with the electric field, q is elementary charge, E is the complex amplitude of the electric field in the cavity normalized to the photon density $S = |E|^2$, γ_s is the photon decay rate in the cavity, g_0 the differential gain, and $D_e = \frac{c}{2k_0\eta^2}$ refers to the diffraction coefficient of light (where k_0 represents the wavenumber in the vacuum, c is the velocity of light and η is the effective refractive index). In the preceding equation, the terms on the L.H.S represent the variation of active layer dielectric

constant with respect to resonant carriers (α_d), non-resonant carriers (carriers in the wetting layer) (α_{nr}) and the differential gain term (g_0).

4.2.2 Steady-state carrier approach

In general, application of a perturbation to the inversion level of a laser (e.g. switching on) results in transient oscillations in the photon field before finally settling to a steady-state. In our beam propagation approach, for reasons of numerical efficiency, we will assume a very fast relaxation of carriers to their steady state and adiabatically eliminate the carrier rate equations, thereby losing the ability to accurately reproduce this transient. Thus, as outlined in the introduction, we are effectively changing our system from a Class B laser system to a Class A system which may have consequences on the validity range of our predictions. Nonetheless, if a stable solution exists in the previous model, we should be able to reproduce it and examine its impact on the internal fields of the laser.

The steady state carrier model is based on the assumption that the laser is operated in the above-threshold regime and the steady state carrier rate equations are obtained by equating the equations [3.1] and [3.2] to zero i.e. $\frac{\partial \rho}{\partial t} = 0$ and $\frac{\partial N}{\partial t} = 0$. Therefore the equations for ρ and N are:

$$N = \frac{J(x)}{q\left[\gamma_n + 2C(1-\rho)\right]} \tag{4.6}$$

$$\rho = \frac{CN + v_g \sigma |E|^2}{\left(\gamma_d + CN + 2v_g \sigma |E|^2\right)} \tag{4.7}$$

Where γ_n , γ_d are the non-radiative decay rates for carriers in the WL and dot respectively, C is the capture rate from wetting layer into an empty dot, and $J(x)$ is the spatially varying injection current per dot (a Lorentzian shape is used throughout).

4.2.2.1 Miscellaneous

- In our model, we assumed only the unidirectional (i.e. forward direction) waves in the resonator cavity, these forward propagating waves on reflection

Table 4.1: Parameters used in the model corresponding to a 60% contribution from non-resonant carriers to α_{th}

$\gamma_n = \gamma_d = 10^{-3}\ (ps)^{-1}$		
$\gamma_s = 0.3\ (ps)^{-1}$		
$v_g = 167 * 10^6\ \frac{m}{s}$		
$C = 10^{-1}\ (ps)^{-1}$		
$\lambda = 1310nm$		
$\eta = 3.5$		
$L = 0.5\ mm(i.e.\ 500\ \mu m)$		
$R_m = 0.75$		
For $\rho_{th} = 0.9$	$g_0 = 22.5\ (cm)^{-1}$	$\sigma = 1.88 * 10^{-7}\ (\mu m)^2$
$\alpha_{th} = 3$	$\alpha_d = 1.2$	$\alpha_{nr} = 0.45$
For $\rho_{th} = 0.6$	$g_0 = 90\ (cm)^{-1}$	$\sigma = 7.5 * 10^{-7}\ (\mu m)^2$
$\alpha_{th} = 1.5$	$\alpha_d = 0.6$	$\alpha_{nr} = 14.4$

Table 4.2: J_{th} value for different α values.

For $\alpha = 0$	$= 3$	$= 6$	$= 9$
$J_{th} = 2.45 * 10^{-10}\left(\frac{coulombs}{sec}\right)$	$= 1.9 * 10^{-10}\left(\frac{coulombs}{sec}\right)$	$= 1.6 * 10^{-10}\left(\frac{coulombs}{sec}\right)$	$= 1.5 * 10^{-10}\left(\frac{coulombs}{sec}\right)$

near the cavity mirror changes their direction into the backward. Again, this backward travelling waves on reflection at the other cavity mirror change there direction of propagation to forward. This never-ending cycle of propagation of travelling waves builds up enough light intensity in the cavity, which in turn leads to lasing process.

- The boundary conditions at the facets is given by the following equations:

$$E_b\left(x, L\right) = \sqrt{R_m} E_f\left(x, L\right) \tag{4.8}$$

$$E_f\left(x, 0\right) = \sqrt{R_m} E_b\left(x, 0\right) \tag{4.9}$$

Where "L" is the length of the cavity, "E_f'' *and* "E_b" points the forward and the backward travelling electromagnetic waves with electric field "E", "R_m" represents facet reflectivity, "x" denotes the coordinate in the transverse direction and the beam propagation is from z = 0 to z = L (see figure [2.11]).

4.3 Results

4.3.1 Unsaturated ($\rho_{th} = 0.6$) case

The narrow (35 μm) and the wider (35 μm) injection profile for the unsaturated case yielded a stable output up to $\sim 1.5 J_{th}$, thereafter the onset of unstable dynamics occurs. In comparison to the 1D simulation case (see chapter [3]), the stability range is considerably less, most likely due to the steady state approximation. The figures [4.1] and [4.2] exemplifies the output features of the unsaturated case. The near field intensity follows the pump profile and consists of two spatially separated counter-propagating traveling waves resulting in distinct, off-axis emission in the far field, stabilized by a carrier induced anti-guide, which is very similar to the previous studies on 1D simulation case (see chapter [3]).

Next, at higher ($\alpha = 4.5$) linewidth enhancement factor the simulation fails to show any stable output features, which is in contrast to the 1D simulation results discussed in chapter [3].

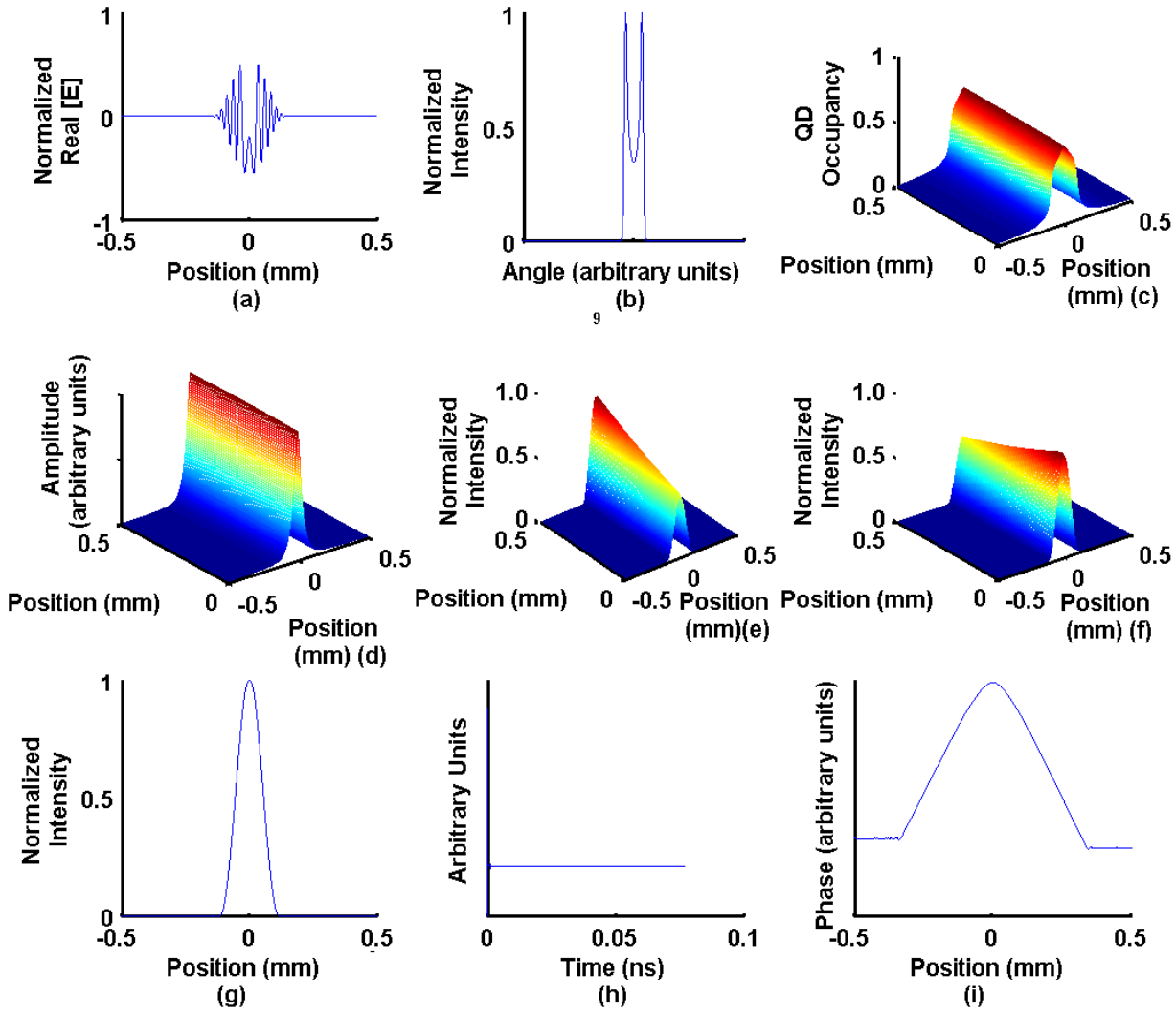

Figure 4.1: Simulated beam properties of QD laser using steady state beam propagation carrier approach for a 35 μm wide Lorentzian injection profile in the saturated regime ($\rho_{ss} = 0.6$) at $1.5J_{th}$ and $\alpha = 1.5$. (a) Instantaneous near field electric field (b) Instantaneous far field intensities (c) QD occupancy (d) non-resonant carrier profile (e) forward propagating intensity profile (f) backward propagating intensity profile (g) near field intensities (h) non-resonant carrier turn-on transient (i) Phase of near field .

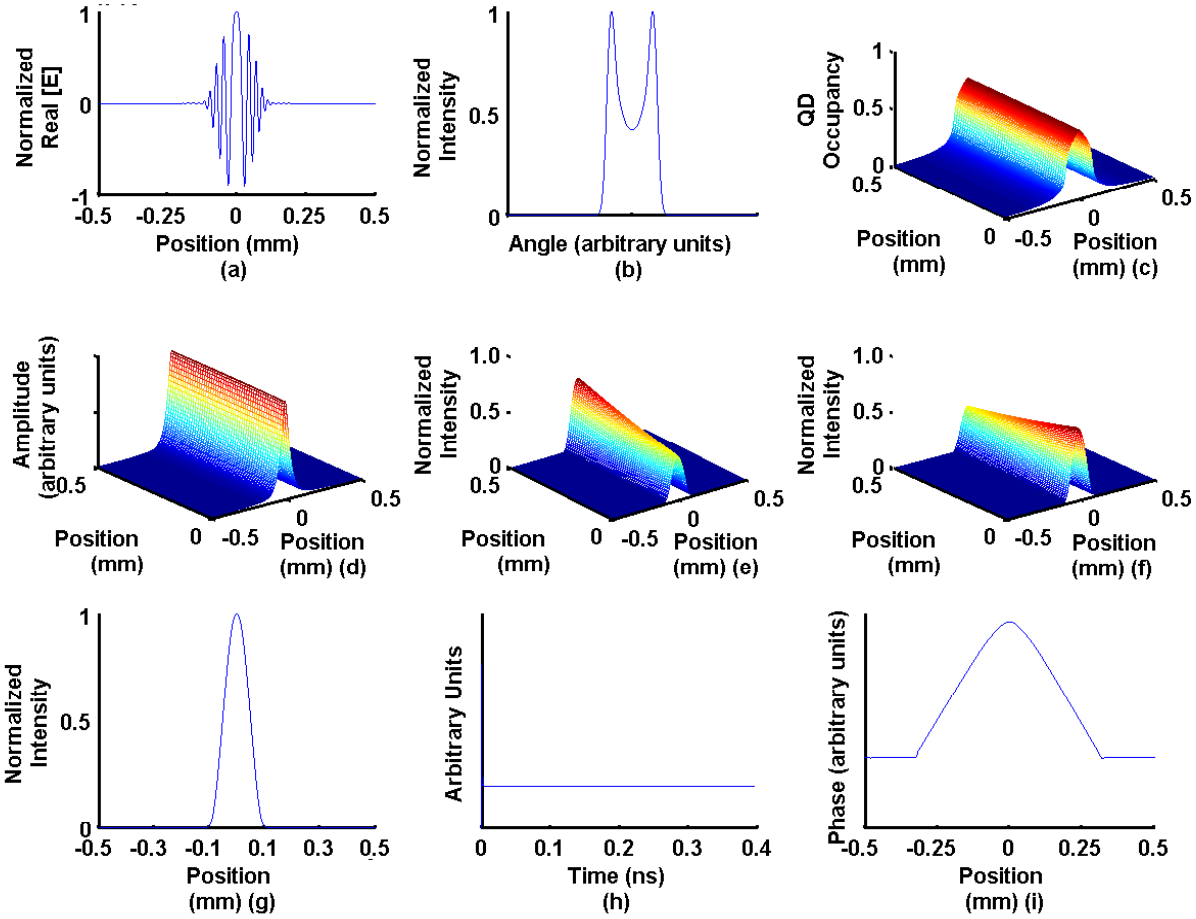

Figure 4.2: Simulated beam properties of QD laser using steady state beam propagation carrier approach for a 70 μm wide Lorentzian injection profile in the saturated regime ($\rho_{ss} = 0.6$) at $1.5J_{th}$ and $\alpha = 1.5$. (a) Instantaneous near field electric field (b) Instantaneous far field intensities (c) QD occupancy (d) non-resonant carrier profile (e) forward propagating intensity profile (f) backward propagating intensity profile (g) near field intensities (h) non-resonant carrier turn-on transient (i) Phase of near field .

4.3.2 Saturated ($\rho_{th} = 0.9$) case

The next step in the simulation was to study the beam characteristics for the saturated case. For the parameters outlined in table [4.1], and [4.2], and for an injection width of 35 μm the behaviour was very similar to that outlined for the narrower injection profiles for saturated case in 1-D rate equation approach (see chapter [3]). An example of this for the narrow 35 μm injection profile is exemplified in figure [4.3]. Here, one marked distinctive feature that we observed was the bulging of the non-resonant carrier profile along the longitudinal dimension. The stable output features can be viewed up to $\sim 7\, J_{th}$, as the onset of filamentary dynamics makes simulation unviable. For higher ($\alpha = 9$) linewidth enhancement factor, the instability level came down to $\sim 1.5\, J_{th}$.

The simulation for the wider $70\mu m$ injection profile yeilded a small dip at the near field intensity at $\alpha = 9$ (see figure [4.4]). The behaviour persists up to $\sim 6\, J_{th}$. The bulging of non-resonant carrier profile along the longitudinal dimension was seen here too. When the injection is further increased to 7 (beyond instability level), the turn-on transient for the non-resonant carrier showed irregular spikes instead of a clamped one and the near field profile showed a self-pulsing behaviour. In order to resolve this effect, we went back to study the dynamics of 1-D steady state carrier rate equations (using equations [3.3], [4.6] & [4.7]). We observed a small dip in the near field intensity for narrow 35 μm injection profile (see figure [4.7]) at $\alpha = 9$ and $\sim 4\, J_{th}$. When the injection is further increased to $\sim 4.5\, J_{th}$, we observed a similar pattern, however, the output power showed a sinusoidal type pattern instead of a clamped one and the near field profile showed a self-pulsing behaviour.

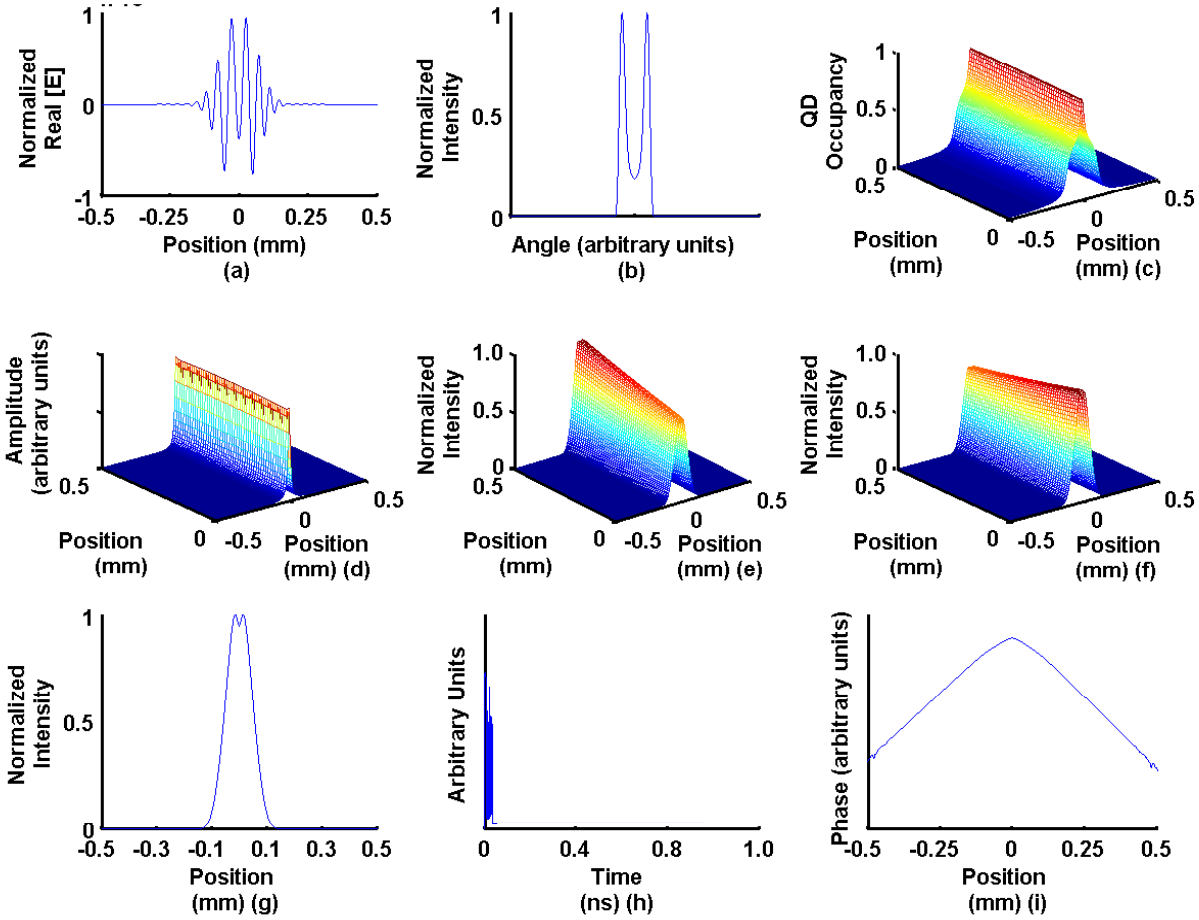

Figure 4.3: Simulated beam properties of QD laser using steady state carrier beam propagation approach for a 35 μm wide Lorentzian injection profile in the saturated regime ($\rho_{ss} = 0.9$) at $5J_{th}$ and $\alpha = 3$. (a) Instantaneous near field electric field (b) Instantaneous far field intensities (c) QD occupancy (d) non-resonant carrier profile (e) forward propagating intensity profile (f) backward propagating intensity profile (g) near field intensities (h) non-resonant carrier turn-on transient (i) Phase of near field .

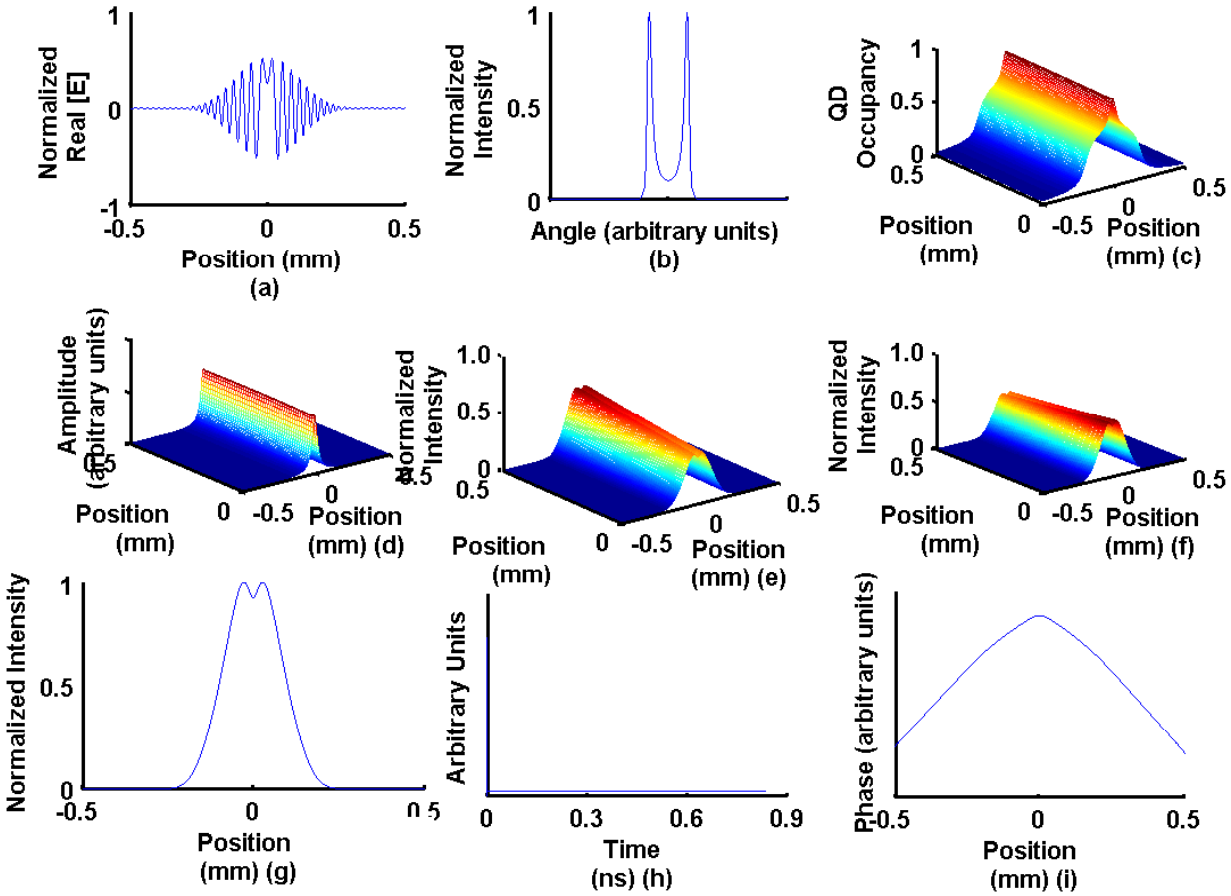

Figure 4.4: Simulated beam properties of QD laser using steady state carrier beam propagation approach for a 70 μm wide Lorentzian injection profile in the saturated regime ($\rho_{ss} = 0.9$) at $5.5J_{th}$ and $\alpha = 9$. (a) Instantaneous near field electric field (b) Instantaneous far field intensities (c) QD occupancy (d) non-resonant carrier profile (e) forward propagating intensity profile (f) backward propagating intensity profile (g) near field intensities (h) non-resonant carrier turn-on transient (i) Phase of near field .

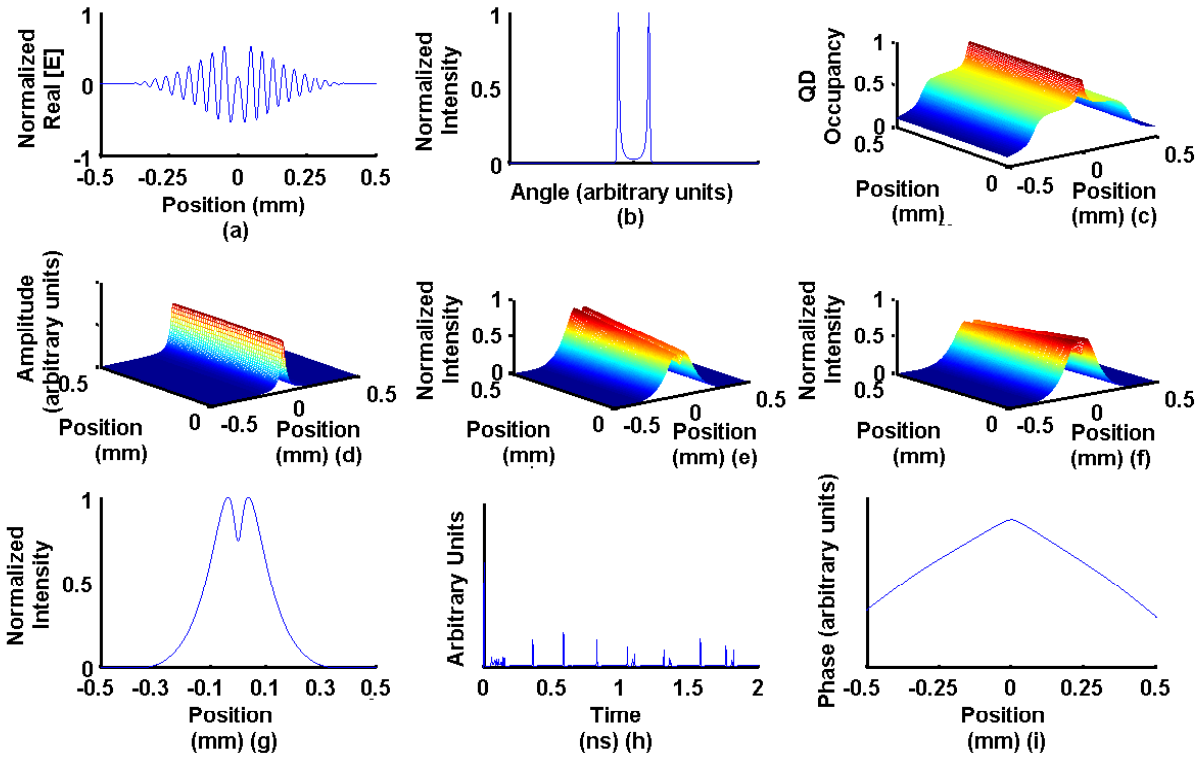

Figure 4.5: Simulated beam properties of QD laser using steady state carrier beam propagation approach for a 70 μm wide Lorentzian injection profile in the saturated regime ($\rho_{ss} = 0.9$) at $7J_{th}$ and $\alpha = 9$. (a) Instantaneous near field electric field (b) Instantaneous far field intensities (c) QD occupancy (d) non-resonant carrier profile (e) forward propagating intensity profile (f) backward propagating intensity profile (g) near field intensities (h) non-resonant carrier turn-on transient (i) Phase of near field .

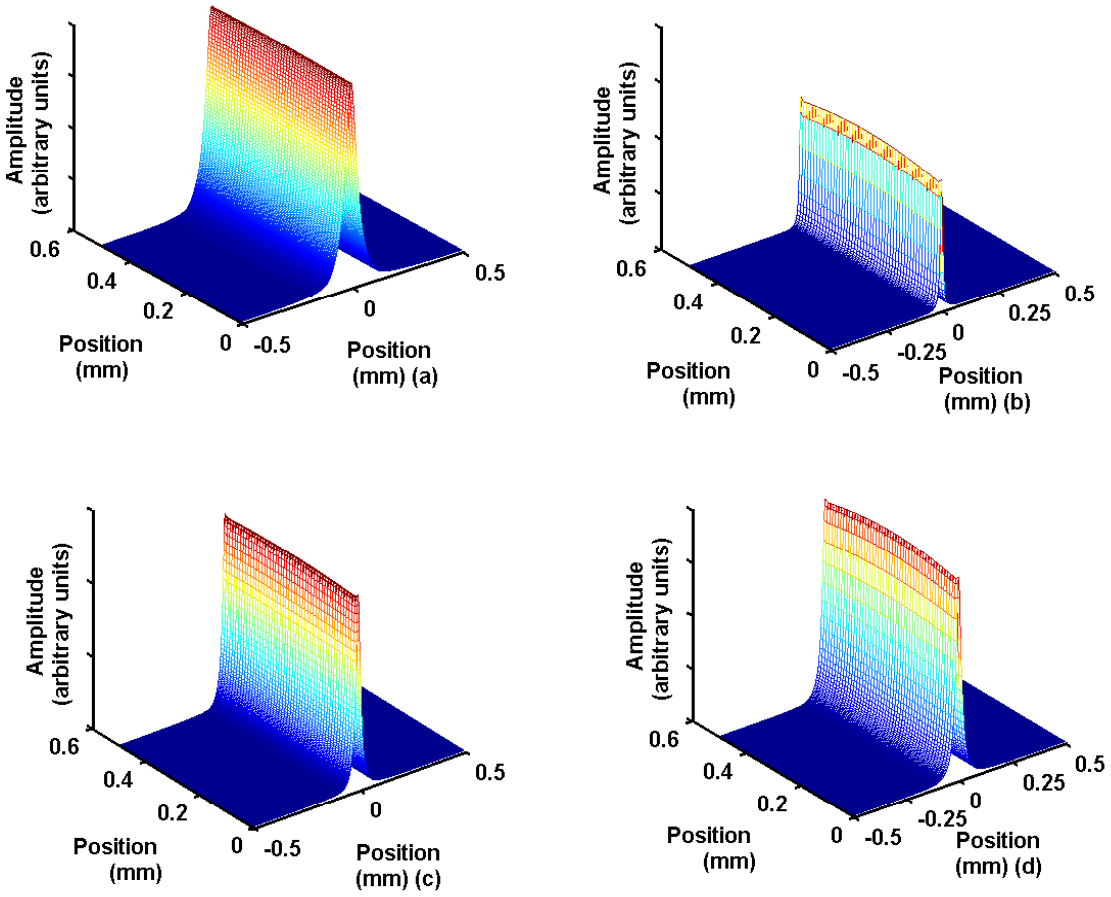

Figure 4.6: Non-resonant carrier profile compared for unsaturated and saturated regimes. (a) unsaturated regime at $\alpha = 1.5$ Lorentzian injection width $= 35\,\mu m$ and $1.5J_{th}$ (b) saturated regime at $\alpha = 3$ Lorentzian injection width $= 35\,\mu m$ and $1.5J_{th}$ (c) unsaturated regime at $\alpha = 1.5$ Lorentzian injection width $= 50\,\mu m$ and $1.5J_{th}$ (d) saturated regime at $\alpha = 3$ Lorentzian injection width $= 50\,\mu m$ and $4J_{th}$ Note the significant bulging of the non-resonant carrier profile near cavity centre in the saturated case.

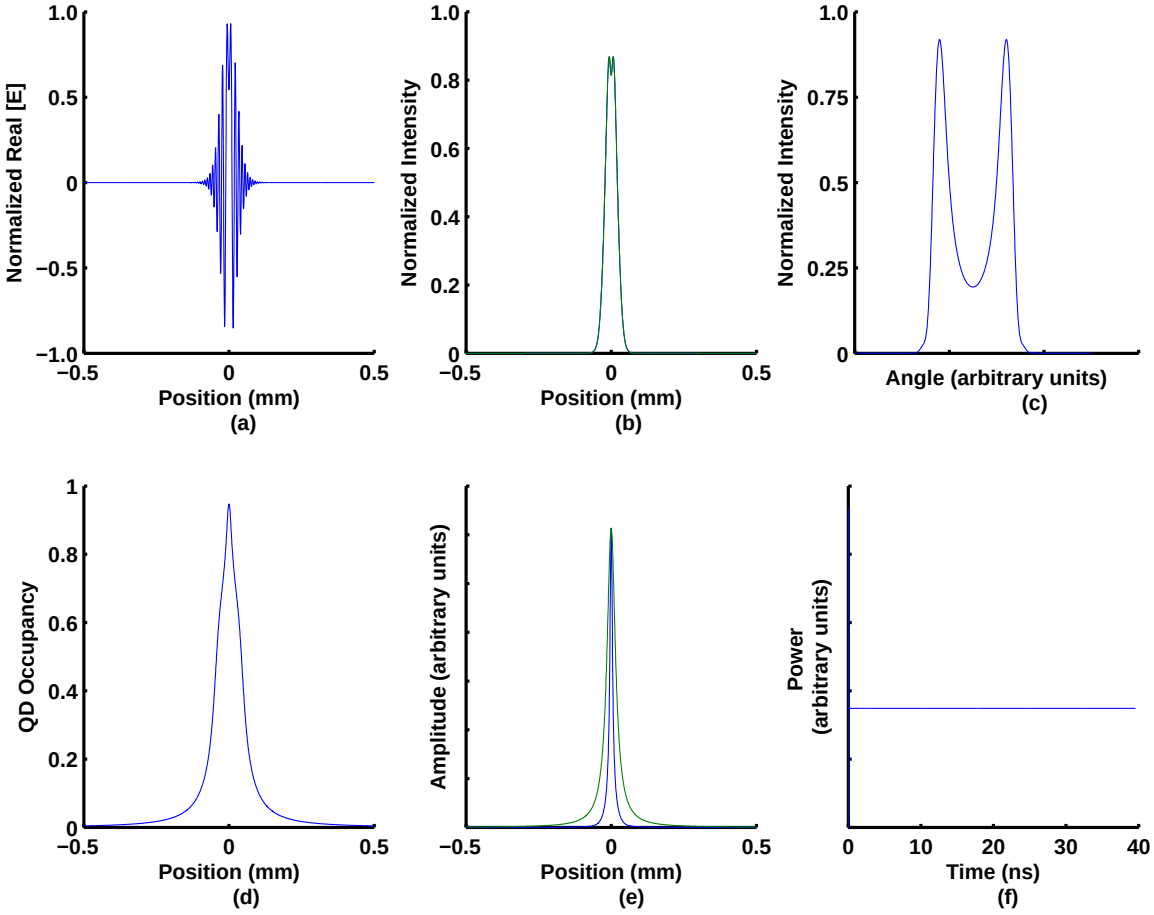

Figure 4.7: Simulated beam properties of QD laser using steady state carrier approach for a 35 μm wide Lorentzian injection profile in the saturated regime ($\rho_{ss} = 0.9$) at $4J_{th}$ and $\alpha = 9$. (a) Instantaneous near field electric field (b) instantaneous (blue) and time averaged (green) near field intensities (c) instantaneous far field intensities (d) QD occupancy (e) normalized injection profile (green) and non-resonant carrier profile (blue) (f) normalized output power as a function of time.

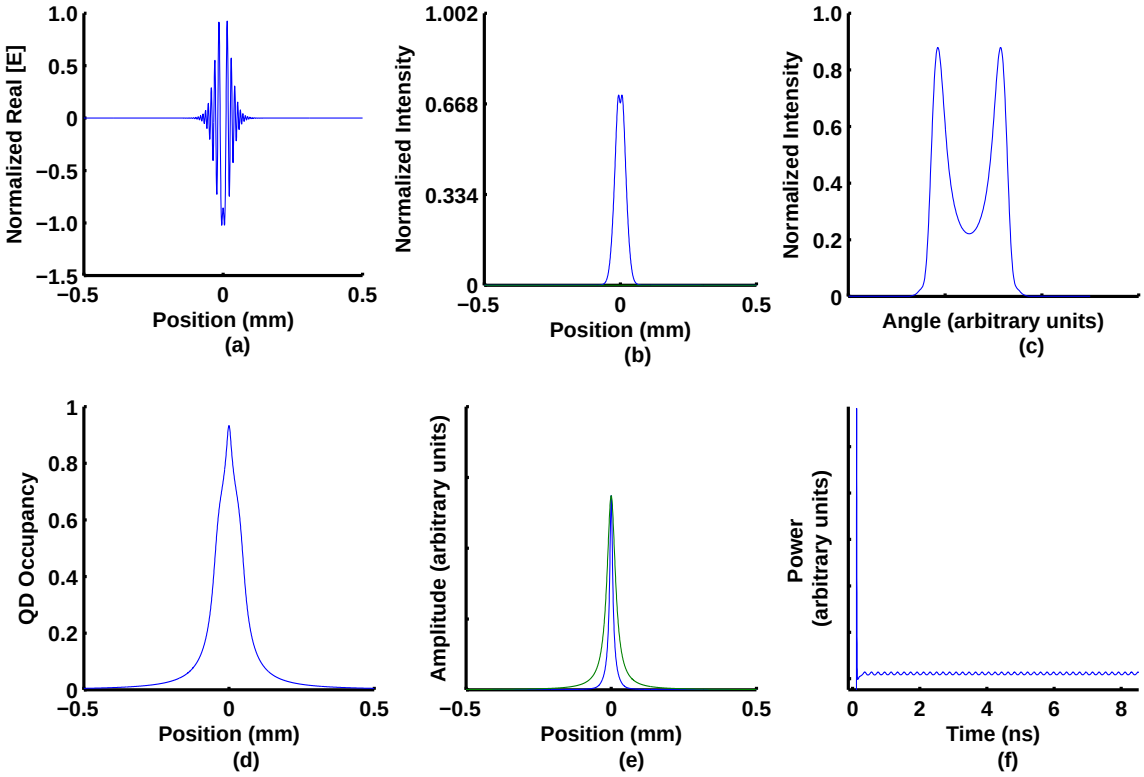

Figure 4.8: Simulated beam properties of QD laser using steady state carrier approach for a 35 μm wide Lorentzian injection profile in the saturated regime ($\rho_{ss} = 0.9$) at $4.5J_{th}$ and $\alpha = 9$. (a) Instantaneous near field electric field (b) instantaneous (blue) and time averaged (green) near field intensities (c) instantaneous far field intensities (d) QD occupancy (e) normalized injection profile (green) and non-resonant carrier profile (blue) (f) normalized output power as a function of time.

4.4 Discussions

In the previous sections, the beam properties of injection profiled QD SL were analyzed through beam propagation approach. The steady state carrier populations for saturable resonant QD states and non-resonant states was presented. This model neglects the dynamic change of charge carrier population. In spite of being the least dynamic model, it qualitatively provides insights on observed phenomena unique to QD devices, also supports the results that were observed in 1-D rate equation approach (from chapter [3]).

Experimentally, in wide injection profiled devices a strong dip appears in the near field. In the 2-D beam propagation approach, a similar dip also occurs when the injection profile width increased beyond $70\,\mu m$ for high phase amplitude coupling when the resonant states were close to saturation. This dip emerges gradually as the injection increases, a similar trend also seen in the experiment. From the numerical simulations, this dip can be attributed to increased anti-guiding in the region of the dip, due to narrowing of the non-resonant carrier profile and subsequent buildup of carriers in the wetting layer. In addition, the bulging of the non-resonant carrier profile along the longitudinal dimension was observed for the saturated dot case (see figure [4.6]).

This model does reproduce the "characteristic dip" at the near-field intensity but it is not as deep as the one observed from rate equation (1-D) approach due to the lack of carrier dynamics, as the model represents a Class A type laser instead of Class B type laser.

The self-pulsing behaviour does not occur for 1-D rate equation approach. Therefore it appearance in the steady-state carrier beam propagation approach and steady state carrier (1-D) rate equation approach is due to steady-state carrier assumption.

One solution is to construct a dynamic carrier beam propagation approach (representing a Class B type laser) and analyze the results.

4.4.1 Conclusions

A dip in the near field intensity distribution across the device can be implicated to increased localized anti-guiding due to non-resonant carrier buildup when the resonant population is close to saturation. In addition, a higher build up of non-resonant charge carriers occurs at the center of the device than at the rear ends. These above features highlights the unique carrier dynamics of QD laser device.

Chapter 5

QD laser array

This chapter provides the simulation analysis of phase-locking between two transversely coupled injection profiled QD lasers.

5.1 Introduction

Some applications require coherent output power levels of $> 100\,mW$ e.g. free-space communications, blue-light generation via frequency doubling, parallel optical-signal processing, high resolution laser printing and end-pumping solid state lasers. Generally, from a narrow stripe ($3 - 4\,\mu m\ wide$) edge-emitting lasers, one can expect a single mode output at just above threshold current with output power at $\sim 100\,mW$. If high output powers are to be obtained from these devices then the stripe width must be increased. This enables the induced injection current to access large transverse active region. However, this solution comes at the cost of reduced beam quality because the laser oscillates with multiple number of transverse modes. Hence, the correlation between the dimension of injection stripe and the output beam quality severely hinders the practical usage of this device for high power applications. This reduction in beam quality with stripe width has led to the development of Phase-locked arrays of semiconductor lasers, which have been studied extensively over the last 30 years.

The basic principles behind the phase-locking among a linear array of ideal emitters (diode lasers) can be best understood through electromagnetic (EM) the-

ory. Consider, for an example, a series of equally spaced emitters that can generate EM radiation with same frequencies (wavelengths) but with random phases $\varphi_n(x,t)$ [The phase $\varphi_n(x,t)$ is a function of the spatial coordinate x and time t and n represents number of emitters]. The uncorrelated random phases result in a light beam which is principally incoherent. Such an array of emitters would generate a random interference pattern that fluctuates both in space and time and has no practical use. It would be much more useful to have an array of coherent emitters, where a definite phase relationship exists between individual light beams and a fixed interference pattern results.

In comparison with other types of high-power coherent sources (master oscillator power amplifier, unstable resonators), phase-locked arrays are more desirable because of the less complicated optical setup and cheaper production cost. In a diode laser array, several narrow stripe lasers can be coupled to produce a very high power output of $> 100\,mW$ (see figure [5.3]).

The four basic types of phase-locked arrays are: leaky-wave coupled, evanescent-wave coupled, Y-junction coupled and diffraction coupled (see figure [5.1]). These devices operate via coupling of adjacent transverse modes. The coupling can be either leaky-wave type or evanescent-wave type. If the lasing modes have the major field-intensity peaks in the low-index array regions then leaky-wave coupling occurs but if lasing modes with high intensity peaks reside in the high-index array regions then evanescent-wave type coupling occurs. By nature gain-guided array laser will have leaky-wave type coupling, whereas the ridge-waveguide array laser will have evanescent-wave type coupling.

The development of Y-junction coupled and diffraction coupled devices occurred due to the complicated nature of evanescent-type coupling, where it is very difficult to achieve the in-phase mode (i.e., single central lobe) [60]. When it comes to the functioning, the Y-junction-coupled devices operate via wave interference and the diffraction coupled devices work through wave diffraction.

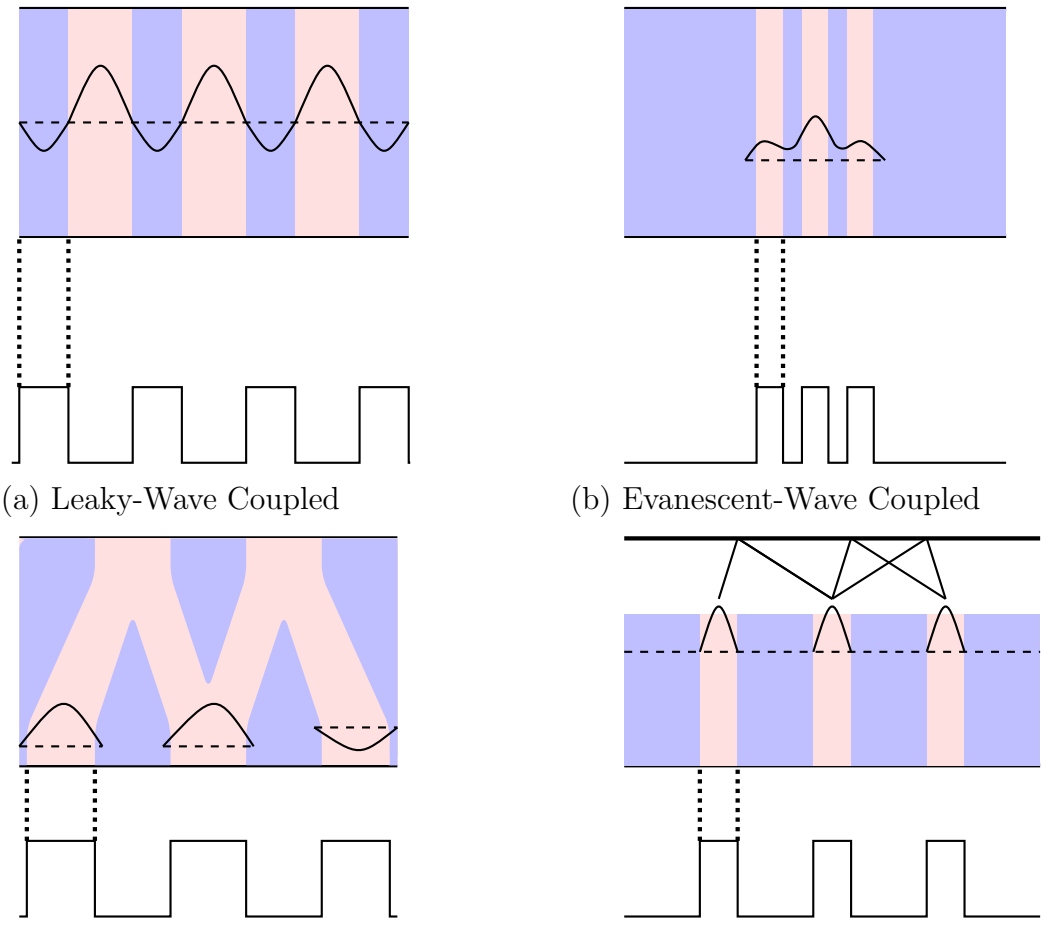

(a) Leaky-Wave Coupled

(b) Evanescent-Wave Coupled

(c) Y-Junction Coupled

(b) Diffraction Coupled

Figure 5.1: Schematic illustration of basic types of phase-locked linear arrays of diode lasers. Leaky-Wave Coupled: Low index region (Light Red), High Index region (Light Blue). For Evanescent-Wave Coupled, (c) Y-Junction Coupled & (d) Diffraction Coupled: Low index region (Light Blue), High Index region (Light Blue). The bottom traces correspond to refractive-index profiles [60].

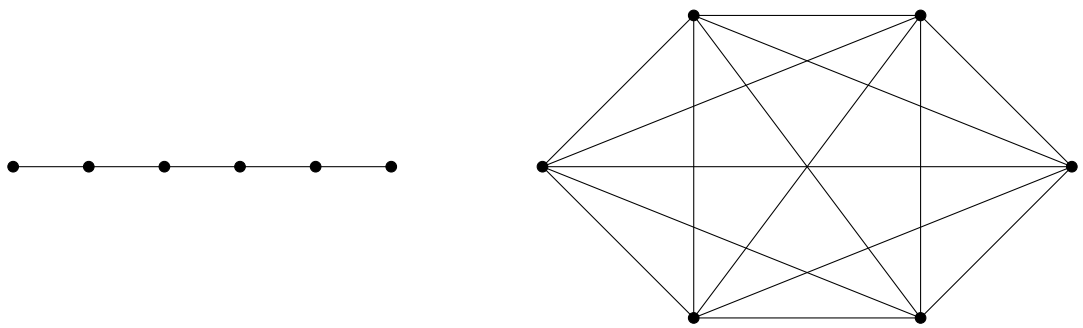

(a) (b)

Figure 5.2: Types of overall inter-element coupling in phase-locked arrays: (a) series coupling (nearest-neighbor coupling) (b) parallel coupling.

5.1.1 Coupling mechanism

The inter-element in a phase-locked diode laser array can couple light via either in the series or through the parallel way. The comparison in terms of advantages between series and parallel coupling (see figure [5.2]) is lopsided because the balance shifts in favor of the parallel one. In series coupling, the intermodal discrimination and the overall coherence are generally poor. While in case of parallel coupling, the equally strong coupling between each element with others gives rise to better intermodal discrimination. Moreover, parallel-coupled systems have uniform near-field intensity profiles, and are resistant to the onset of high order mode oscillation at high injection levels.

In our simulation, we used broad-area array laser having a leaky-wave type coupling (by nature) and a series inter-element coupling [by fabrication] (see figures [5.3], [5.1] & [5.2]).

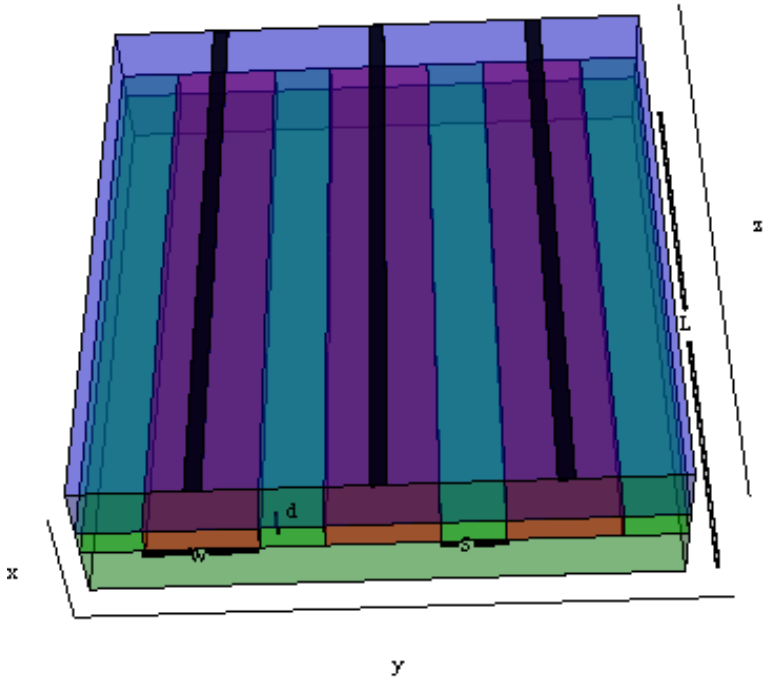

Figure 5.3: Schematic representation of the BA laser array (three coupled emitters) with the coordinate system (x,y,z). The laser cavity is in the axial (or longitudinal) direction [z]. [x] represents lateral or vertical direction, [y] denotes transverse direction, Contact area (black), active region (red), substrate (light green) and top layer (light blue). The active region below the contact area has a axial length (L), transverse width (W), vertical height (d) and spacing between the coupled emitters (S). A BA laser array, by its nature is a leaky-wave-coupled device.

5.2 Previous work

A theoretical study of two large aperture injection current profiled edge-emitting lasers, which are transversely coupled through respective gain profiles was first studied by E. O'Neill et al [33]. Similar to our injection profiling approach, an additional current spreading layer under the positive electrode of the device was used to achieve a Lorentzian injection profile along the transverse dimension.

In this study, a numerical model based on the standard Maxwell-Bloch equations was analyzed, where parameters point to a class B type laser. Moreover, an additional term representing the effects of linewidth enhancement factor was used [33]. The results from the analysis of two transversely coupled large aperture semiconductor lasers through Maxwell-Bloch rate equations are as follows:

At very small the lobe separation (typically $< 250\,\mu m$), the electric fields interact strongly, and the emitters can no longer be treated as independent but rather as a single and continuous element. Moreover, a very high pump level between the lobes compared to the outside edges results in an unstable output, which varies both in space and time (regime 1 in figure [5.5]). An initial increase in the lobe separation ($> 250\mu m$ but $< 300\mu m$) stabilizes the near-field intensity and thereafter further increase in the separation leads to regime 2, where the intensity becomes stable but with a periodic drifting phase relationship between the two transversely coupled emitters. The drifting phase is usually sinusiodal-like but sometimes can be strange.

Still further increase in the lobe separation leads to a stable phase locked output, which is identified as regime 3 in figure [5.5]. Here, the phase difference between the lobes tends towards to zero. A typical example of the output profile is shown in figure [5.4], where a stable near field intensity follows closely with the injection profile. As the separation is increased further, the regime 3 changes to regime 4, where the electric fields have negligible interaction between each other and the emitters act as separate entities, resulting in a stable output with unlocked phase (see figure [5.5]).

In addition, increasing the injection level, as can be seen in Fig . 5.5, forces the boundaries of the different regimes to larger lobe separations.

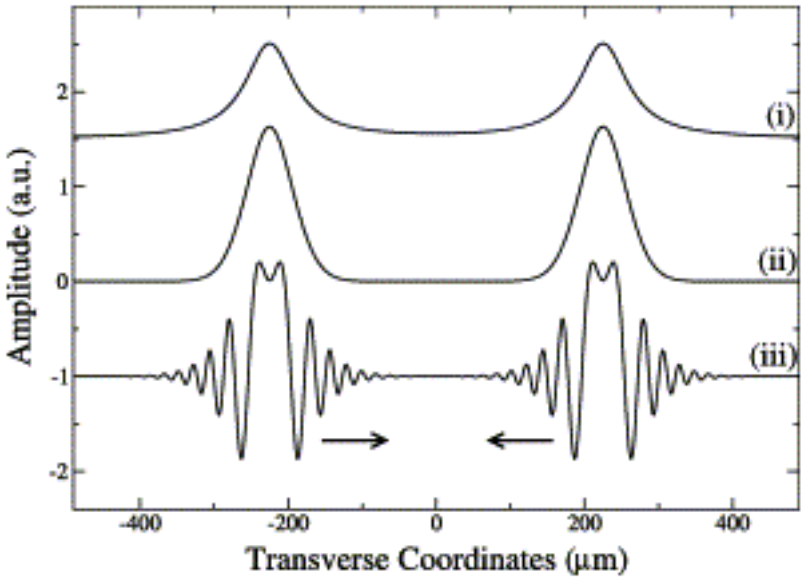

Figure 5.4: Schematic representation of output profile from a pair of injection current profiled edge-emitting lasers locked in phase showing (i) the pump profile, (ii) the near-field intensity and (iii) the real part of the electric field. The pump level was 3.0 and the lobe separation was 450 μm [25].

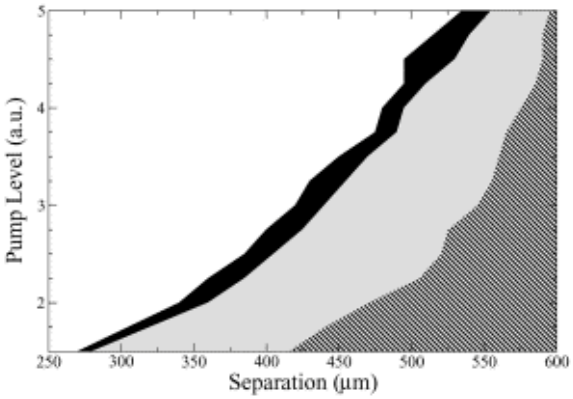

Figure 5.5: Schematic representation of stability and locking analysis of the coupled QW lasers in relation to pump level and lobe separation. Regime 1, unstable output (white); 2, stable output with drifting phase (black); 3, stable phase locked output(grey); 4, stable output with unlocked phase(stripped) [25].

If the injection level is maintained at a constant value and the pump profile is symmetric then the two transverse travelling waves will have the same k-vector because they produce the same k-vector (see figure [5.4]). Therefore, the lobe separation will now determine how the waves will interfere. As expected for an anti-guided structure, changing the lobe separation leads to periodically in - and out-of-phase locking between the two transversely coupled emitters. This coupling scheme is similar to the leaky-wave-coupled devices investigated by Botez [93].

5.3 Modelling

Previously, we have demonstrated the stable output features of injection profiled QD laser without filamentation. Where an Lorentzian-like injection profile generates an antiguide by lowering the refractive index of the gain medium. This carrier-induced antiguide confines the transverse travelling waves leading to a stable single-lobed near-field and double-lobed far-field. At high linewidth enhancement factor ($\alpha = 9$), a strong dip appears at the center of the near field intensity.

In this study, we examined the possibility of coupling two injection profiled QD lasers, similar to earlier work on transversely coupled semiconductor lasers (see section [5.2]) . We analyzed the spatial properties using rate equation approach and beam propagation approach (see chapters [3] & [4]) and the parameter values used in the two approaches are same as the one mentioned in the table [3.1] & [4.1]. The only difference is that the pump profile is double lobed Lorentzian (see figure [5.6]) instead of a single one. To examine the phase-locking between coupled QD emitters, we varied the lobe separation from $250\mu m$ to $1200\mu m$ and the injection pump level from $1\,J_{th}$ to $5\,J_{th}$. However, the instability threshold is $12\,J_{th}$. Similar to the single QD laser, the injected Lorentzian carrier profile affects the real part of the refractive index, where the peak of the carrier profile lowers the index region leading to an induced antiguide (see figure [5.6]). The coupling between the two travelling waves in the adjacent emitters is a leaky-wave type as the lasing modes with high intensity peaks are in the low index, and the low intensity peaks are in

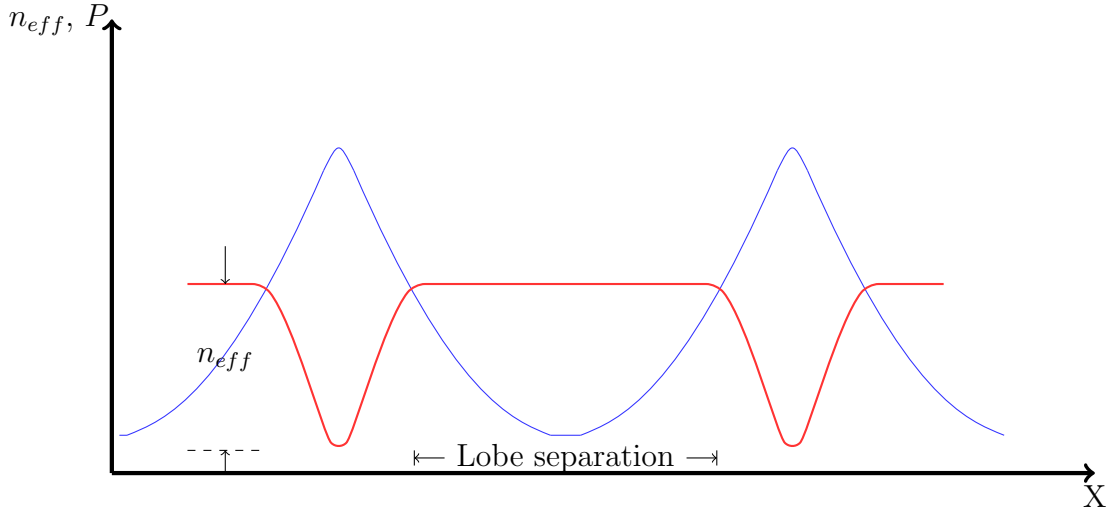

Figure 5.6: Schematic representation of the transverse optical confinement in a two QD BA lasers transversely coupled through their gain profiles. "P" represents dual lobed pump profile (arbitrary units) [blue], and "n_{eff}" represents lowering of refractive index due to injected Lorentzian charge carrier profile. This lowering of refractive index (antiguide) [red] acts as a dielectric transverse waveguide for the optical mode with intensity "ϵ". "X" refers to transverse dimension.

the high index array regions (see figure [5.6]).

5.4 Results

5.4.1 Results from rate equation approach

5.4.1.1 Saturated regime

The 1-D rate equation analysis of two transversely coupled injection profiled QD lasers was analyzed through gain profiling. Results indicate that the classification of the output into distinct phase regimes was more difficult than in the QW case. In particular, the phase relationship between the coupled emitters took a large time scale to evolve to a steady state (typical run time of $\sim 3Hours$). Nevertheless, a wider range of stable output features for $\geq 1200\mu m$ lobe separation was observed.

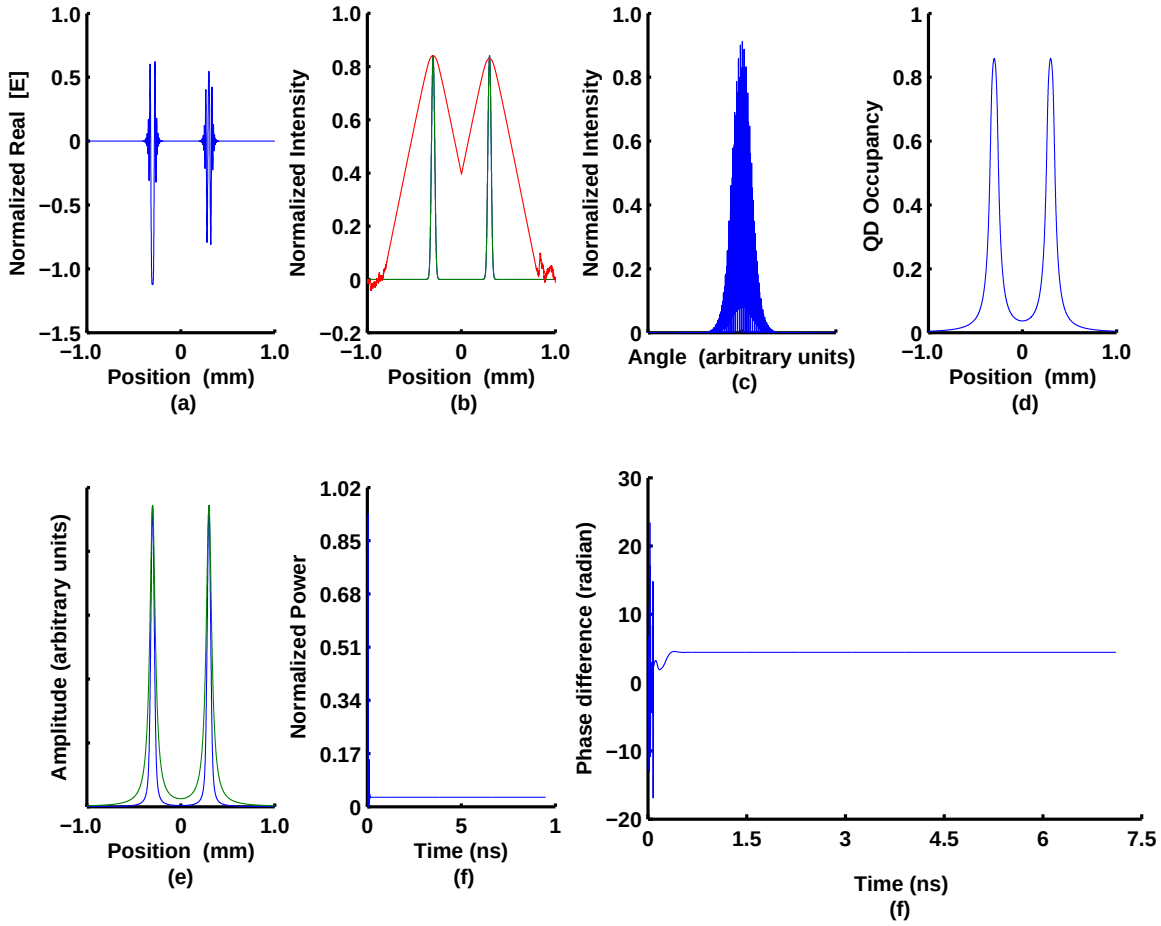

Figure 5.7: Simulated beam properties of QD laser array using rate equation approach for a 70 μm wide Lorentzian injection profile in the saturated regime ($\rho_{ss} = 0.9$) at 1.5 J_{th}, Lobe separation = 600μm and $\alpha = 9$. (a) Instantaneous near field electric field (b) instantaneous (blue) and time averaged (green) near field intensities, Phase (red) of near field (c) instantaneous far field intensities (d) QD occupancy (e) normalized injection profile (green) and non-resonant carrier profile (blue) (f) normalized output power as a function of time (g)Phase difference between the two counter-propagating traveling waves as a function of time.

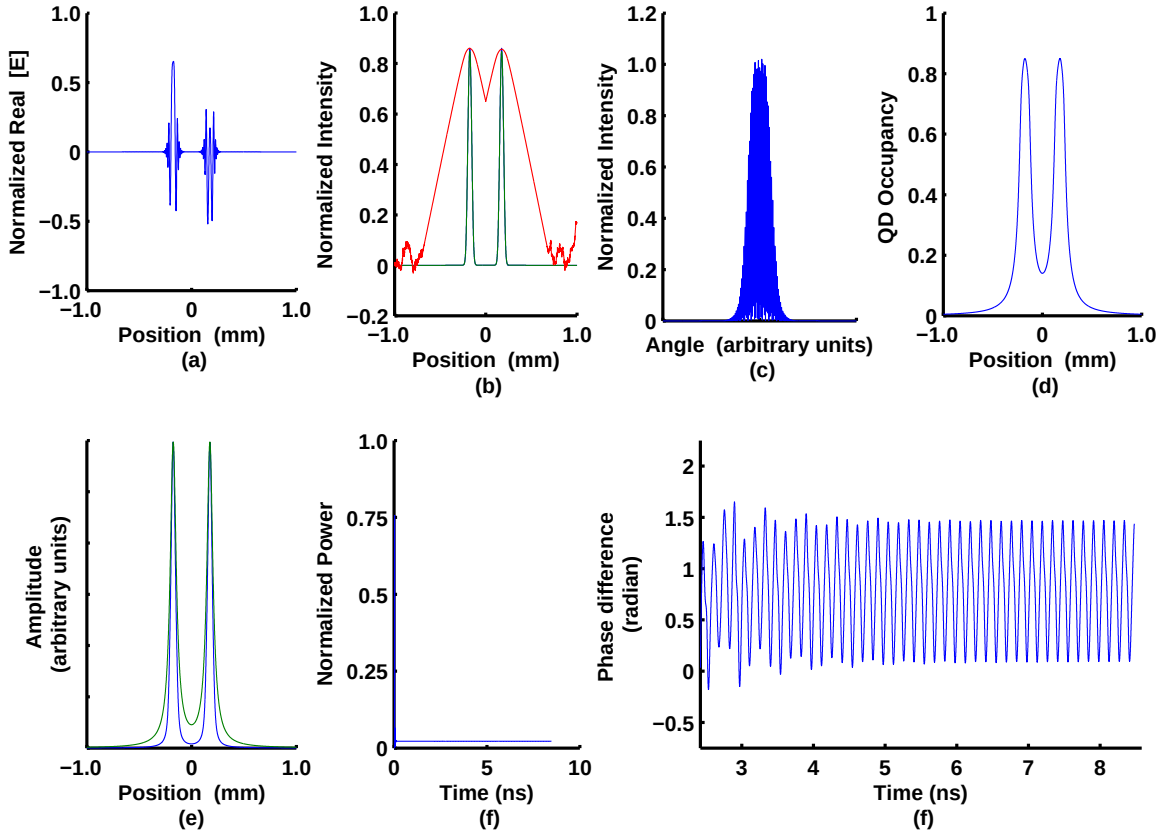

Figure 5.8: Simulated beam properties of QD laser array using rate equation approach for a 70 μm wide Lorentzian injection profile in the saturated regime ($\rho_{ss} = 0.9$) at 2 J_{th}, Lobe separation = 350μm and $\alpha = 9$. (a) Instantaneous near field electric field (b) instantaneous (blue) and time averaged (green) near field intensities, Phase (red) of near field (c) instantaneous far field intensities (d) QD occupancy (e) normalized injection profile (green) and non-resonant carrier profile (blue) (f) normalized output power as a function of time (g)Phase difference between the two counter-propagating traveling waves as a function of time.

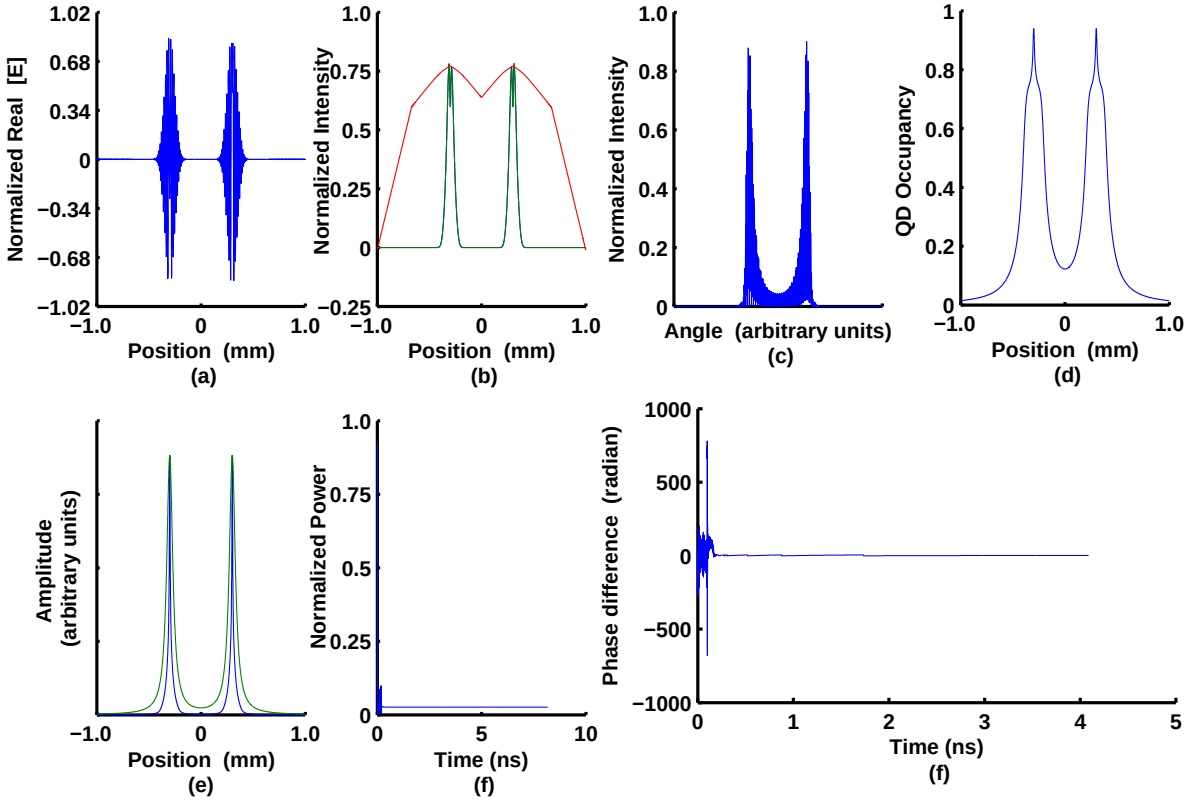

Figure 5.9: Simulated beam properties of QD laser array using rate equation approach for a 70 μm wide Lorentzian injection profile in the saturated regime ($\rho_{ss} = 0.9$) at 5 J_{th}, Lobe separation = $600\mu m$ and $\alpha = 9$. (a) Instantaneous near field electric field (b) instantaneous (blue) and time averaged (green) near field intensities, Phase (red) of near field (c) instantaneous far field intensities (d) QD occupancy (e) normalized injection profile (green) and non-resonant carrier profile (blue) (f) normalized output power as a function of time (g)Phase difference between the two counter-propagating traveling waves as a function of time.

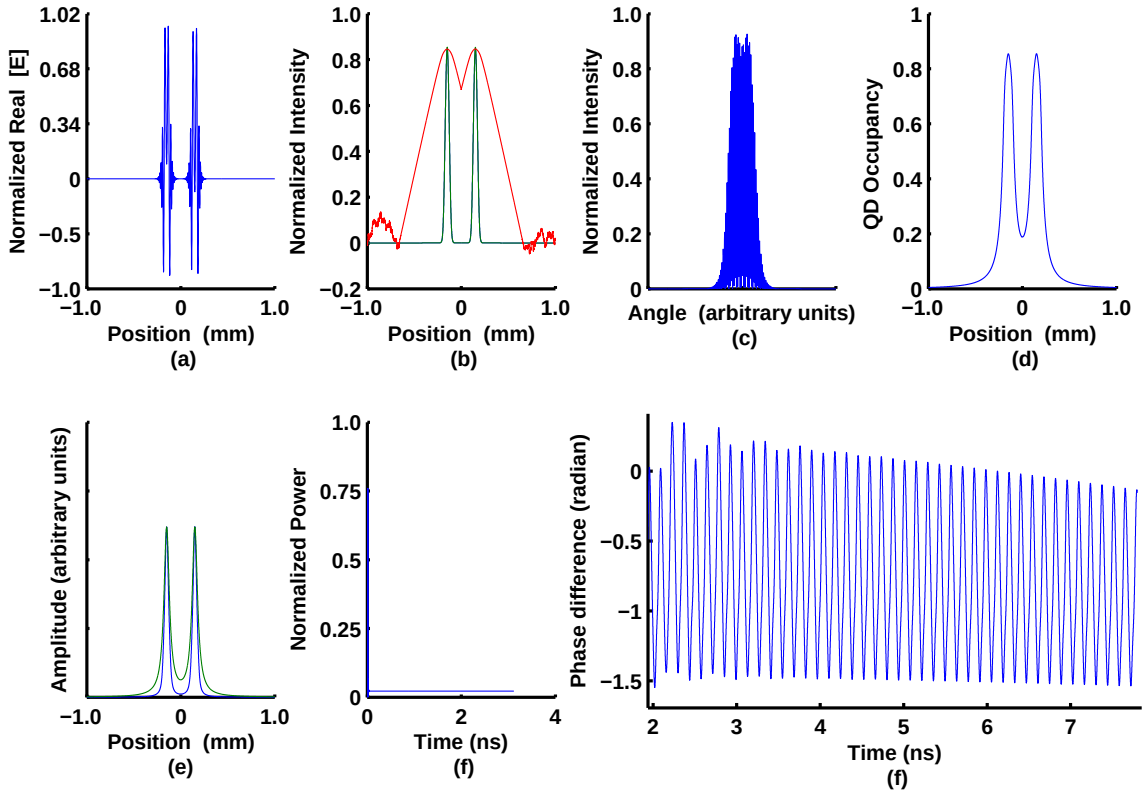

Figure 5.10: Simulated beam properties of QD laser array using rate equation approach for a 70 μm wide Lorentzian injection profile in the saturated regime ($\rho_{ss} = 0.9$) at 2 J_{th}, Lobe separation = 300μm and $\alpha = 9$. (a) Instantaneous near field electric field (b) instantaneous (blue) and time averaged (green) near field intensities, Phase (red) of near field (c) instantaneous far field intensities (d) QD occupancy (e) normalized injection profile (green) and non-resonant carrier profile (blue) (f) normalized output power as a function of time (g)Phase difference between the two counter-propagating traveling waves as a function of time.

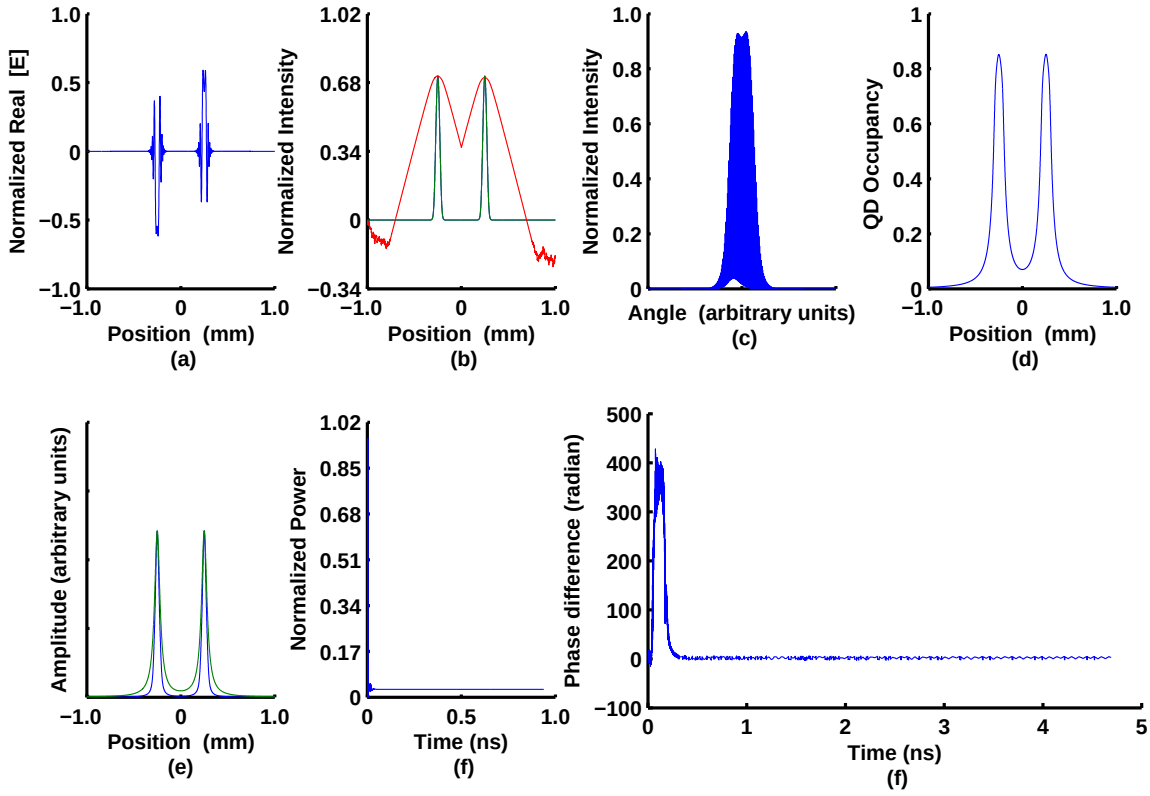

Figure 5.11: Simulated beam properties of QD laser array using rate equation approach for a 70 μm wide Lorentzian injection profile in the saturated regime ($\rho_{ss} = 0.9$) at 2 J_{th}, Lobe separation = $500\mu m$ and $\alpha = 9$. (a) Instantaneous near field electric field (b) instantaneous (blue) and time averaged (green) near field intensities, Phase (red) of near field (c) instantaneous far field intensities (d) QD occupancy (e) normalized injection profile (green) and non-resonant carrier profile (blue) (f) normalized output power as a function of time (g)Phase difference between the two counter-propagating traveling waves as a function of time.

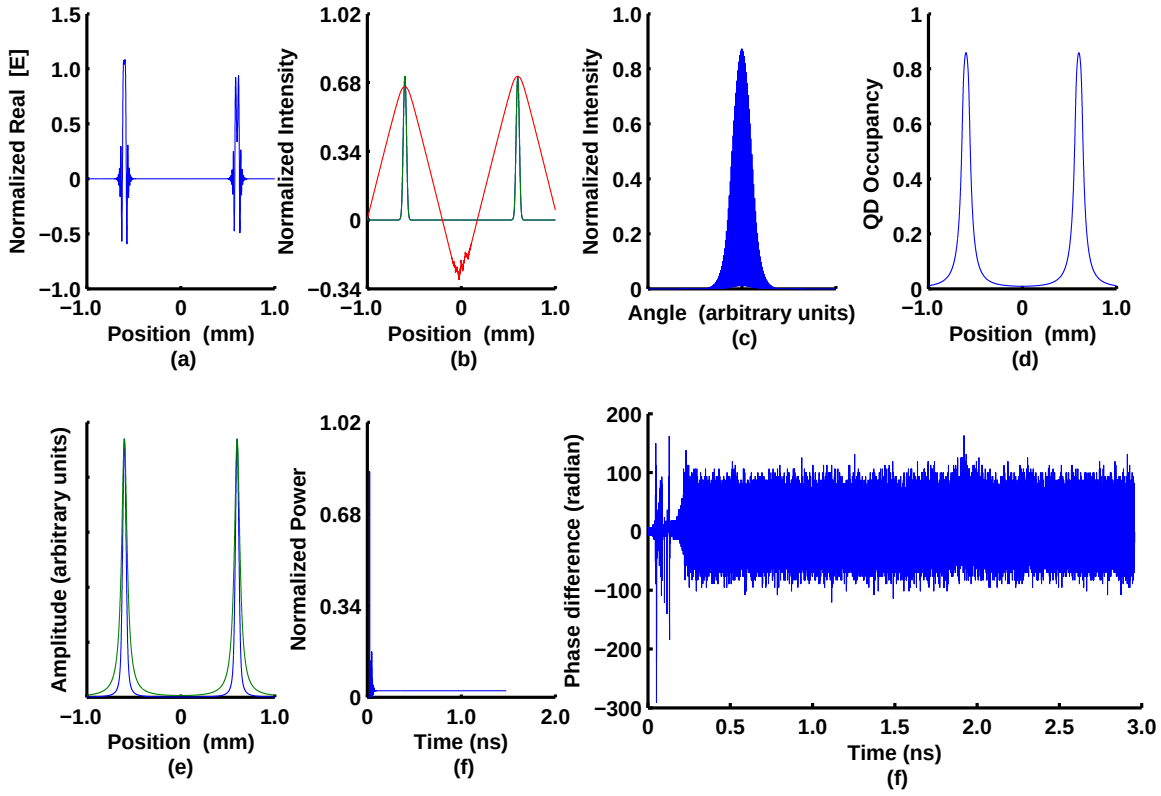

Figure 5.12: Simulated beam properties of QD laser array using rate equation approach for a 70 μm wide Lorentzian injection profile in the saturated regime ($\rho_{ss} = 0.9$) at 1.5 J_{th}, Lobe separation = 1200μm and $\alpha = 9$. (a) Instantaneous near field electric field (b) instantaneous (blue) and time averaged (green) near field intensities, Phase (red) of near field (c) instantaneous far field intensities (d) QD occupancy (e) normalized injection profile (green) and non-resonant carrier profile (blue) (f) normalized output power as a function of time (g)Phase difference between the two counter-propagating traveling waves as a function of time.

Figure [5.7] illustrates a phase locked output, figure [5.8] exemplifies a sinusoidal type drifting phase, and figure [5.9] illustrates a phase trending towards locked type. At first, it might seem that the figure [5.10] is drifting sinusoidally, however, on close inspection the phase difference between the two counter-propagating traveling waves as a function of time reveals a trending behaviour towards locked case. Figure [5.11] exemplifies an atypical drifting phase case. Finally, figure [5.12] illustrates an unlocked phase type.

Thus the above results point to several conclusions about the phase locking in injection profiled quantum dot lasers. First, the output behaviour shows a significant trending towards locking type where phase difference between the two counter-propagating traveling waves as a function of time ultimately comes to constant or zero. In order to prove this particular case a high performance computer machine is needed. Second, the occurrence of different types of phase relations cannot be grouped into classified regimes because the output pattern is irregular with respect to injection current and lobe separation. Therefore, the output behaviour from the coupled QD emitters is uncomparable to published results on coupled QW emitters by E. O'Neill et al [33]. Third, the stable output features have a large lobe separation width ($\geq$ 1200 μm). For example, a stable output with trending phase was observed at 5 J_{th} and 1200 μm lobe separation. Fourth, similar to the single injection current profiled QD emitter, the characteristic dip at the near field profile was observed for the two coupled injection profiled QD laser emitters case too (see figure [5.9]).

5.4.1.2 Unsaturated regime

The unsaturated QD case is highly unstable at 3 α_{th} for the 70 μm wider Lorentzian injection profile at different lobe separations raging from 250 μm to 1200 μm. Therefore, we didn't observed any classified phase relationships between the two coupled QD emitters here, which is in contrast to the saturated dot case.

5.4.2 Results from beam propagation method

The results from the beam propagation method are very similar to rate equation approach. However, the only difference is the instability level occurring at a lower injection level. Depending on the lobe separation the instability level ranges from 1.5 J_{th} to 2.5 J_{th} at $\alpha = 9$. An example of this approach for the saturated case is shown in Figure [5.13]. Figure [5.14] illustrates in- and out-of-phase locking when lobe separation between the two transversely coupled emitters is changed from 500 μm to 600 μm. Nevertheless, this is not similar to the one mentioned by E. O'Neill [33], where in - and out-of-phase locking between the two transversely coupled emitters were observed at recurring regular intervals when lobe separation was dynamically changed from 450 μm to 550 μm.

5.5 Discussions

In the preceding sections, the rate equation analysis of two transversely coupled injection profiled QD lasers was analyzed. In general, the observed output features based on phase relationship between the coupled emitters can be separated into four basic types: stable output with drifting phase, stable output with trending phase, stable output with unlocked phase and stable output with locked phase. However, in comparison to the previous work done by E. O'Neill et al, [33] on two transversely coupled large aperture semiconductor lasers through gain profiling, we do not observe clearly separated parameter regimes for the different output types. This contrasted behaviour can be attributed to the unique carrier dynamics of QD lasers. Moreover, stable output features have a wider lobe separation range than that of coupled QW emitters. This is because at increased pump level, the non-resonant carrier induced antiguiding at the center of the QD structure increases further, which in turn further stretches the optical mode.

During the numerical study of steady-state carrier beam propagation approach, the observed features were similar to 1-D rate equation approach but the simulation takes considerably less time scale to evolve. However, the instability level was substantially less compared to 1-D rate equation approach. This is due

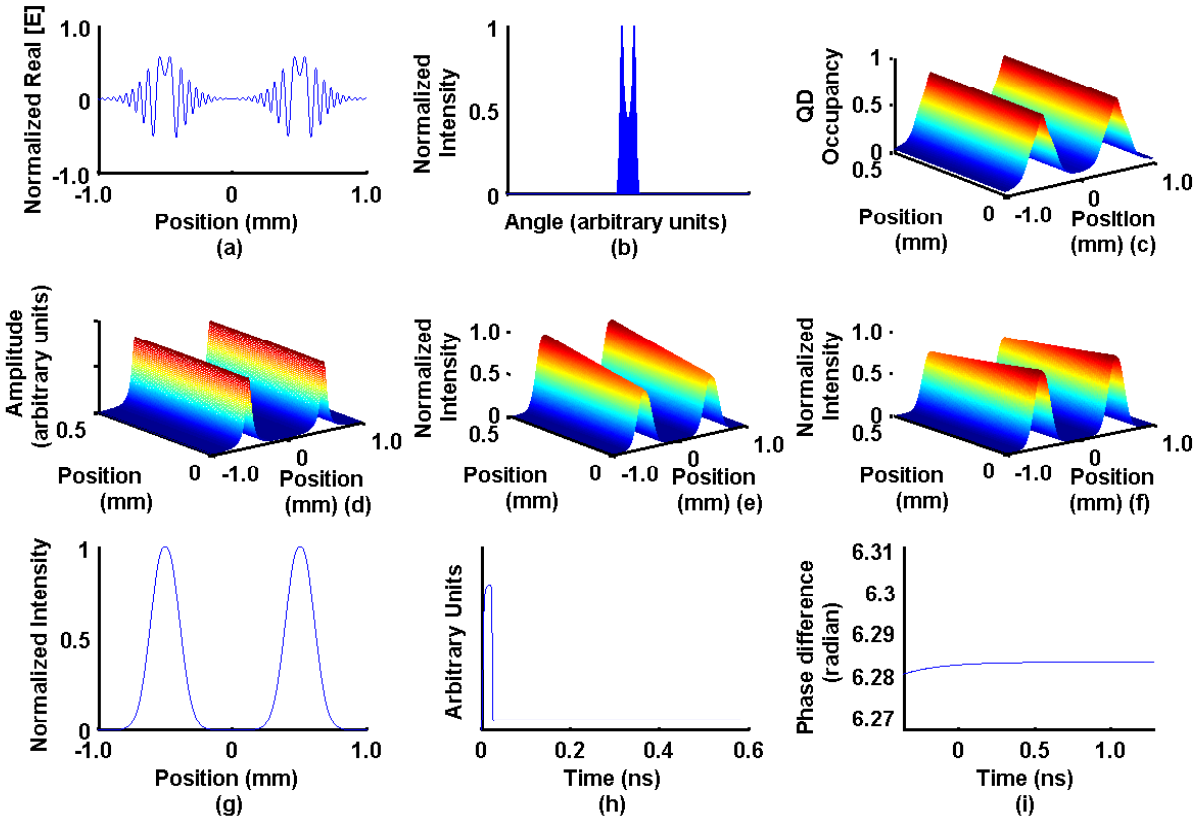

Figure 5.13: Simulated beam properties of two transversely coupled QD lasers using steady state carrier beam propagation approach for a lobe separation of $500\,\mu m$ and $70\,\mu m$ wide Lorentzian injection profile in the saturated regime ($\rho_{ss} = 0.9$) at $2J_{th}$ and $\alpha = 9$. (a) Instantaneous near field electric field (b) Instantaneous far field intensities (c) QD occupancy (d) non-resonant carrier profile (e) forward propagating intensity profile (f) backward propagating intensity profile (g) near field intensities (h) non-resonant carrier turn-on transient (i) Phase difference between the two counter-propagating traveling waves as a function of time.

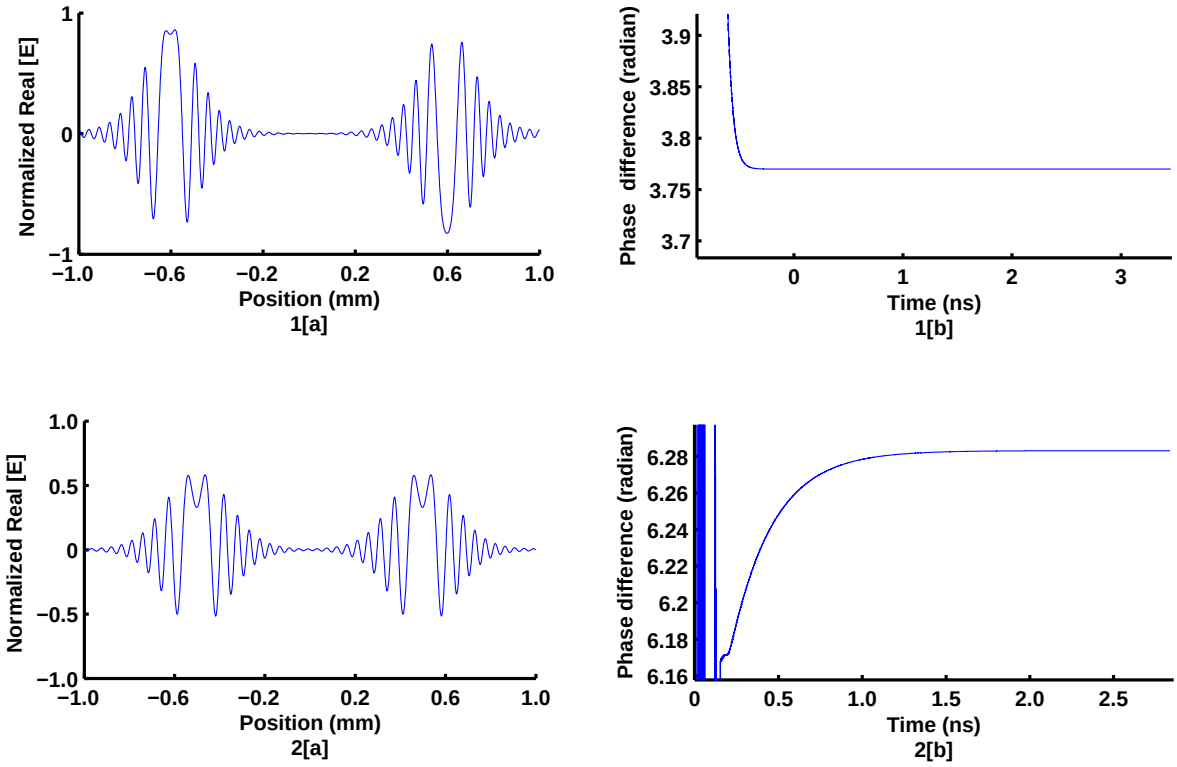

Figure 5.14: Simulated beam properties of two transversely coupled QD lasers using steady state carrier beam propagation approach for 70 μm wide Lorentzian injection profile in the saturated regime ($\rho_{ss} = 0.9$) at $2J_{th}$ and $\alpha = 9$. Figure series 1 represents out-of-phase locking and figure series 2 represents in-phase locking1[a] Instantaneous near field electric field and 1[b] Phase difference between the two counter-propagating traveling waves as a function of time at a lobe separation of 600 μm. 2[a] Instantaneous near field electric field and 2[b] Phase difference between the two counter-propagating traveling waves as a function of time at a lobe separation of 500 μm.

to limitations in the model, where at higher injection levels, the beam propagation approach does not produce a steady-state solution because of the time independent equations and steady-state carrier approximation, with energy oscillating greatly between the photons and the carriers [96].

5.5.1 Conclusions

The carrier dynamics of QD devices involves both resonant charge carriers and non-resonant charge carrier. When the resonant charge carrier population is close to saturation, further increase in the anti-guiding was observed, mainly due to non-resonant carrier buildup. Such a localized change in the non-resonant carriers leads to unique output behaviour and results in a modified phase relationships between the two coupled QD emitters when compared to published results on two transversely coupled injection profiled QW lasers by E. O'Neill et al [33].

Chapter 6

Focusing beam properties

Many semiconductor laser applications require good (TEM_{00} Gaussian mode) beam quality. For example: some scientific experiments require coupling the laser beam into a single mode fiber. In the publishing field, a high resolution printing in the range of 2400 to 3000 dpi would be required for some graphical applications, and the writing spot (or pixel) size should be as small as 2.5 to 10 μm [67]. Therefore, the characterization of a laser beam helps in defining the practical usage of the beam profile. Moreover, a proper way to characterize the laser beam has a significant purpose, as it helps in comparing the output beam profile with that of other laser diodes.

To examine the suitability of our QD laser device for such applications, we used a beam propagation algorithm to propagate the light from the output facet into free space in the presence of collimating and focusing lenses.

6.1 Background

In the following section, the Gaussian nature of the laser beam is discussed in detail, which is especially important in the understanding of output beam profiles.

6.1.1 Gaussian Laser beam

A Gaussian beam is a beam of electromagnetic radiation whose transverse electric field and intensity distributions can be approximated by the Gaussian function. In general, many lasers emit light beams that are Gaussian in nature. Moreover, the fundamental transverse mode (TEM_{00}) inside a laser cavity has a Gaussian profile, which when refracted by a lens, transforms into another Gaussian beam (characterized by a different set of parameters). Thus the study of Gaussian model has profound importance in the understanding of the laser light beams.

It is easier to analyze the laser beam by recognizing it as a 2-D problem, even though, the beam propagation is a three dimensional (3-D) job involving two transversal dimensions (x, y) and one axial dimension. The amplitude distribution of a Gaussian laser beam in 2-D form can be written as:

$$E(x,z) = E_0\sqrt{\frac{2}{\pi}}\frac{\omega_0}{\omega(z)}e^{(-j[\theta_0-\theta(z)])}e^{\left(\frac{-jkx^2}{2R(z)}-\frac{x^2}{\omega^2(z)}\right)} \tag{6.1}$$

The above equation [6.1] describes the behavior of the laser beam amplitude as a function of the transversal coordinate "x" and the axial coordinate "z". Here, $k = \frac{2\pi}{\lambda}$ represents the wave number, λ denotes the wavelength of the material where the beam propagates, $\omega(z)$ refers to the radius at which the field amplitude and intensity drop to $\frac{1}{e}$ and $\frac{1}{e^2}$ of their axial values respectively, $R(z)$ is the radius of curvature of the wavefronts comprising the beam and $\theta(z)$ stands for the divergence of the beam.

E_0 represents the value at $|E(0,0)|$ (see expression [6.1]), ω_0 refers to the value at $\omega(0)$ (see expression [6.3]), similarly, θ_0 stands for the value at $\theta(0)$.

The corresponding time averaged intensity (irradiance) distribution is given by:

$$I(x,z) \propto |E(x,z)|^2 = I_0\left(\frac{\omega_0}{\omega(z)}\right)^2 e^{\left(\frac{2x^2}{\omega^2(z)}\right)} \tag{6.2}$$

The detailed analysis of the Gaussian beam width in a way completes the total analysis of the electromagnetic (em) waves. Mathematically, the width of the

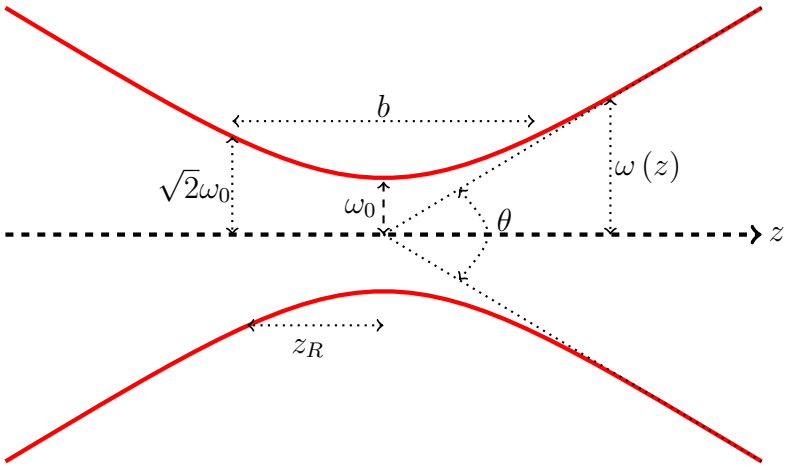

Figure 6.1: Schematic representation of Gaussian beam width $\omega(z)$ as a function of the axial distance z. ω_0 represents beam waist, b denotes depth of focus, z_R refers to Rayleigh range and θ stands for total angular spread

beam can be written as:

$$\omega(z) = \omega_0 \sqrt{\left(1 + \left[\frac{z\lambda}{\pi\omega_0^2}\right]^2\right)} \tag{6.3}$$

From the above equation, it is quite clear that the shape of the beam is a hyperbola of revolution about the z-axis. The divergence of the beam is the distance over which its cross-sectional area doubles, or equivalently, the value of z for which $\omega(z) = \sqrt{2}\omega_0$. This mentioned distance, z_R, is known as the "Rayleigh range" [1], and can be obtained from the above equation [6.3]. Quantitatively, the Rayleigh range is written as:

$$z_R = \frac{\pi\omega_0^2}{\lambda} \tag{6.4}$$

From the figure [6.1] and from the equations [6.3] & [6.4], it can be implicitly understood that if the light beam has a smaller waist or smaller the Rayleigh range then the beam diverges faster. The parameter $w(z)$ approaches a straight line for $z \gg z_R$. The angle between this straight line and the central axis of the beam is called the divergence of the beam. Mathematically, it is represented as:

[1]Note: confocal parameter or depth of focus is twice the Rayleigh range, i.e. $b = 2z_R$

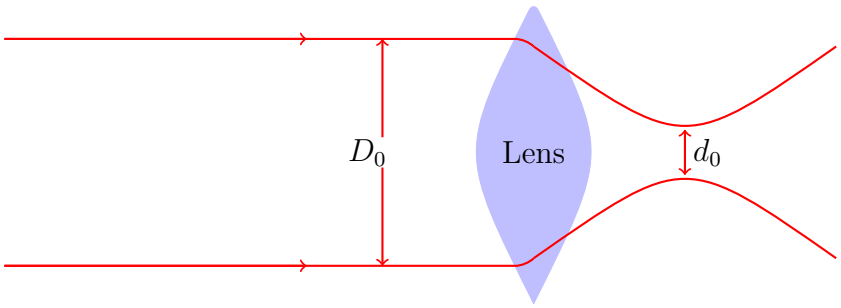

Figure 6.2: Schematic representation of Gaussian laser beam having a D_0 waist width focused to a d_0 waist size using a lens of known focal length f.

$$\varphi = \frac{\lambda}{\pi\omega_0} \tag{6.5}$$

The full angular width of the beam (θ) is given by the following expression:

$$\theta = \frac{2\lambda}{\pi\omega_0} = 0.637\frac{\lambda}{\omega_0} = 2\,\varphi \tag{6.6}$$

The diffraction limited spot size ω_s of the focused Gaussian beam can be described as:

$$\omega_s = \frac{f\,\theta}{2} = f\,\varphi \tag{6.7}$$

Where "f" is the focal length and "θ" is the full angular width of the beam.

Previously, a Gaussian fit to the laser beam profile has been used to measure how close the beam is to TEM_{00}. This particular type of evaluation suffers from drawbacks as many multimode combination of laser beams have a nearly perfect Gaussian shape [2]. In conclusion, the Gaussian fit does not answer the mode characteristics of the laser beam.

6.1.2 Beam propagation factor $\left(M^2\right)$

Beam propagation factor answers the mode characteristics of the laser beam correctly (see table [6.1]). However, this particular concept is not exceptionally

Laser Mode	M^2
TEM_{00}	1
TEM_{01}	2
TEM_{10}	3
TEM_{11}	4
TEM_{20}	5
TEM_{21}	6

Table 6.1: Beam profile comparisions

popular because the difficulty of making an accurate measurement. Precisely, it cannot be determined with a single calculation.

The International Organization for Standardization (ISO) committee has defined a methodology for a reliable measurement of M^2. The procedure involves placing a lens of a known focal length in a laser beam, then making a series of measurements along the focused waist of the beam. The measured M^2 parameters like width of the spot ultimately reveal the M^2 value. Mathematically, it can be written as [68]:

$$M^2 = \frac{\pi d_0 D_0}{4\lambda f} \tag{6.8}$$

and the beam divergence (φ) can be obtained as:

$$\varphi = \frac{d_0}{f} \tag{6.9}$$

Where λ is the wavelength, f is the focal length, D_0 is the waist width of the input multimode laser beam and d_0 is the waist width of the output multimode focused laser beam.

From the above table [6.1] and from the equation [6.8] it can be concluded that, if a beam have $M^2 = 4$, then the focused spot size is four times larger than would be obtained with a TEM_{00} beam.

6.1.3 Beam diameter

The beam diameter or beam width of the laser do not have sharp edges, so the diameter can be obtained in many different ways. Generally, beam diameter

refers to a beam of circular cross section, but not necessarily so. For example, with an elliptical beam the orientation of the beam diameter must be specified with respect to the major or minor axis. Currently, five different ways of defining the beam width are in use: $D4\sigma$ or second moment width, $\frac{10}{90}$ or $\frac{20}{80}$ knife-edge, $\frac{1}{e^2}$, FWHM, and $D86$. Only FWHM and $\frac{1}{e^2}$ are defined below, as these are used in the current investigation of the QD beam profile.

6.1.3.1 Full width half maximum ($FWHM$)

This is the easy way to define the beam width of the laser. Two diametrically opposite points at which the irradiance reduces to half from a specified peak irradiance is called FWHM.

6.1.3.2 $\frac{1}{e^2}$ width

In this case, the distance between the points where the intensity falls to $\frac{1}{e^2} = 0.135$ times the maximum value is called the $\frac{1}{e^2}$ width.

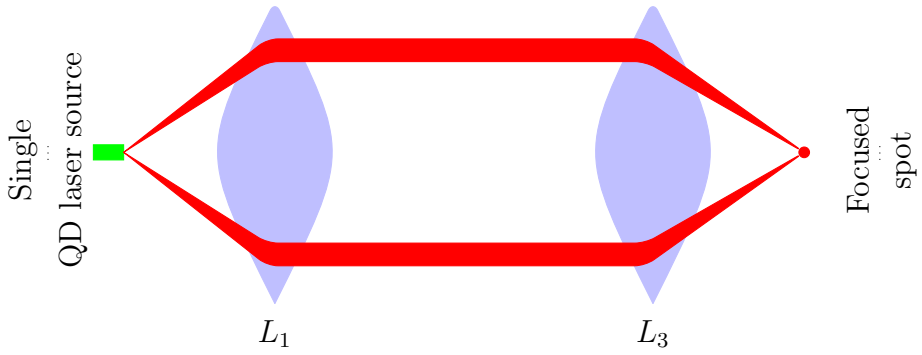

Figure 6.3: Schematic representation of focusing alignment of single QD laser. In the figure, L_1 represents the collimating lens, whereas L_3 represents focusing lens.

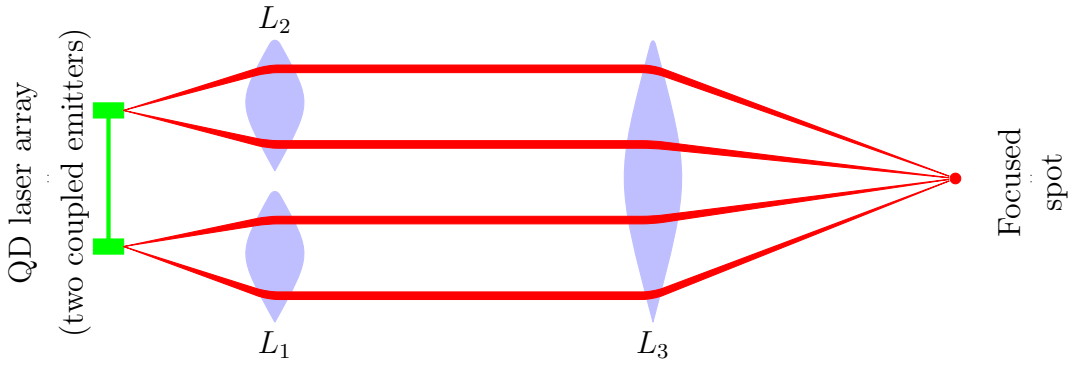

Figure 6.4: Schematic representation of focusing alignment of QD laser array having two coupled emitters. In the figure, L_1 and L_2, represents the collimating lens, whereas L_3 represents focusing lens.

6.2 Method

The light coming out from the laser diode is highly divergent and astigmatic in nature. It requires a special type of lens for collimation. However, for the sake of simplicity in our simulation we have taken a simple convex lens for both collimation and focusing. In the single QD laser case, a collimating lens was used to collimate the light output, and a focusing lens was used to bring the collimated output to a focus. In the case of two transversely coupled QD emitters, two separate but identical lenses, centered at the middle of each emitter were used to collimate the

light output and a single focusing lens was used to bring the collimated output to a focus (see figure [6.3]).

The lens equation is described as:

$$E\left(x, y, z_{after\ lens}\right) = E\left(x, y, z_{before\ lens}\right) e^{-j\left(\frac{kz^2}{2f}\right)} \tag{6.10}$$

Where "$E\left(x, y, z_{after\ lens}\right)$", "$E\left(x, y, z_{before\ lens}\right)$" represents the electric field after passing through the lens and before going through the lens, respectively. The "k" stands for wavenumber in vacuum $\left(i.e.\ \frac{2\pi}{\lambda}\right)$, "$f$" denotes focal length and "z" refers to propagating direction.

To maintain a small beam diameter of the collimated light, one has to use a lens with shorter focal length. However, smaller focal length leads to a higher beam divergence of the collimated beam.

The equation for the propagating electric filed in the free space is given as:

$$\frac{\partial E}{\partial Z} = \frac{j}{2K_z}\frac{\partial^2 E}{\partial x^2} \tag{6.11}$$

Where $K_z = \eta K_0$ is the propagation constant.

The above equation [6.11] is same as Eq [4.4] minus the gain term. This is due to no absorbing material to change the gain of the electric field in the free space.

In this chapter, the simulation results (output beam profiles) from rate equation approach (see chapter [3] & [5]) were used to study the focusing properties of the single QD laser and the QD laser array.

6.3 Results

In the present beam propagation approach, steady state electric field from the QD laser device simulated through rate equation approach was made to propagate in the free space by using Eq. [6.11] and then through the lens by using the Eq. [6.10].

Only beam waist in the transverse direction was measured as the previous laser simulation analysis (rate equation approach) was carried out on that dimen-

sion. Therefore, the confocal parameter (b) could not be calculated as the beam waist measurements were done in the transverse dimension and had to be treated as a separate variable vis-a-vis confocal parameter. The laser beam waist was calculated using the $\frac{1}{e^2}$ method.

6.3.1 Single QD laser

6.3.1.1 Saturated regime

We examined wider 70 μm injection profile case at high $\alpha = 9$ factor for saturated $\rho_{th} = 0.9$ dots at various injection currents. The figures [6.5] & [6.6] illustrates the light coming out from the output facet into free space in the presence of collimating and focusing lenses at $3.5J_{th}$ and $7.5J_{th}$ respectively. The near field profile changes from a single lobe at $3.5J_{th}$ injection to a lobe with a strong characteristic dip at the center of the profile at $7.5J_{th}$ injection. Such a profile change should lead to different beam waists and M^2 values. Exactly, this happened in our measurements.

The calculated beam waist at the focus section for the figure [6.5] is $\sim$ 22.1 μm and for figure [6.6] is $\sim$ 55.58 μm. Here, beam waist measurements are corrected to identical lenses case, where collimating lens and focusing lens have same focal length. This type of calculations is useful to compare the results to previous studies of beam propagation approach in QW devices by E. O'Neill et al [33].

The M^2 values [2] for the figure [6.5] is 0.72, which is theoretically impossible because M^2 factor cannot assume values less than 1. The M^2 values for figure [6.6] yeilded 3.75. It is worthwhile highlighting that, as the injection is varied from $1.5J_{th}$ to $11.5J_{th}$, the M^2 values varies from 0.72 to 8.67 correspondingly, however, with few exceptions (see figure [6.11]). Moreover, for $< 4\ J_{th}$ values, we observed a $M^2 < 1$ value for single QD laser device in the saturated regime.

[2] M^2 calculations are based on uncorrected beam waist

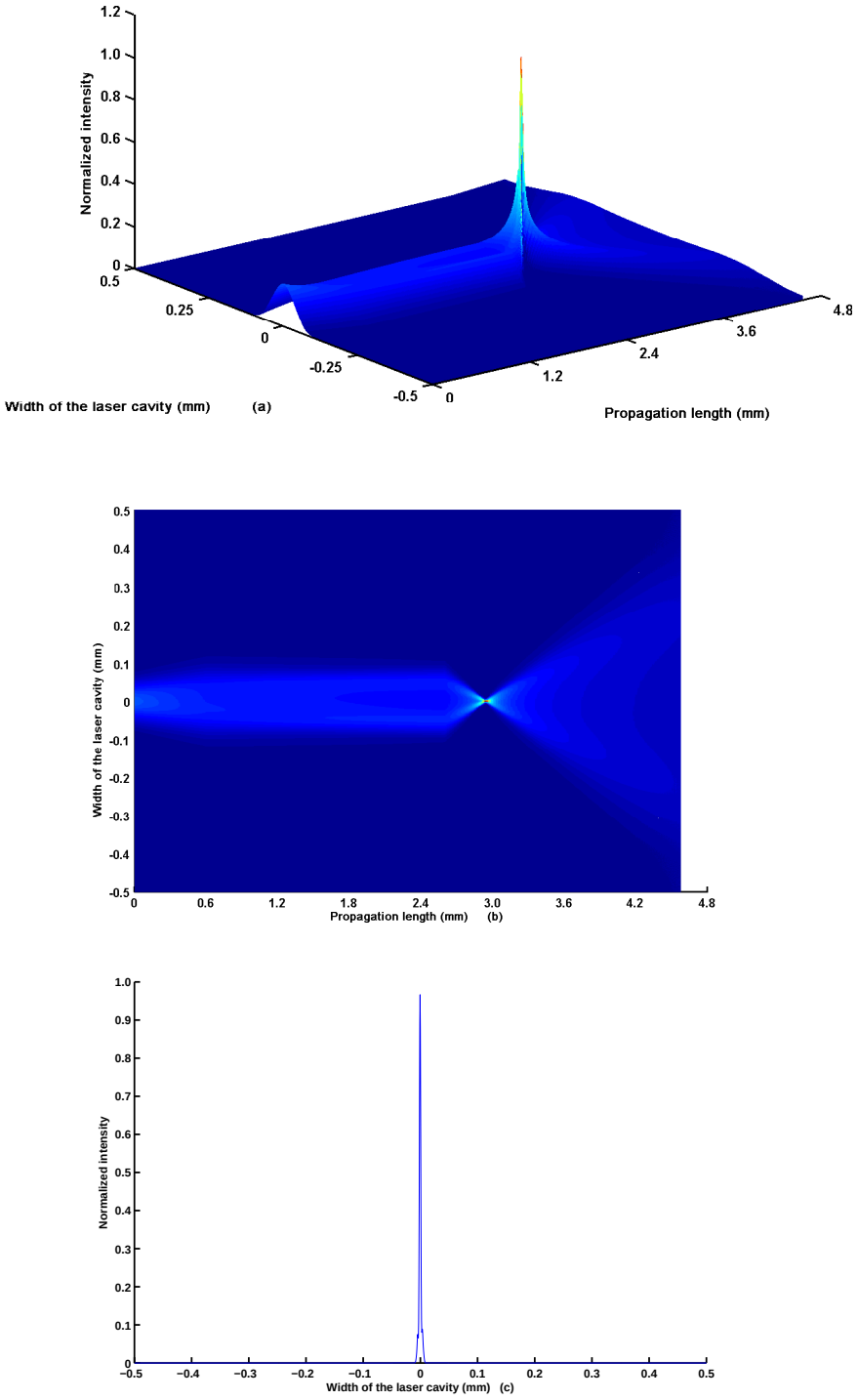

Figure 6.5: Simulated focusing beam properties of single QD laser for a 70 μm wide Lorentzian injection profile in the saturated regime ($\rho_{ss} = 0.9$) at $\simeq 3.5 J_{th}$ and $\alpha = 9$. The focal length of the lenses are: $L_1 = 1.3\,mm$, $L_3 = 0.5\,mm$ and the total propagation length is: 4800 μm (a) 3-D illustration (b) 2-D illustration (c) Focus point irradiance profile.

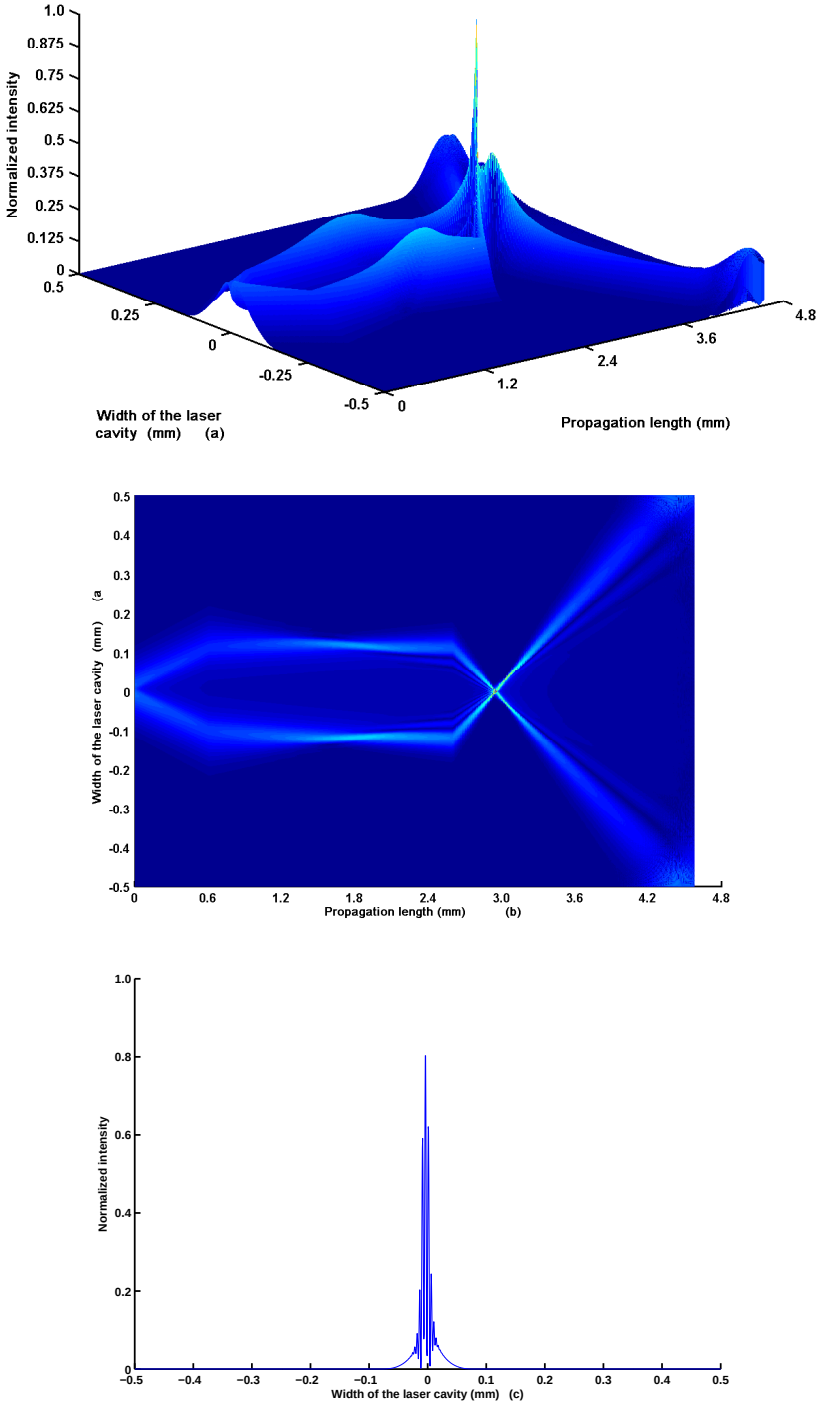

Figure 6.6: Simulated focusing beam properties of single QD laser for a 70 μm wide Lorentzian injection profile in the saturated regime ($\rho_{ss} = 0.9$) at $\simeq 7.5 J_{th}$ and $\alpha = 9$. The focal length of the lenses are: $L_1 = 2.9\, mm$, $L_3 = 0.6\, mm$ and the total propagation length is: 4800 μm (a) 3-D illustration (b) 2-D illustration (c) Focus point irradiance profile.

6.3.2 QD laser array

The next case in the simulation was to examine two transversely coupled injection profiled QD emitters. For the parameter values $\rho_{th} = 0.9$, $J_{th} = 3.5$, $\alpha = 9$ and lobe separation $= 500\,\mu m$, a snapshot of the light coming out from the output facet into free space in the presence of collimating and focusing lenses is shown in figure [6.7]. In this case, the near field has a single lobe with no characteristic dip at the center with M^2 value at 2.02, and the beam waist at the focus section about $\sim 13.5\,\mu m$.

In the simulation, when the coupled emitter is operated at high injections, the near field profile changes from simple single lobe to a lobe with strong characteristic dip at the center for $\alpha = 9$. A snapshot of such a case, where light coming out from the output facet into free space in the presence of collimating and focusing lenses is shown in figure [6.8] for parameter values $\rho_{th} = 0.9$, $11.5J_{th}$ and lobe separation $= 500\,\mu m$. In this case, the beam waist at the focus section is $\sim 126\,\mu m$, and M^2 value at 23.07.

6.3.3 Comparison

The figure [6.9] illustrates beam waist comparison between single injection profiled QD emitter and two transversely coupled injection profiled QD emitters at various injection currents. If the steady state electric field between the coupled emitters is phase locked then we have a beam waist at the focus point which is considerably less, compared to the single QD emitter. This particular case occurred in our simulation analysis at $3.5J_{th}$ (See figures [6.10] & [6.9]). However, if the steady state electric field between the coupled emitters is not phase locked then the beam waist at the focus point is substantially greater, compared to the single QD emitter, which occurred in the simulation at $1.5J_{th}$, $5.5J_{th}$, $7.5J_{th}$, $9.5J_{th}$ and $11.5J_{th}$.

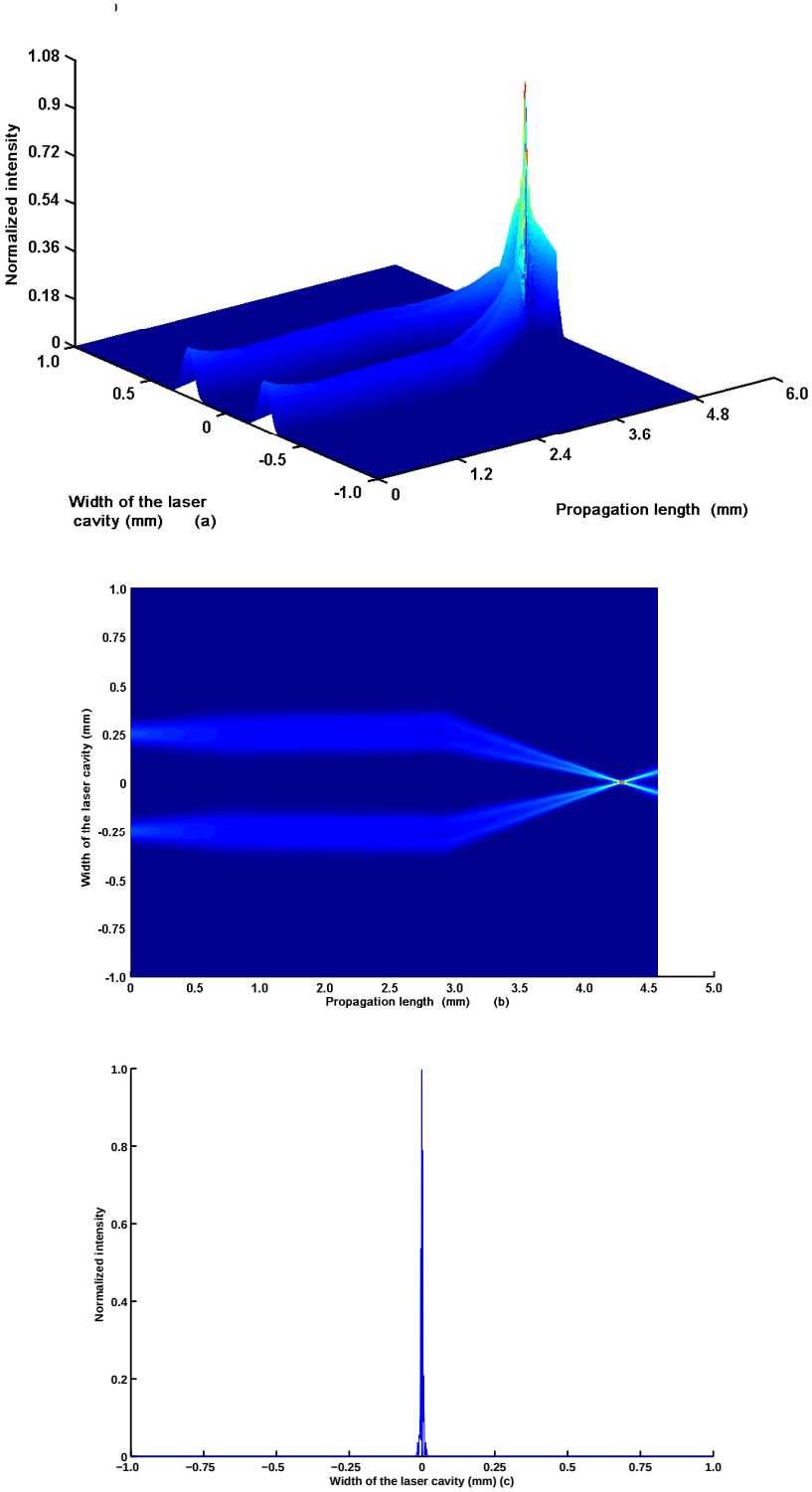

Figure 6.7: Simulated focusing beam properties of QD laser array for a 70 μm wide Lorentzian injection profile with a lobe separation of 500 μm in the saturated regime ($\rho_{ss} = 0.9$) at $\simeq 3.5 J_{th}$ and $\alpha = 9$. The focal length of the lenses are: $L_1 = 1.8\, mm$, $L_2 = 1.8\, mm$ $L_3 = 2.0\, mm$ and the total propagation length is: 5000 μm (a) 3-D illustration (b) 2-D illustration (c) Focus point irradiance profile.

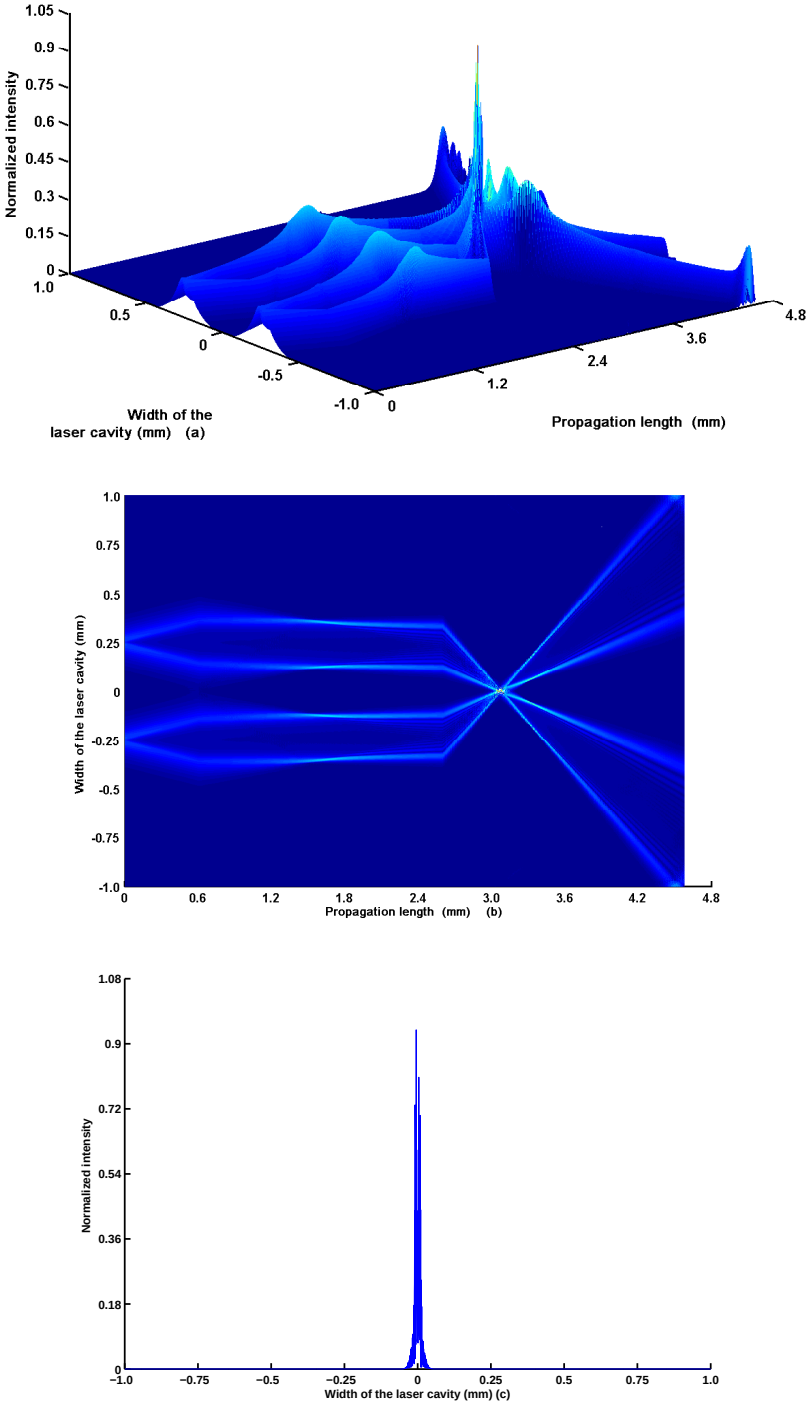

Figure 6.8: Simulated focusing beam properties of QD laser array for a 70 μm wide Lorentzian injection profile with a lobe separation of 500 μm in the saturated regime ($\rho_{ss} = 0.9$) at $\simeq 11.5 J_{th}$ and $\alpha = 9$. The focal length of the lenses are: $L_1 = 1.8\, mm$, $L_2 = 1.8\, mm$ $L_3 = 0.5\, mm$ and the total propagation length is: 4800 μm (a) 3-D illustration (b) 2-D illustration (c) Focus point irradiance profile.

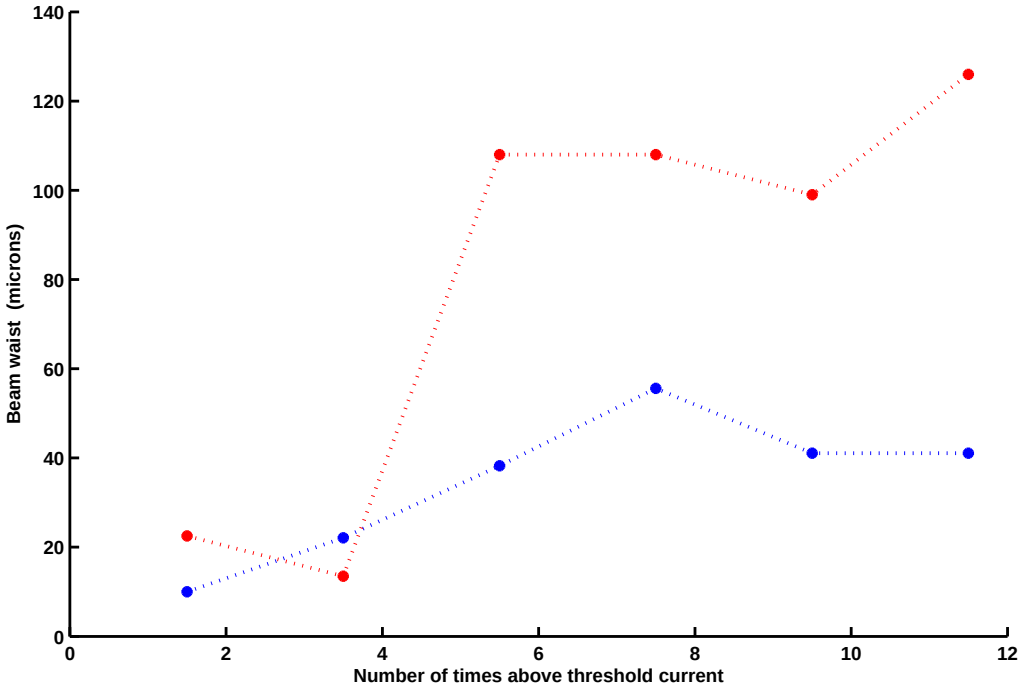

Figure 6.9: Schematic representation of J_{th} vs beam waist at the focus point for single QD laser (blue) and QD laser array (red). Parameters used in the simulation (for both single QD laser and QD laser array) are: wide (70 μm) Lorentzian injection profile in the saturated regime ($\rho_{ss} = 0.9$) at $\alpha = 9$. For QD laser array, lobe separation was maintained at (500 μm).

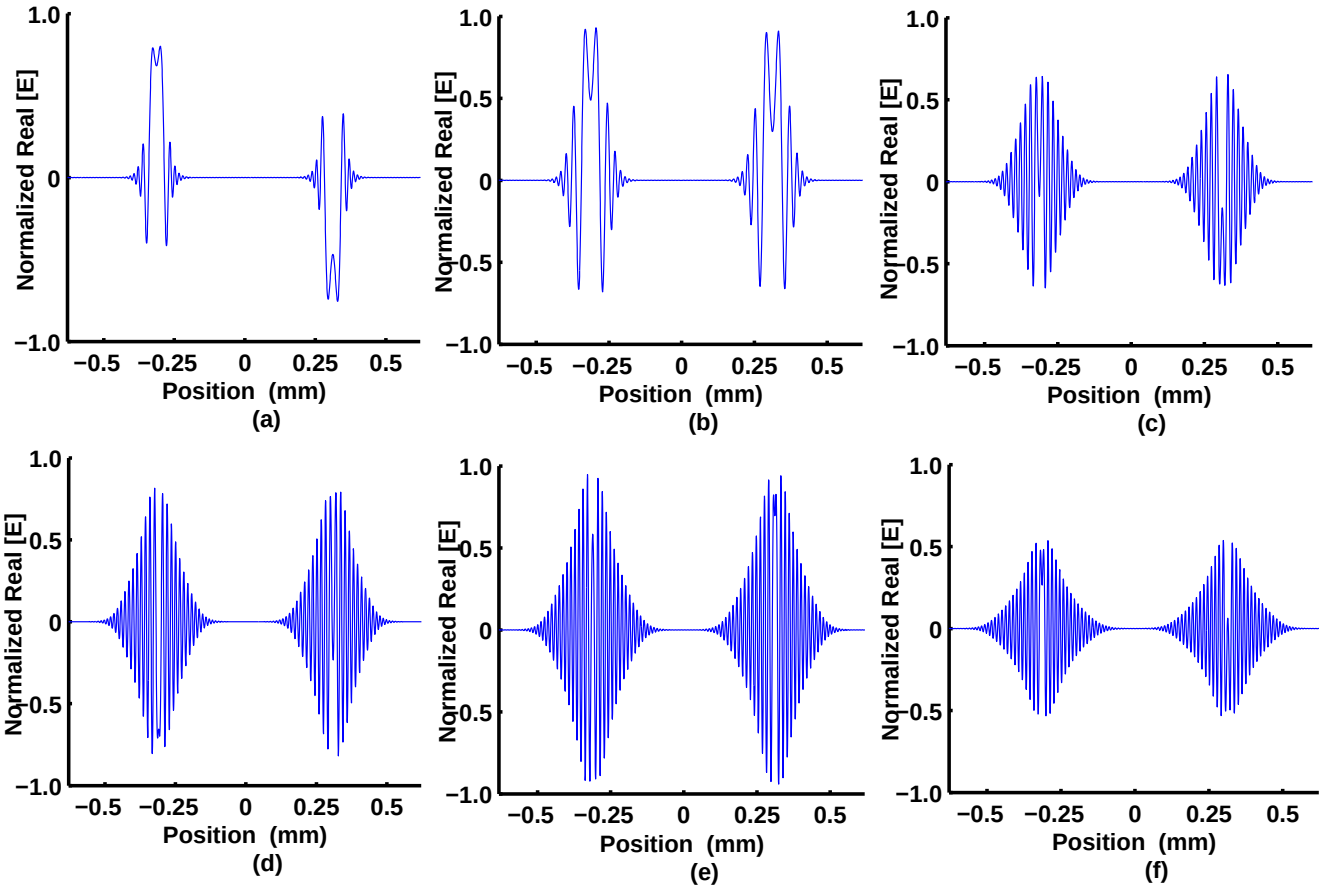

Figure 6.10: Simulated instantaneous near field electric field profile of two transversely coupled injection profiled QD emitters using rate equation approach at various injection currents. Parameters used in the simulation are: 70 μm wide Lorentzian injection profile in the saturated regime ($\rho_{ss} = 0.9$) at $\alpha = 9$ with 500 μm Lobe separation. (a) $1.5J_{th}$ (b) $3.5J_{th}$ (c) $5.5J_{th}$ (d) $7.5J_{th}$ (e) $9.5J_{th}$ (f) $11.5J_{th}$.

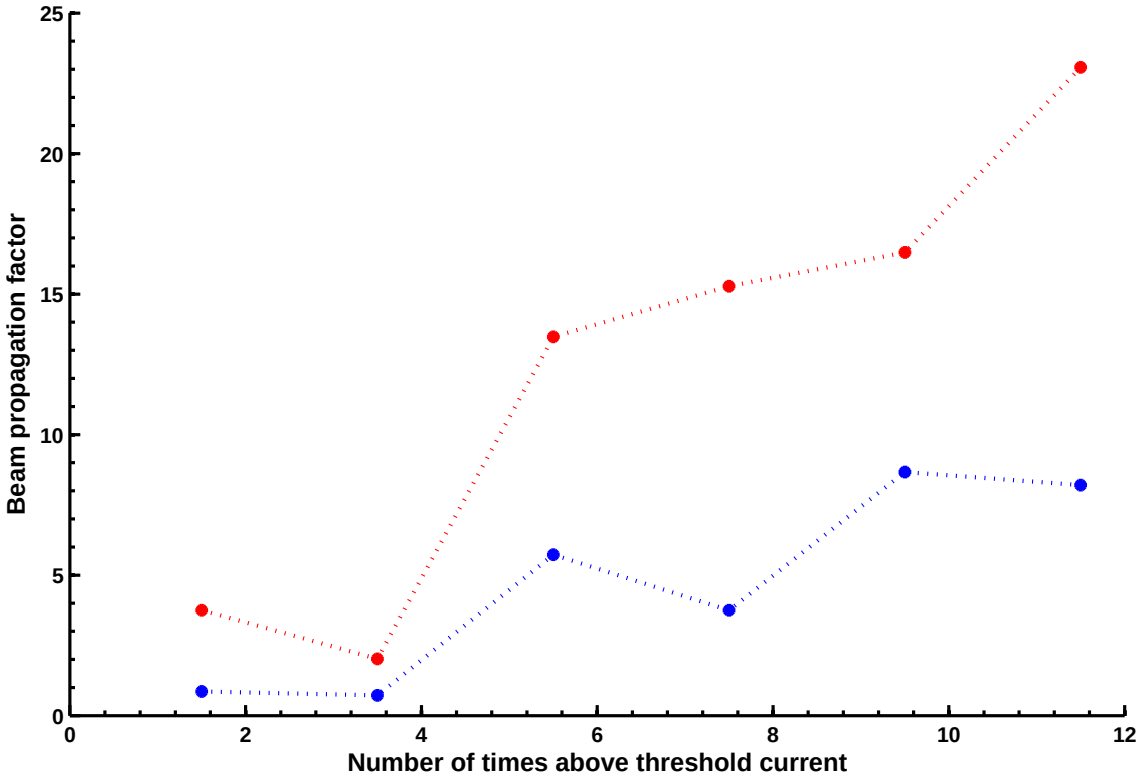

Figure 6.11: Schematic representation of J_{th} vs M^2 for single QD laser (blue) and QD laser array (red). Parameters used in the simulation (for both single QD laser and QD laser array) are: wide (70 μm) Lorentzian injection profile in the saturated regime ($\rho_{ss} = 0.9$) at $\alpha = 9$. For QD laser array, lobe separation was maintained at (500 μm).

To characterize the laser beam correctly, we utilised M^2 measurements, since the beam waist measurements can't reveal the type of TEM mode emanating from the injection profiled QD laser. The figure [6.11] illustrates the M^2 comparison between single injection profiled QD emitter and two transversely coupled injection profiled QD emitters at various injection currents. From the figure [6.11], it can be concluded that the coupled QD emitters oscillate in higher transverse mode compared to single QD emitter at all injection currents.

6.4 Discussions

For both single injection profiled QD laser and two transversely coupled QD lasers, the beam waist measurements at the focus point reveal a general picture that as the injection level is raised the beam waist dimension also raises significantly. Similarly, M^2 values also raises as the injection level is raised for both single injection profiled QD emitter and two transversely coupled QD emitters. In the earlier study on two transversely coupled QW emitters by E. O'Neill et al[33], the phase locked regime have a reduced beam waist at the focus point compared to single QW emitter at the same pump level. A similar result was observed for two transversely coupled QD emitters at 3.5 J_{th} (see figure [6.11] & [6.10]).

Typically, a general broad-area semiconductor laser will have M^2 value in the range $10 \sim 50$ depending on the bias injection current and the stripe width [5]. In our approach on injection profiled quantum dot lasers, M^2 values range from 0.72 to 8.67 for single QD emitter and from 2.02 to 23.07 for two transversely coupled QD emitters (See figure [6.11]).

A surprising behaviour was observed in our results for the single QD laser device at low injection currents ($< 4J_{th}$), the reported M^2 values are less than 1, whereas beam propagation factor cannot assume values less than 1 [65]. According to International standard (ISO), the most reliable and consistent way to measure the width of the laser beam is through second order moments ($D4\sigma$) method [68]. Eventhough, the use of the M^2 factor as a main way of evaluating laser beam is more and more frequent nowadays. Some main objections to the practice still exist because the beam propagation factor is defined in terms of second-order moments ($D4\sigma$), where beam waist measurements are often somewhat problematic to measure[68]. In our simulation approach, the beam waist measurements were done using $\frac{1}{e^2}$ method. Therefore, the surprising behaviour in our results can be attributed to inadequateness in the $\frac{1}{e^2}$ method. However, our results on the beam propagation factor rightly reveal a multimode lasing behaviour, which is intrinsic to general broad area laser sources. These multimode beam characteristics affect both depth of focus and energy profile when the beam is focused to a tight spot. This is because the multiple modes have a localized spatial coherence within the

converging light beam that causes the light to focus differently from the main beam [67].

The main reason for the increase in the beam waist dimensions and the beam propagation factor values as the injection level is raised is due to nature of the antiguiding structures. A step up in the injection level increases the antiguiding which in turn stretches the optical mode instead of confining it. Thus the reduction in the optical mode confinement leads to multimode behaviour.

6.4.1 Reliability

The simulation results are yet to be compared with the experimental ones. So the reliability of our simulation results using beam propagation approach can not be essayed.

6.5 Conclusions

We have characterized the light beam emanating from the injection profiled QD laser and two transversely coupled injection profiled QD emitters through beam propagation approach. The beam waist dimensions and the beam propagation factor values rise with an increase in the injection level. The beam propagation factor values reveal a multimode lasing behaviour at high injection currents.

Chapter 7

Thesis conclusion and further work

Earlier results of injection current profiling on broad area QW lasers reported a non-filamentary output with an ensuing far-field profile made up of two counter-propagating transverse travelling waves emitted at the centre of the pumped region [9]. Similarly, the effect of such an injection current profiling on the beam properties of broad area QD device were experimentally examined by J. Houlihan et al [16]. This thesis work's main objective was to analyze the performance of injection profiled quantum dot lasers for high brightness applications through numerical simulations so that a comparison can be made with the observed experimental results. A variety of modelling types was employed to understand the beam properties of injection profiled quantum dot lasers and reproduce initial experimental results. In chapter [3], using 1-D rate equations representing the transverse dimension, the role of non-resonant carries was identified in the occurrence of a characteristic dip at the center of the near field intensity profile. Furthermore, spontaneous symmetry breaking at high injections was observed in the simulation, similar to the one observed in the experiment [16]. In chapter [4], a steady state beam propagation approach was employed to explored both the longitudinal and transverse dimensions of the QD laser. In addition to the characteristic dip, a characteristic bulging of non-resonant carrier profile along the longitudinal dimension was identified. In chapter [5], the possibility of coherent

arrayed emission was examined by calculating the phase relationship between two coupled injection profiled quantum dot lasers. In contrast to similar calculations using quantum well emitters, the classification of the output into distinct regimes was less apparent however, overall, a wider range of stable output was inferred. In chapter [6], the beam properties of single and double emitters was examined using a beam propagation approach. Both beam waist measurements and the beam propagation factor reveal a steady reduction in the overall beam quality with respect to increased injection currents.

To further investigate the potential of injection profiled quantum dot lasers for high brightness application, future numerical studies should involve exploring more sophisticated models based on a fully spatially resolved dynamic carrier approach. This can be used to validate the modelling results already produced and provide more accurate predictions on the behaviour of future devices. In general, such models are quite complicated and require significant computer resources and time to produce results. Of course, additional measurements will also be required to test the predictions in this thesis and coming from future modelling work.

However, before moving to the full spatio-temporal description some simple modifications of the 1-D rate equation approach may prove fruitful. For example, the role of excited state carriers has recently been highlighted in quantum dot lasers [31] and absorbers [99]. Incorporating the possibility of lasing from excited dot states and introducing different relaxation timescales for electrons and holes into the rate equations may indicate other opportunities for high brightness applications. In addition, both the steady state carrier beam propagation method and the 1-D rate equation approach to incorporate temperature effects would be particularly important for high brightness emitters where such effects may play a dominant role at high output powers. This approach can be very challenging because of the difference in thermal time scales (microseconds) when compared to photon density timescales (picoseconds). These are some modifications which may be made to produce more accurate predictions before moving to the full 3-D spatio-temporal modelling and experimental investigation.

So far in our research work we have focused on injection current profil-

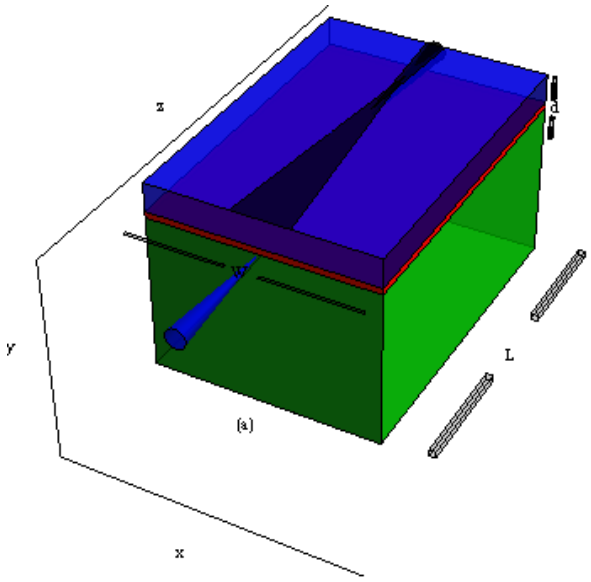

Figure 7.1: Schematic 3-D representation of curved facet having bow-tie injection contact (black). Here, active region $InGaAsP$ (red), substrate $n-InP$ (green), top layer $p-InP$ (blue) and light output [cone shaped] (blue). The laser cavity is in the axial (or longitudinal) direction [z], [y] represents lateral or vertical direction, and [x] denotes transverse direction. The active region below the contact area has a axial length (L), transverse width (W) and a vertical height (d).

ing of broad area QD lasers having plane cavity mirrors. It has been reported that a much improved beam quality can be obtained from broad area lasers using unstable resonators [97] [98]. A first examination of such an approach could be simulated easily. For example, an injection profiled QD laser having a bow-tie injection contact and unstable resonators could initially be examined using the steady state beam propagation method and compared to the performance of the injection current profiled QD lasers having plane resonators with rectangle type injection contact. Furthermore, the obtained results from such a modelling can be compared to the published results on injection profiled QW lasers having bow-tie injection contact and unstable resonators by Y. Tanguy et al [98].

Bibliography

[1] John Houlihan, "Spatial dynamics of semiconductor lasers", PhD thesis, National University of Ireland, Cork, (2002).

[2] Anthony E. Siegman, "Lasers", University Science Books, ISBN: 978-0-935702-11-8, (1986).

[3] Vinod Vukkalam and John Houlihan, "Beam properties of injection profiled quantum dot lasers", Optics Communications, Volume: 283, Issue: 12, Pages: 2596-2602, (2010).

[4] Dieter Bimberg, Marius Grundmann and Nikolai N. Ledentsov, "Quantum Dot Heterostructures", John Wiley and Sons, ISBN : 0471973882 9780471973881, (1999).

[5] Junji Ohtsubo, "Semiconductor Lasers: Stability, Instability and Chaos", Springer, ISBN: 978-3-540-72647-0, (2008).

[6] Z. Mi , P. Bhattacharya and S. Fathpour, "High-speed 1.3 μm tunnel injection quantum-dot lasers", Applied Physics Letters, Volume: 86, Issue: 15, Article Number: 153109 (3 pages), (2005).

[7] M. Kuntz et al, "10 Gbit/s data modulation using 1.3μm InGaAs quantum dot lasers", Electronics Letters, Volume:41, Issue: 5, Pages: 244-245 (2005).

[8] D. OBrien et al., "Feedback sensitivity of 1.3μm InAs/GaAs quantum dot lasers", Electronics Letters, Volume: 39, Issue: 25, Pages: 1819-1820 (2003).

[9] J.R.O'Callaghan et al., "Focusing properties of high brightness gain tailored broad-area semiconductor lasers", IEEE Photonics Technology Letters, Volume: 14, Issue:1, Pages: 9-11, (2002).

[10] Todd D. Steiner, "Semiconductor Nanostructures for Optoelectronic Applications", Artech House, ISBN : 1580537510, 9781580537513, (2004).

[11] John H. Davies, "The physics of low-dimensional semiconductors: an introduction", Cambridge University Press, ISBN : 052148491X, 9780521484916, (1998).

[12] K. Petermann, "Laser Diode Modulation and Noise", Springer, ISBN : 079231204X, 9780792312048, (1991).

[13] C.H. Henry, "Theory of the linewidth of semiconductor lasers", IEEE Journal of Quantum Electronics, Volume: 18, Issue: 2, Pages: 259-264 (1982).

[14] T. C. Newell et al, "Gain and Linewidth Enhancement Factor in InAs Quantum-Dot Laser Diodes", IEEE PHOTONICS TECHNOLOGY LETTERS, Volume: 11, Issue: 12, Pages: 1527-1529, (1999).

[15] Sergey Melnik and Guillaume Huyet, "The linewidth enhancement factor α of quantum dot semiconductor lasers", Optical Society of America, Volume : 14, Issue: 7, Pages: 2950-2955, (2006).

[16] John houlihan and Carmel Kelleher, "Stability properties of current-profiled quantum dot lasers", Optics Communications, Volume: 281, Issue: 5, Pages: 1156-1161, (2008).

[17] Maria Teresa Todaro et al., "Simultaneous achievement of narrow pulse width and low pulse-to-pulse timing jitter in 1.3μm passively mode-locked quantum-dot lasers", OPTICS LETTERS, Volume: 31, Issue: 21, Pages: 3107-3109, (2006).

[18] P. M. Smowton et al, "Filamentation and linewidth enhancement factor in InGaAs quantum dot laser", Applied Physics Letters, Volume: 81, Issue: 17, Pages: 3251-3253, (2002).

[19] Ch. Ribbat et al, "Complete suppression of filamentation and superior beam quality in quantum-dot lasers", American Institute of Physics, Volume: 82, Issue: 6, Pages: 952-954, (2003).

[20] M. Kuntz et al, "Spectrotemporal response of 1.3μm quantum-dot lasers", American Institute of Physics, Volume: 81, Issue: 20, Pages: 3846-3848, (2002).

[21] F. T.Arecchi et al, "Pattern formation and competition in nonlinear optics", Elsevier Science, Volume: 318, Issues: 1-2, Pages: 1-83, (1999).

[22] S. P.Hegarty et al, "Pattern Formation in the Transverse Section of a Laser with a Large Fresnel Number", Physical Review Letters, Volume: 82, Issue: 7, Pages: 1434-1437, (1999).

[23] K. F. Huang et al, "Observation of the Wave Function of a Quantum Billiard from the Transverse Patterns of Vertical Cavity Surface Emitting Lasers", Physical Review Letters, Volume: 89, Issue: 22, Article Number: 224102 (4 pages), (2002).

[24] Y. F.Chen et al, "Observation of Vector Vortex Lattices in Polarization States of an Isotropic Microcavity Laser", Physical Review Letters, Volume: 90, Issue: 5, Article Number: 053904 (4 pages), (2003).

[25] O'Neill et al, "Dynamics of Traveling Waves in the Transverse Section of a Laser", Physical Review Letters, Volume: 94, Issue: 14, Article Number: 143901 (4 pages), (2005).

[26] Y.Tanguy et al, "Mode formation in broad area quantum dot lasers at 1060 nm", Elsevier Science, Volume: 235, Issues: 4-6, Pages: 387-393, (2005).

[27] C.Lindsey et al, "Tailored-gain broad-area semiconductor laser with single-lobed diffraction-limited far-field pattern", Electronics Letters, Volume: 21, Issue: 16, Pages: 671-673, (1985).

[28] V. Voignier et al, "Stabilization of self-focusing instability in wide-aperture semiconductor lasers", Phys. Rev. A, Volume: 65, Issue: 5, Article Number: 053807 (5 pages), (2002).

[29] K. Petermann, "Some relations for the far-field distribution of semiconductor lasers with gain-guiding", Optical and Quantum Electronicss, Volume: 13, Issue: 4, Pages: 323-333, (1981).

[30] A. Markus et al, "Simultaneous two-state lasing in quantum-dot lasers", Applied Physics Letters, Volume: 82, Issue: 12, Pages: 1818-1820, (2003).

[31] E. A. Viktorov et al, "Electron-hole asymmetry and two-state lasing in quantum dot lasers", Applied Physics Letters, Volume: 87, Issue: 5, Pages: 1818-1820, (2005).

[32] E. A. Viktorov et al, "Low-frequency fluctuations in two-state quantum dot lasers", OPTICS LETTERS, Volume: 31, Issue: 15, Pages: 2302-2304, (2006).

[33] E. O'Neill et al, "Coupling of large aperture semiconductor lasers by gain profiling", Optics Communications, Volume: 220, Issues: 4-6, Pages: 419-423, (2003).

[34] B. Dagens et al, "Giant linewidth enhancement factor and purely frequency modulated emission from quantum dot laser", ELECTRONICS LETTERS, Volume: 41, Issue: 6, Pages: 323-324, (2005).

[35] S. Fathpour et al, "Linewidth enhancement factor and near-field pattern in tunnel injection $In_{0.4}Ga_{0.6}As$ self-assembled quantum dot lasers", ELECTRONICS LETTERS, Volume: 39, Issue: 20, Pages: 1443-1445, (2003).

[36] T. C. Newell et al, "Gain and Linewidth Enhancement Factor in InAs Quantum-Dot Laser Diodes", IEEE, Volume: 11, Issue: 12, Pages: 1527-1529, (1999).

[37] D.G. Deppe et al, "Physics of Quantum Dot Lasers: Threshold Temperature Dependence, Internal Loss Effects, and Threshold Current Density", IEEE, Nano-Optoelectronics Workshop, Issue: 2-15, Pages: 64-65 (2008).

[38] D. OBrien et al, "Sensitivity of quantum-dot semiconductor lasers to optical feedback", Optics Letters, Volume: 29, Issue: 10, Pages: 1072-1074, (2004).

[39] J. K. Kim et al, "Design parameters for lateral carrier confinement in quantum-dot lasers", APPLIED PHYSICS LETTERS, Volume: 74, Issue: 19, Pages: 2752-2754, (1999).

[40] J.P. Reithmaier et al, "Next Generation High Power Quantum Dot Laser Materials", e-Newsletter n^o'2 from http://www.ist-brighter.eu, November, (2007).

[41] H. Benisty et al, "Intrinsic Mechanism for the poor Luminescence Properties of Quantum-Box System", Phys. Rev. B, Volume: 44, Issue: 19, Pages: 10945-10948, (1991).

[42] C.Z. Ning et al, "From Microscopic Physics to Advanced Semiconductor Laser Modeling and Simulation", http://www.nusod.org/nusod01/ning01nusod.pdf, Retrieved 2.01, August 28, (2009).

[43] A. V Uskov et al, "Carrier-induced refractive index in quantum dot structures due to transitions from discrete quantum dot levels to continuum states", Applied Physics Letters, Volume: 84, Issue: 2, Pages: 272-274, (2004).

[44] S.P. Hegarty et al, "Free-carrier effect on index change in 1.3 μm quantum dot laser", Electronics Letters, Volume: 41, Issue: 7, Pages: 416-418, (2005).

[45] O. Carroll et al, "Length dependence of feedback sensitivity of InAs/GaAs quantum dot lasers", Electronics Letters, Volume: 41, Issue: 16, Pages: 911-912, (2005).

[46] Wikipedia contributors, "Split-step method.", In Wikipedia, The Free Encyclopedia. from http://en.wikipedia.org/w/index.php?title=Split-step_method&oldid=296133562, Retrieved 12.09, August 21, (2009).

[47] Wikipedia contributors, "Laser Diode.", In Wikipedia, The Free Encyclopedia. from http://en.wikipedia.org/w/index.php?title=Split-step_method&oldid=296133562, Retrieved 1.09, August 21, (2009).

[48] Bright.EU contributors, http://www.bright-eu.org, Retrieved 11.29, August 24, (2009).

[49] A.D. Andreev and E.P. O'Reilly, "Optical matrix element in InAs/GaAs quantum dots: Dependence on quantum dot parameters", Applied Physics Letters, Volume: 87, Issue: 21, Article Number: 213106 (3 pages), (2005).

[50] E. Gehrig and O. Hess, "Spatiotemporal Dynamics and Quantum Fluctuations in Semiconductor Lasers", Springer Tracts in Modern Physics, Volume: 189 , ISBN: 978-3-540-00741-8, (2003).

[51] J. Muszalski, J. Houlihan, J. Huyet, B. Corbett, "Measurement of linewidth enhancement factor in self-assembled quantum dot semiconductor lasers emitting at 1310 nm", Electronics Letters, Volume: 40, Issue:7, Pages: 428-430, (2004).

[52] J. Houlihan, J. R. OCallaghan, V. Voignier, G. Huyet, J. G. McInerney, and B. Corbett, "Experimental observation of traveling waves in the transverse section of a laser", Optics Letters, Volume: 26, Issue: 20, Pages: 1556-1558, (2001).

[53] I. ODriscoll, T. Piwonski, J. Houlihan, G. Huyet, R. J. Manning, and B. Corbett, "Phase dynamics of InAs/GaAs quantum dot semiconductor optical amplifiers", Applied Physics Letters, Volume: 91, Issue: 26, Article Number: 263506 (3 pages), (2007).

[54] G. P. Agarwal, "Fast-Fourier-transform based beam-propagation model for stripe-geometry semiconductor lasers: Inclusion of axial effects", Journal of Applied Physics, Volume: 56, Issue: 11, Pages: 3100-3109 (1984).

[55] Takayoshi Mamine, Tatsuji Oda, and Osamu Yoneyama, "New class of gain guiding laser with a tapered-stripe structure", Journal of Applied Physics, Volume: 54, Issue: 8, Pages: 4302-4304, (1983).

[56] Fujitsu, "25Gbps Data Communication Using Quantum Dot Laser.", from http://www.fujitsu.com/global/news/pr/archives/month/2010/20100520-01.html, Retrieved 18.14, July 17, (2010).

[57] Marvin J. Weber, "Handbook of Lasers", CRC Press, ISBN : 9780849335099, (2001).

[58] Roland Diehl, "High-power diode lasers: fundamentals, technology, applications", Springer series: Topics in Applied Physics, Volume: 78, ISBN: 978-3-540-66693-6, (2000).

[59] E. Gehrig, O. Hess, C. Ribbat, R.L. Sellin, D Bimberg, "Dynamic filamentation and beam quality of quantum-dot lasers", Applied Physics Letters, Volume: 84, Issue: 10, Pages: 1650-1652, (2004).

[60] P. L. Knight, A. Miller, "Diode laser arrays", Cambridge University Press, ISBN: 0521419751, (1994).

[61] Robert K. Willardson, W. T. Tsang, Albert C. Beer, "Lightwave Communications Technology - Part B Semiconductor Injection Lasers, I", Academic press INC, ISBN: 9780127521510, Volume 22, Part 2, (1985).

[62] Eugene Hecht, "Optics", Addison-Wesley, ISBN: 0805385665, 9780805385663, (2002).

[63] Javier Alda, "Laser and Gaussian Beam Propagation and Transformation", Encyclopedia of Optical Engineering, ISBN: 978-0-8247-0940-2, (2003).

[64] Wikipedia contributors, "Gaussian beam", In Wikipedia, The Free Encyclopedia. from http://en.wikipedia.org/w/index.php?title=Gaussian_beam&oldid=374502768, Retrieved 14.53, July 20, (2010).

[65] Rudiger Paschotta, "Encyclopedia of Laser Physics and Technology", Wiley-VCH, ISBN-10: 978-3-527-40828-3, (2008).

[66] Y. Miyazaki et al, "Small-chirp 40-Gbps electroabsorption modulator with novel tensile-strained asymmetric quantum-well absorption layer", IEEE, Volume: 39, Issue: 6, Pages: 813-819, (2003).

[67] Fred M. Dickey, "Laser beam shaping applications", Taylor & Francis, ISBN: 0824759419, (2005).

[68] C. Roundy, "Propagation factor quantifies laser beam performance", Laser Focus World, December(1999)."

[69] A. E. Siegman, "How to (maybe) measure laser beam quality", Optical Society of America, Tutorial presented at annual meeting, TOPS Volume, (1998).

[70] Wikipedia contributors, "Beam diameter", In Wikipedia, The Free Encyclopedia. from http://en.wikipedia.org/w/index.php?title=Beam_diameter&oldid=357096599, Retrieved 17.53, 7 September (2010).

[71] D Sands, "Diode lasers (Series in Optics and Optoelectronics)", Taylor & Francis, ISBN-10: 0750307269, (2004).

[72] John Wilson, John Hawkes,"Optoelectronics: An Introduction", Prentice Hall, ISBN-10: 013103961X, (1998).

[73] Mool C. Gupta, "The handbook of photonics", Taylor & Francis, ISBN-10: 0-8493-3095-5, (2007).

[74] S S Jha,"Perspectives in optoelectronics", World Scientific publishing Co. Pte. Ltd, ISBN: 978-981-02-2022-8, (1995).

[75] Shun Lien Chuang, "Physics of photonic devices", John Wiley and Sons, ISBN: 978-0-470-29319-5, (2009).

[76] J. M. Liu, "Photonic Devices", Cambridge university press, ISBN: 9780521551953, (2005).

[77] M. Osinski, J Buus, "Linewidth broadening factor in semiconductor lasers–An overview", IEEE Journal of Quantum Electronics, Volume: 23, Issue:1, Pages: 9-29, (1987).

[78] Manijeh Razeghi, "Technology of Quantum Devices", Springer, ISBN 978-1-4419-1055-4, (2010).

[79] Benisty et al., "Intrinsic mechanism for the poor luminescence properties of quantum-box systems", Phys. Rev. B, Volume: 44, Issue: 19, Pages: 10945-10948, (1991).

[80] Prasad N.Prasad, "Nanophotonics", John Wiley and sons, ISBN: 978-0-471-64988-5, (2004).

[81] A.V. Uskov et al., "On ultrafast optical switching based on quantum-dot semiconductor optical amplifiers in nonlinear interferometers", IEEE Photonics Technology Letters, Volume: 16, Issue: 5, Pages: 1265-1267, (2004).

[82] M. Sugawara et al., "Effect of phonon bottleneck on quantum-dot laser performance", Applied Physics Letters, Volume: 71, Issue: 19, Pages: 2791-2793, (1997).

[83] Ralf Ostendorf, "High-Power High-Brightness Tapered Diode Lasers and Amplifiers", Brigther meeting presentation, Madrid 25^{th}, October (2007).

[84] Martin Maiwald et al., "600 mW optical output power at 488 nm by use of a high-power hybrid laser diode system and a periodically poled $MgO : LiNbO_3$ bulk crystal", Optics Letters, Volume: 31, Issue: 6, Pages: 802-804, (2006).

[85] Elias Towe, "Phase-locked semiconductor quantum well laser arrays", Technical Report No: 526, MIT Research Laboratory of Electronics, Cambridge, Massachusetts, (1987).

[86] Arecchi FT et al., "Deterministic chaos in laser with injected signal", Optics Communication, Volume: 51, Issue: 5, Pages: 308-314, (1984).

[87] Tredicce JR et al., "Instabilities in lasers with an injected signal", Journal of the Optical Society of America B, Volume: 2, Issue: 1, Pages: 173-183, (1985)

[88] Paul Mandel, "Theoretical problems in cavity nonlinear optics", Cambridge Studies in Modern Optics, ISBN: 9780521553858, (1997).

[89] Giuseppe Palumbo, "Lasers and current optical techniques in biology", The royal society of chemistry, ISBN: 978-0-85404-321-7, (2004).

[90] S. C. Gupta, "Textbook on optical fiber communication and its applications", Prentice-Hall of India, ISBN: 9788120324992, (2004).

[91] Z. Zhang et al., "High-power Tm-doped fiber distributed-feedback laser at 1943 nm", Optics Letters, Volume: 33, Issue: 18, Pages: 2059-2061, (2008).

[92] Robert G. Hunsperger, "Integrated Optics: Theory and Technology", Springer-Verlag, ISBN: 0387897747, (2009).

[93] D. Botez et al., "High-Power Diffraction-Limited-Beam Operation from Phase-Locked Diode-Laser Arrays of Closely Spaced 'Leaky' Waveguides (Antiguides)", Applied Physics Letters, Volume: 53, Issue: 6, Pages: 464-466, (1988).

[94] Thomas L. Koch , "Optical Fiber Telecommunications IIIA Volume 3A", Academic Press, ISBN-10: 0123951704, (1997).

[95] Mitsuo Fukuda , "Optical Semiconductor Devices", John Wiley and sons, ISBN: 978-0-471-14959-0, (1999).

[96] S. Biellak, G. Fanning, S.Wong, and A. Siegman, Reactive-ion-etched diffraction-limited unstable resonator semiconductor lasers, IEEE J. Quantum Electron, Volume: 33, Issue: 2, Pages: 219-230, (1997).

[97] J. Salzman et al., Unstable resonator semiconductor lasers. Part 2: Experiment, Optoelectronics, IEE Proceedings J, Volume: 134 Issue:1, pages: 76 - 86, (1987).

[98] Y. Tanguy et al., "'Focusing properties of semiconductor lasers with broad-area and shaped unstable resonator"', IEEE PHOTONICS TECHNOLOGY LETTERS, Volume: 15, Issue: 5, Pages: 637-639, (2003).

[99] E. A. Viktorov et al., "'Recovery time scales in a reversed-biased quantum dot absorber"', Applied Physics Letters, Volume: 94, Issue: 26, Article Number: 263502 (3 pages), (2009).